Thèse de Doctorat
de L'Ecole normale supérieure
Spécialité Physique
Laboratoire de Physique Statistique
présentée par
Claudio Falcon
pour obtenir le titre de
Docteur de l'Université Pierre et Marie Curie

Quelques effets des fluctuations sur les systèmes collectifs

Soutenu le 12 Décembre 2008
devant le jury composé de

M.	Yves Couder	(président)
M.	Phillipe Petitjeans	(rapporteur)
M.	Olivier Cadot	(rapporteur)
M.	Stéphan Fauve	(directeur de thèse)
M.	Eric Falcon	(invité)
M.	Angel Alastuey	(examinateur)
M.	Christophe Josserand	(examinateur)

Contents

Resumé de la thèse:

Dans cette thèse, nous présentons une étude théorique et expérimentale des fluctuations dans des systèmes dissipatifs forcés hors de léquilibre. Dans une première partie nous étudions les fluctuations de la puissance injectée nécessaire à maintenir le système dans un régime stationnaire, dans le cas d'un forçage aléatoire gaussien. Nous montrons que la fonction de distribution de probabilité (PDF) de la puissance injectée comporte des ailes exponentielles et une singularité en zéro. Ces propriétés sont décrites à laide dun calcul théorique simple. Nous montrons aussi que ce type de PDF peut être observée dans différents systèmes dissipatifs. Nous étudions également la relation entre les fluctuations de la puissance injectée moyennée sur un intervalle de temps et l'énergie interne (Théorème de Fluctuation). Dans une deuxième partie, nous présentons deux études expérimentales des fluctuations de l'amplitude locale des vagues à la surface d'un liquide. La première étude est consacrée aux fluctuations des ondes de surface résultant de lamplification paramétrique en présence d'un écoulement tourbillonnaire. Nous montrons que les fluctuations de l'amplitude et le seuil d'instabilité paramétrique augmentent avec l'intensité de l'écoulement tourbillonnaire. La deuxième étude est consacrée à la turbulence d'ondes capillaires à la surface d'un liquide en apesanteur ou à linterface entre deux liquides non miscibles de même densité. Nous montrons que la densité de puissance spectrale (PSD) de l'amplitude locale des vagues suit une loi de puissance en fonction de la fréquence et nous trouvons un bon accord entre l'exposant mesuré et sa prédiction théorique.

Mots clés: **GRANDEURS GLOBALES, FONCTION DE GRANDES DEVIATIONS, THEOREME DE FLUCTUATION, AMPLIFICATION PARAMETRIQUE, TURBULENCE DE DEFAUTS, TURBULENCE D'ONDES.**

Abstract:

In this thesis, we present a theoretical and experimental study of fluctuations in dissipative systems forced out of equilibrium. In the first part, we study the fluctuations of the injected power necessary to maintain a system in a stationary state in the case of a random gaussian forcing. We show that the probability distribution function (PDF) of the injected power presents exponential tails and a singularity at zero. These properties are described by means of a simple theorical calculation. We also show that this type of PDF can be observed in different dissipative systems. Then, we study the relation between the fluctuations of the injected power averaged over a given time lag and the internal energy of the system (Fluctuation Theorem). In the second part, we present two experimental studies of the local amplitude fluctuations of surface waves at a fluid-fluid interface. The first study is devoted to the fluctuations of parametrically amplified surface waves in the presence of a vortex flow. We show that the amplitude fluctuations and the parametric instability threshold increase with the vortex flow intensity. The second study is devoted to capillary wave turbulence developing in a microgravity environment or at the interface between two inmiscible fluids of equal densities. We show that the power spectral density (PSD) of the local wave amplitude follows a power-law as a function of frequency and we find good agreement between the measured exponent and its theoretical prediction.

Key words: **GLOBAL OBSERVABLES, LARGE DEVIATION FUNCTION, FLUCTUATION THEOREM, PARAMETRIC AMPLIFICATION, DEFECT-MEDIATED TURBULENCE, WAVE TURBULENCE.**

Thèse préparée au Laboratoire de Physique Statistique, UMR 8550 Département de Physique de l'Ecole Normale Supérieure de Paris, 24 rue Lhomond 75005, Paris, France.

Acknowledgements

During my period as a PhD student I had lots of help and encouragement, more than I thought I would get with the help of my run-of-the-mill french from more people that I thought I would meet. In these lines I'll try to acknowledge the aid of these people, which are all of great importance in the developement of this manuscript.

I have to start by thanking the former director of the Laboratoire de Physique Statistique de l'Ecole Normale Supérieure de Paris (LPS-ENS), Jacques Meunier, and the present director, Eric Perez, for receiving me and allowing me to take part in this active research enviroment.

I don't know if any of the former students under the direction of Stéphan Fauve can really determine how much they owe to him or how much they have learnt from his knwoledge, expertise and intuition in several domains of physics (I am tempted to say "in every domain", by most likely, he would crack a joke saying "you exagerate... again"). It is out of the question to say that this PhD work could not be done without his advice, not only from the experimental and theoretical point of view, but from the personal one also. I am much indebted to him for all his support, time and interest. Even from the beginning, when he had no time to spare (that is a new one...), he found a way to commence my PhD research subject when he introduced me to Eric Falcon (no accent on the "o"), who became the second advisor of this thesis. There is no doubt that his humor, professionalism and dedication have advanced this work and enriched it much farther and further than our initial expectations. I learnt a lot from him, and I hope to keep doing so.

I thank M. Phillipe Petitjeans and M. Olivier Cadot, who have kindly accepted to read, correct and report this manuscript, and M. Yves Couder, M. Angel Alastuey and M. Christophe Josserand, the members of the jury, for their interest in this PhD work.

I have great pleasure to acknowledge the constant support and humor of *la piéce D24* and all the people who came through those doors and that I had the chance to meet. I have to start by thanking the omnipresent Michaël Berhanu, from whom I've learnt quite a lot about magneto-hydrodynamics, electromagnetism and french cooking. He always had the time to spare and correct advise when I needed. I owe him also for his ever full cookie drawer, from which I inescrupulously took quite a few cookies, when my experiments run along the night. I sincerely hope we will meet again soon.

I am grateful for the constant interest and time that Francois Pétrelis gave to me, even when I tried, in my poor, almost laughable french, to explain a problem to him. He taugh me with the best of moods a lot of new tricks on how to device experimental set-ups, approach a new problem from a simple point of view (and how not to drink mojitos). Almost every single day, I could count on him to discuss physics or other non related subjects, making the labwork an enjoyable time.

Nicolas Mordant always had the time to show me some new stuff on physics. And did it with the best of the attitudes. Even when he could not afford the time. I am much grateful for that. I hope he continues to do so with Basile Gallet, who arrived last year, to whom I wish the best of lucks in his forthcomming PhD period.

I have to thank the help of Sébastien Aumaître, with whom I've discussed the subject of the fluctuations of injected power in out-of-equilibrium systems. I profited a lot from his knowledge on the subject and his simplicity to explain very complex phenomena.

I am much indebted to Jose da Silva Quintas, Claude Laroche and Artyom Petrosian for their technical support in devicing the experimental set-ups of this thesis. Without their help, it

could not be done. Nor it could be done without the help of Marie Gefflot, Annie Ribaudeau and Nora Sadaoui, the secretaries of the LPS-ENS, on the multiple administrative tasks.

Agradezco al contingente chileno que sigue en la larga y angosta franja de tierra y que ha seguido desde lejos los avances de este trabajo por su interés y buenos consejos: Marcel Clerc, Enrique Tirapegui, Nicolás Mujica, Rodrigo Soto.

Ahora, tengo el placer de agradecer al contigente chileno que sigue en la Francia, por el buen humor, amistad y alegría que me regalaron durante mi periplo europeo, y que en verdad, no pensé encontrar. Muchas gracias, a Giorgio y Miguel, los primeros *colocs* en la llegada a Paris (y que tuvieron que soportarme por largos dos años), a Gustavo "la Máquina" Düring, el presidente emérito de la Asefe, a los Tamarillos, a los BravOviedo, a Dani y Gaby, a Francisca, a Sergio Rica incluso, a Luchito, a Cristobal (Ratita) y MariLu, en fin, a la comunidad chilena que me alegro los días tristes.

Al final, tengo que darle las gracias a mi familia, que me aguanta y me sostiene, y que sin ellos esto en verdad sería un trabajo sin gracia. Todas las gracias de mundo a mis hermanos Cristián y Felipe, y a mis papás Moisés y Gladys por mantenerme tranquilo. Y a Marcela, mi negra, por lograr mantenerme contento.

A mis papás, Moisés y Gladys
los dos motores de este trabajo.

Part I

Introduction

Introduction

The theoretical and experimental studies developed in this thesis are focused on the statistical properties of observables and their fluctuations in dissipative systems when they are forced into a statistically stationary state far from equilibrium. In order to say that a system is "out-of-equilibrium" we need to define first what "equilibrium" means. A system with a large number of degrees of freedom is said to be in equilibrium (also called *thermodynamic equilibrium*) when is either isolated and does not interact with its surroundings or its temperature T is fixed externally by a thermal bath, also called a thermostat. In the case where the system has its temperature fixed externally, its energy E fluctuates and the probability of finding the system in a macroscopic state of energy E is proportional to $\exp[-E/k_BT]$, where k_B is the Boltzmann constant. In this "equilibrium" state, equipartition of energy occurs in the classical limit and each one of the internal degrees of freedom has a mean energy $e = \frac{k_BT}{2}$. For any observable O of the system, its higher order moments can be computed using the weight of the macroscopic state with energy E. Even more, when a small external forcing is applied to the system, such as a small electric field on a conducting liquid[1], or a small pressure gradient on a coloidal suspension[2], the response of the internal degrees of freedom to the perturbation can be estimated accurately by just assuming that the internal fluctuations of the system created spontaneously the small perturbation. This is the so called Fluctuation-Dissipation theorem. In that sense, just knowing the distribution function of a macroscopic state, we can estimate its response to small perturbations of its equilibrium.

This workframe breaks down when dissipation is included into the system. When this happens, no microscopic assumptions on the dynamical evolution of the internal degrees of freedom can be made. The system loses energy in time through certain processes and an external operator must be injecting it continously. In this configuration, fluctuations still occur, that are driven by the balance between injected and dissipated power. Therefore, the energy fluctuations of the system are not externally controlled and a description that can use the Boltzmann weights as a distribution function of the energy of the system is not possible. The observables, either global or local, present fluctuations that cannot be described by simply knowing the energy of the macroscopic state, because large energy fluctuations can be present and become quite common as the systems is continually maintained far from its equilibrium.

In this regime, there are no general distribution functions that can describe in different classes of systems, the fluctuations of the observables of interest. In any case, we will not try to develop a study for any type of "out-of-equilibrium" system. We shall focus on the particular case of statistically stationary states, where temporal averages are well defined. We will use the temporal average $\langle\rangle$ and assume that the system under study presents a stationary out-of-equilibrium state, in some sense, ergodic[3]. In that way, the spatial average over the system volume V of the temporally averaged

[1] As first studied by Smoluchowski (M. von Smoluchowski, Bull. Int. Acad. Sci. Cracovie, **184** (1903)).

[2] An approach to this problem was first given by Einstein (A. Einstein, Annalen der Physik **17**, 549-560 (1905)).

[3] For ergodicity in statistical mechanincs, see, for instance the book by Richard C. Tolman, *The Principles of Statistical Mechanics*, (New York, Dover, 2nd Edition, 1979)

observable $\langle O(t) \rangle$,

$$\frac{1}{V} \int_V \langle O(t) \rangle dV,$$

is the same as the ensemble average of the observable $O(\Gamma)$,

$$\int_\Sigma \Phi(\Gamma) O(\Gamma) d\Gamma,$$

where Γ is the phase space of the system, Σ is the volume of the phase space and $\Phi(\Gamma)$ is the ergodic invariant measure of the system, which depends solely on the available phase space volume and we assume it is known and can be calculated.

This fact allows us to relate ensemble averages, which are taken by averaging over the available phase space of the dissipative system using a suitable distribution function and temporal averages.

Global observables are quantities, such as the energy of the system or its entropy creation, that are averaged over the entire volume of the system. Even after being averaged on a large number of effective degrees of freedom, they can present large fluctuations with respect to their averaged values. These fluctuations can be asymmetric in their distribution functions, a fact related to the lack of microscopic reversibility (due to dissipation) and external control of the internal energy fluctuations. It is in this context that we present the first part of our study.

On the other hand, local fluctuations in systems forced far from equilibrium, such as the local velocity fluctuations in turbulent flows or the local concentration of chemicals in a chaotic chemical reaction, are known to display large fluctuations, bursts and even intermittency. The distribution functions and statistical properties of local fluctuations have been studied in depth in hydrodynamic turbulence[4] and turbulent-like regimes in out-of-equilibrium systems. A great deal of attention has been placed on the study of these types of chaotic or stochastic regimes in systems that can sustain waves, such as bending waves of elastic sheets, Rayleigh waves on the surfaces of elastic solids, electromagnetic waves in vacuum or in a nonlinear medium, shock waves in gases, Langmuir waves in plasmas, and so forth[5]. In hydrodynamics, for instance, a fluid can sustain surface waves or internal waves, such as sound waves or inertial waves, which propagate in the bulk of the fluid. These waves will have different properties mainly described by their dispersion relation which depends on the type of restitution force that sustains them. When they are strongly excited or amplified, nonlinearities become important in their dynamical evolution.

These nonlinear interactions change the wave properties such as their energy transfer mechanism or their dissipation scale. They can also produce fluctuations in the amplitude or the phase of the waves that can modify the spatio-temporal evolution of the wave system. This type of fluctuations will be the main interest of the second part of our study.

The manuscript is divided into two different parts. The **First Part** is devoted to the *global* fluctuations of observables in out-of-equilibrium systems. We present the energy balance equation that relates injected and dissipated power and we use it to study simple systems where we can modelise these two observables (see Chapter 1). We extract relations between the statistical properties of these observables (such as their correlation time scales and standard deviations) when the system is set in a stationary out-of-equilibrium state. In Chapter 2, we study the injected power fluctuations I in dissipative systems where the dissipated power is proportional to the internal energy E of the system and the forcing driving the system is a random gaussian noise. The injected power distribution

[4]See for instance the work of A. S. Monin and A. M. Yaglom, *Statistical Fluid Mechanics: Mechanics of Turbulence* (Dover Publications, 2nd Edition, 2007).

[5]A long review on waves can be found in Whitham (G. B. Whitham, *Linear and Nonlinear Waves* (Wiley-Interscience, New York, 2nd Edition, 1999)

function displays several robust features, such as the appearance of exponential tails and a singular cusp close to $I \simeq 0$. Then, we discuss several systems where the injected power fluctuations display this type of probability distribution function. In Chapter 3, we probe the validity of the Fluctuation Theorem in such dissipative out-of-equilibrium systems.

The **Second Part** is devoted to the local fluctuations of waves in out-of-equilibrium systems. In Chapter 4 we present the general framework of wave fluctuations and discuss some specific systems where turbulent-like states develope. In Chapter 5 we present an experimental study on the fluctuations of parametrically excited surface waves. In two separate studies, statistical properties of the standing waves are studied when the wave pattern displays fluctuations. Finally, Chapter 6 is devoted to the experimental investigation of capillary wave turbulence. We present two separate studies where the statistical properties of pure capillary dispersive waves are studied.

Conclusions and Perspectives are presented in the last part in which we underline the main results of our work and propose further developements related to this study.

Part II

Fluctuations of global quantities in out-of-equilibrium systems

Chapter 1

Energy balance in out-of-equilbrium systems

We recall in this Chapter, through a simple but general balance equation, several results on the properties of the energy fluctuations in ou-of-equilibrium dissipative systems in steady states. Some interesting relationships between injection and dissipation of energy in these systems are also presented in Section 1.1. Then, we study the case of constant dissipation as the simplest type of dissipation in Section 1.2. As an approach to other complex systems, we then study the case of linear damping in Section 1.3.

1.1 Description of the problem

1.1.1 Balance Equation

The main equation that concerns the energy flux to drive a system into an out-equilibrium state is the following

$$\frac{dE(t)}{dt} = P_{inj}(t) - P_{diss}(t). \tag{1.1}$$

Here $P_{inj}(t)$ stands for the injected power to drive the system out-of-equilibrium, $P_{diss}(t)$ stands for the dissipated power and $E(t)$ is the energy of the system. The three observables are global quantities, spatially averaged over the whole system. We will call $R(t) = P_{inj}(t) - P_{diss}(t)$, the forcing term of the system. Eq. (1.1) describes the evolution of the rate of change of the internal energy as these two operators balance their effects.

For several out-of-equilibirum systems, the energy flux evolution can be written in the form of Eq.(1.1), for example:

- Incompresible hydrodynamic turbulence [1]. In hydrodynamics, as the mean flow of a fluid is increased, turbulence develops. A statistical approach to the study of the flow properties (such as the energy fluctuations or transport coefficients) is often used. The transition from a laminar or smooth situation to a fluctuating or turbulent one is controlled by the Reynolds number $Re = VL/\nu$, where V and L are the typical velocity and length scales of the flow, and ν is the kinematic viscosity of the fluid. For $Re \gg 1$, large fluctuations in the velocity field occur and turbulence is said to be developed. In this regime the energy balance equation of Eq.(1.1) has been studied [2]. Taking the NAVIER-STOKES equation

$$\rho\left[\frac{\partial \mathbf{v}}{\partial t} + \mathbf{v}\cdot\nabla\mathbf{v}\right] = -\nabla p + \rho\nu\nabla^2\mathbf{v} + \mathbf{f},$$

where ρ is the density of the fluid, ∇p its local pressure gradient and $\mathbf{f}(\mathbf{r},t)$ is the external forcing per unit of volume. Multiplying the above equation by the velocity field $\mathbf{v}(\mathbf{r},t)$ and integrating over the volume of the system V, the energy balance equation (Eq. (1.1)) is statisfied with

$$E = \rho \int_V \frac{v^2}{2} d\mathbf{r}, \quad P_{inj} = \int_V \mathbf{f}\cdot\mathbf{v} d\mathbf{r}, \quad P_{diss} = \rho\nu \int_V \omega^2 d\mathbf{r},$$

where $\omega \equiv \nabla \times \mathbf{v}$ is the local vorticity field. The velocity field $\mathbf{v}(\mathbf{r},t)$ is zero at the boundaries but its vorticity is not. Here, P_{diss} is always positive and P_{inj} can change sign depending on the sign of the integrated local injected power $\mathbf{f}\cdot\mathbf{v}$. To eliminate the boundary terms related to the velocity, we have used the incompressibility condition $\nabla\cdot\mathbf{v} = 0$ and to eliminate the boundary term related to the pressure we have assume that the boundaries do not move. In the case where the forcing is made by means of a moving boundary $\partial\mathcal{V}$ (such as impellers [2] or wavemakers[3]), the injection term will read in that case

$$P_{inj} = \int_{\partial\mathcal{V}} (p + \frac{\rho v^2}{2})\mathbf{v}\cdot\mathbf{n} dS + \int_{\partial\mathcal{V}} \rho\nu(\mathbf{v}\times\omega)\cdot\mathbf{n} dS.$$

The first term will be nonzero when the velocity $\mathbf{v}$ is not ortogonal to the unitary vector $\mathbf{n}$, normal to the moving boundary of the impellers, as it is shown in Fig.(1.1) for instance, that set the fluid in motion. The second one, related to the viscous stresses will be zero when no shear is applied on the fluid by the moving boundary.

- Granular gases [4]. An ensemble of N inelastic particles confined in a volume V can be regarded as a granular gas when the particle density $n = N/V$ is sufficiently low. In this low-density limit, events where 3 or more particles collide simultaneously are very unlikely and binary collisions dominate the momentum transfer between particles. The collision rule for the velocities of a pair of inelastic particles after they interact $\mathbf{v_1}^*$ and $\mathbf{v_2}^*$ (their initial velocities being $\mathbf{v_1}$ and $\mathbf{v_2}$) is

$$\mathbf{v_1}^* = \mathbf{v_1} - \frac{(1+r)}{2}\mathbf{n}(\mathbf{v_1}-\mathbf{v_2})\cdot\mathbf{n}, \quad \mathbf{v_2}^* = \mathbf{v_2} + \frac{(1+r)}{2}\mathbf{n}(\mathbf{v_1}-\mathbf{v_2})\cdot\mathbf{n},$$

where $\mathbf{n}$ is the vector joining the center of both particles. We suposse here that they interact as hard inelastic spheres [5], as shown in Fig. (1.2). The restitution coefficient $0 < r < 1$ relates the efficency of the momentum transfer before and after the colision. Note that in the elastic case $r = 1$, we can change $\mathbf{v_1}$ and $\mathbf{v_2}$ by $\mathbf{v_1}^*$ and $\mathbf{v_2}^*$ making the system reversible in time. In this case no dissipation takes place and as the system is continually forced the energy of the system grows. The conservative limit can be shown to be a singular one, and precautions must be taken into account when taking the thermodynamic limit (in this case $r \to 1$) [6].

  The energy loss is proportional to the combined momenta of the particles that interact. The coefficient of proportionality is given by $(1-r^2)/4$ and the injection of energy is usually made by the colision of the particles with a moving boundary that "heats" the granular gas [4], as shown in Fig. (1.2). Eq.(1.1) is then satisfied with

$$E = \frac{1}{2}\sum_{i=1}^{N} m v_i^2 \quad P_{inj} = 2\nu_p \sum_{i=1}^{N} m\mathbf{V_p}\cdot(\mathbf{V_p}-\mathbf{v_i}), \quad P_{diss} = \frac{(1-r^2)}{4}\nu_c \sum_{i\neq j}^{N} m\mathbf{v_i}\cdot\mathbf{v_j},$$

where ν_p and ν_c are the mean collision frequency of a particle with the boundary and with another particle respectively, and $\mathbf{V_p}$ the velocity of the moving boundary.

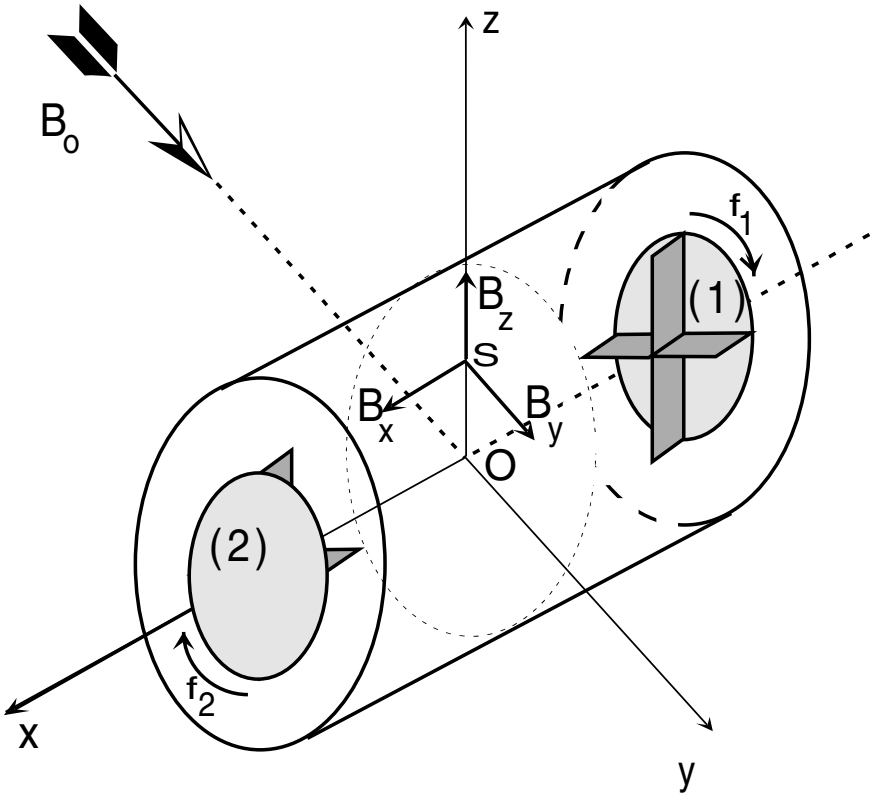

Figure 1.1: Experimental set-up of the VKS experiment, where a large volume of liquid Na is set into turbulent motion by means of rotating impellers at frequencies f_1 and f_2 to study the effect of turbulent fluctuations on the dynamo action (Figure taken from [2]).

- Turbulent thermal convection [7]. Let us consider a fluid confined between two infinite horizontal plates separated by a distance h. The temperature of the lower and upper plates are fixed at T_d and T_u respectively, with the temperature difference $(T_d - T_u) > 0$. When the temperature gradient $(T_d - T_u)/h$ is strong enough to overcome the dissipative losses due to viscous friction, the fluid stratification is unstable to small velocity perturbation and it starts to moves. In the BOUSSINESQ aproximation the motion of an incompresible fluid obeys

$$\rho \left[\frac{\partial \mathbf{v}}{\partial t} + \mathbf{v} \cdot \nabla \mathbf{v} \right] = -\nabla p + \rho \nu \nabla^2 \mathbf{v} + \rho g \alpha \delta T \mathbf{e_z},$$

and the local temperature $\delta T(\mathbf{r}, t)$ follows the advection-diffusion equation

$$\rho C_p \left[\frac{\partial \delta T}{\partial t} + \mathbf{v} \cdot \nabla \delta T \right] = \lambda \nabla^2 \delta T,$$

where ρ, α, ν, C_p and λ are the fluid density, thermal expansion coefficient, kinematic viscosity, heat capacity and thermal conductivity respectively, and g is the acceleration of gravity. Each coefficient, in this approximation is independent of the local temperature. The buoyancy force is modelized $\mathbf{f}(\mathbf{r}, t) = \rho g \alpha \delta T(\mathbf{r}, t) \mathbf{e_z}$, where $\mathbf{e_z}$ is a unit vector along the vertical (generally z) axis. Multiplying the equation of conservation of momentum by $\mathbf{v}(\mathbf{r}, t)$ and integrating over

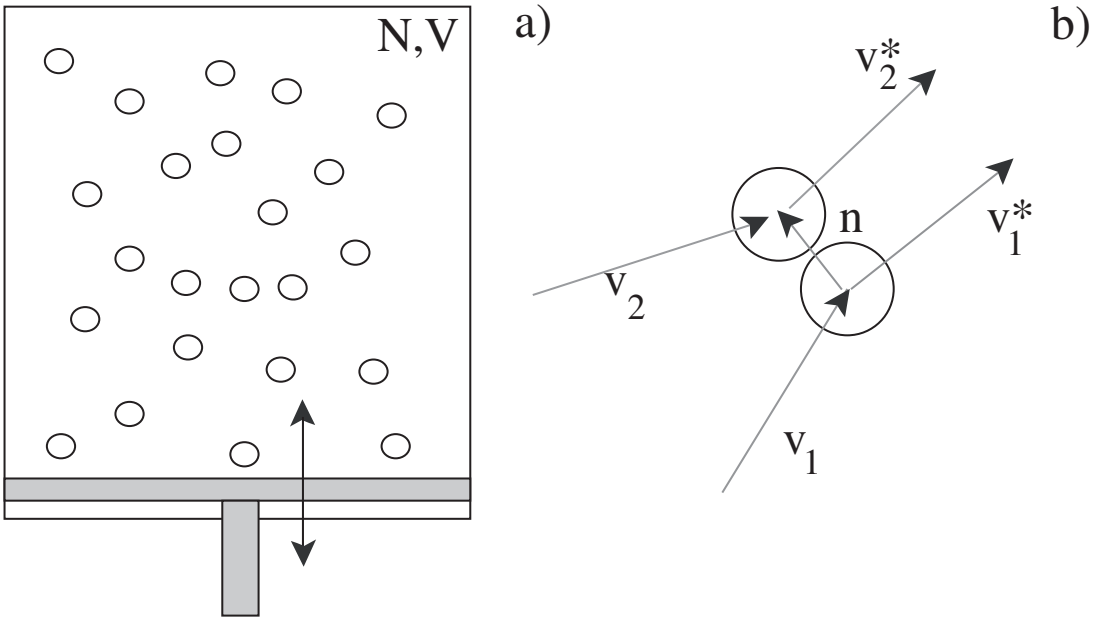

Figure 1.2: a) Granular gas with N inelastic particles confined in a volume V. The moving boundary injects energy constantly to the system by collisions. b) Collision rule for two inelastic particles interacting as hard spheres.

the volume, Eq.(1.1) is satisfied with

$$E = \rho \int_{\mathcal{V}} \frac{v^2}{2} d\mathbf{r}, \quad P_{inj} = \rho\alpha g \int_{\mathcal{V}} \delta T v_z d\mathbf{r}, \quad P_{diss} = \rho\nu \int_{\mathcal{V}} \omega^2 d\mathbf{r}.$$

When the buoyancy force is much larger than viscous friction, convection develops in the system in a random and fluctuating way. This regime is called turbulent convection and develops when the Rayleigh number $Ra = \rho C_p g \alpha h^3 (T_d - T_u)/(\nu\lambda) \gg 1$. In this regime, large fluctuations of velocity and temperature are observed, as it is shown in Fig.(1.3).

- Electronic systems [9]. In a simple electronic dipole composed of a resistance R and a capacitance C, an electromotive force $\varepsilon(t)$ must be applied to generate the mean motion of the electrons of the conductor, creating a current i which flows through the resistance, as shown in Fig.(1.4). Macroscopically, the continuity equation for the measured tension $U(t)$ over a closed circuit, reads

$$\varepsilon(t) = U(t) + Ri(t),$$

where the rate of change of the charge $Q(t)$ of the capacitance is given by

$$\frac{dQ(t)}{dt} = C\frac{dU(t)}{dt} \equiv i(t).$$

Multiplying the continuity equation by U, we can rewrite the expression as Eq. (1.1), with

$$E = \frac{1}{2}U^2, \quad P_{inj} = \gamma\varepsilon U, \quad P_{diss} = \gamma U^2,$$

where $\gamma = 1/RC$ is the inverse of the charging time of the RC dipole. We will take this simple system as a canonical example of a dissipative system and explore further the statistical properties of the fluctuations of these global quantities in later chapters.

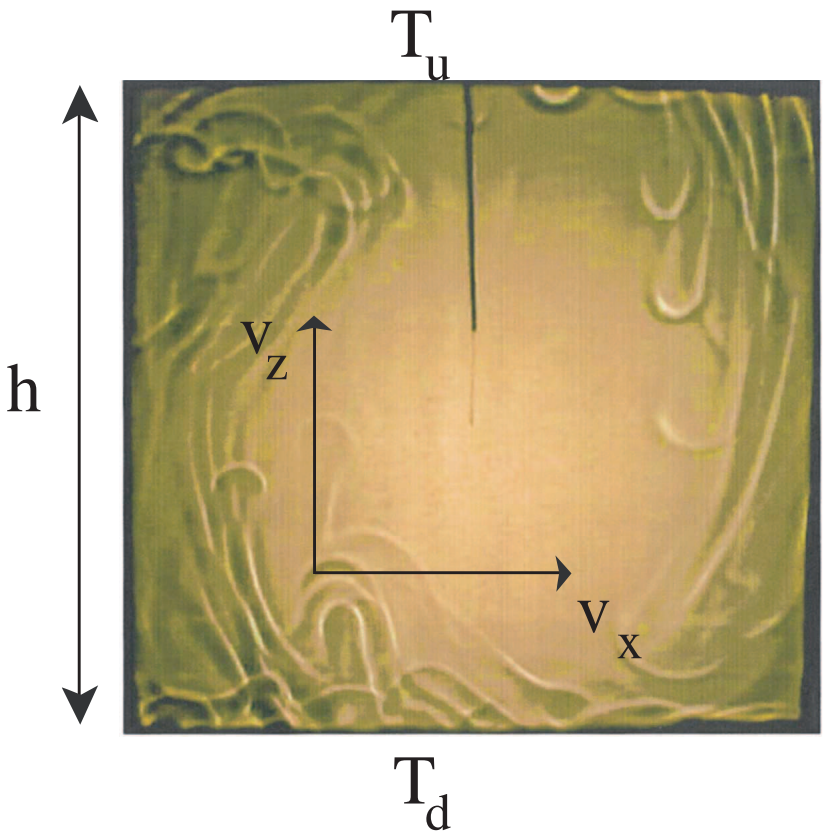

Figure 1.3: A shadowgraph showing the spatial distribution of thermal plumes in 3-D turbulent convection (Figure taken from [8])

As shown above, we can often discriminate injection and dissipation of energy per unit of time. However, it is important to notice that the choice of what is defined as the injected power and dissipated power is arbitrary. In each system under study we will be very clear on the choice of these operators.

It is straightforward to show that, in order to maintain a dissipative system whose energy evolution is described by Eq. (1.1) in a stationary state, a certain amount of power P_{inj} has to be injected into it. Power is generally transfered from the forcing device (for instance, rotating discs in turbulent swirling flows [2], a vibrating plate in a granular gas [6], a heating plate in turbulent convection [10], a moving wavemaker in wave turbulence [3]) into the system that will make use of the accessible injected power to excite its internal degrees of freedom and later dissipate it, if it can. Dissipation usually takes place at scales much smaller than the injection scale [1] and time-scales much shorter than the correlation time of the injected power.

The statistics of P_{inj} and P_{diss} can display remarkable differences. This is mainly due to the fact that dissipation is always defined positive $P_{diss} \geq 0$, while the injected power can display negative and positive events, depending on the type of driving force acting on the system.

1.1.2 Stationary States

In a stationary non-equilibrium state, global quantities, such as the energy of a system E, flucutate. We suppose, from now on, that these observables have statistically well-defined averages. This means

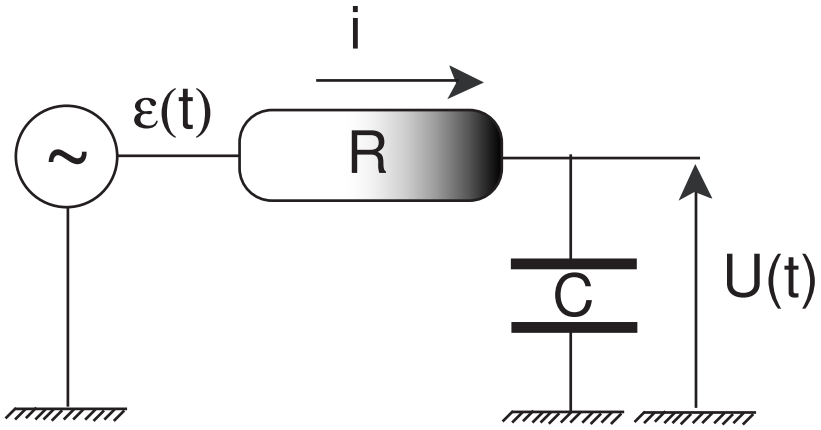

Figure 1.4: Electronic RC dipole submitted to an electromotive force $\varepsilon(t)$.

that for a time T larger than the internal correlation time τ_c of its fluctuations, the temporal average

$$\langle E \rangle_T (t) = \frac{1}{T} \int_t^{t+T} E(t')dt',$$

does not change with respect to T in the limit $T \to \infty$. In this limit, we will discard the index T in the time-averages and we will simply write $\langle E \rangle$, independent of time.

Following the reasoning in Section 1.1, a balance between the injected and dissipated power must be achieved in order to neglect the mean rate of change of E. Hence, several constrains and relationships between P_{inj} and P_{diss} have to be satisfied for a dissipative system to sustain a steady out-of-equilibrium state. These constraints are related to the statistical properties of these quantities, such as their averages $\langle P_{diss} \rangle$,$\langle P_{inj} \rangle$ or *rms* fluctuations $\sigma_{P_{inj}}$, $\sigma_{P_{diss}}$, where $\sigma_X = \sqrt{\langle X^2 \rangle - \langle X \rangle^2}$ for a given variable X.

In certain cases their fluctuations display values that are several times larger than their average values. Their statistics also present large deviations, even when they are averaged over the entire volume of the system or its boundaries [2]. Therefore, in this type of systems, the usual tools of equilibrium statistical mechanics do not apply, or can only be applied when the injection of energy into the system can be regarded through the scope of the Fluctuation-Dissipation theorem [11].

Averaging over time Eq. (1.1) leads to $\langle \dot{E} \rangle = \langle P_{inj} - P_{diss} \rangle = 0$ .We can see that, in order to maintain the system in a statistically stationary regime,

$$\langle P_{inj} \rangle = \langle P_{diss} \rangle ,$$

where the brackets $\langle \rangle$ stand for time average and we suppose that the system is, in a statistical sense, ergodic. From the definition above, $\langle R \rangle = 0$, which means that all the injected power is somehow dissipated by the system. This point is crucial: physically, the system itself chooses the way to dissipate its excess energy input. Even more, it chooses the way to relate the *rms* fluctuations of P_{inj} and P_{diss}, and by doing so, it fixes the *rms* fluctuations of the energy E, as we will show in the following parragraph.

1.1.3 Statistical properties of the energy flux in frequency domain

As shown above, the mean values of both injected and dissipated power have to be balanced in order to maintain the system in a stationary out-of-equilibirum state. But what about the fluctuations of

such quantities? What relationships can be extracted for their fluctuations? How do these relations control the energy fluctuations? These questions can be partially answered by looking carefully into the spectral properties of P_{inj} and P_{diss}. For that matter we define the Fourier transform of the fluctuating variable $X(t)$ as

$$\widehat{X}(\omega) = \frac{1}{2\pi}\int_{-\infty}^{\infty} X(t)e^{-i\omega t}dt,$$

and $\widehat{X}(\omega)^* = \widehat{X}(-\omega)$, where $\widehat{X}(\omega)^*$ stands for the complex conjugate of $\widehat{X}(\omega)$. When taking the Fourier transform of both injected and dissipated powers, we have eliminated their mean values using that their averages cancel each other in the steady state.

This procedure enables us to relate the statistical properties in frequency domain to the ones in time. For that matter we define the cross-correlation function of the statistically stationary fluctuating variables $X(t)$ and $Y(t)$ by

$$C_{XY}(t,t') \equiv \langle X(t)Y(t')\rangle - \langle X\rangle \langle Y\rangle .$$

It follows that in a statistically stationary state

- $C_{XY}(t,0) = C_{YX}(0,-t)$ (time translation)
- $C_{XY}(t,t') = C_{XY}(|t-t'|,0) \equiv C_{XY}(|t-t'|)$ (stationarity)
- $|C_{XX}(0)| \geq |C_{XX}(t)|$ (maximum correlation at the initial time)
- $\lim_{t\to\infty} C_{XY}(t) \to 0$ (events with large time lag are statistically independent)

This function indicates the degree of statistical dependence of a variable (or variables) at different periods of time. It can be related directly to the the spectral properties of their Fourier transforms by means of the Wiener-Khinchin theorem [11] which states

$$S_X(\omega) = \lim_{T\to\infty}\frac{1}{2}\int_{-T}^{T} C_{XX}(t)e^{-i\omega t}dt. \tag{1.2}$$

which simply means that the power spectral density $S_X(\omega)$ of the variable $X(t)$ defined by

$$\langle \widehat{X}(\omega)\widehat{X}(\omega')^*\rangle = S_X(\omega)\delta(\omega-\omega'),$$

is the Fourier transform of its autocorrelation function $C_{XX}(t)$.

In different dissipative systems, it is possible to estimate the *rms* fluctuations and typical time scales of the large scale (low-frequency) forcing of the system, related directly to the energy injection mechanism, but no direct information can be given on the dissipation mechanism and its intrinsic dynamics. Furthermore, cross-correlation functions of both global quantities cannot be deduced from first principles. This means that global relationships between P_{inj} and P_{diss} are of paramount importance to probe the internal energy transfer mechanisms and intermediate dynamics between injection and dissipation.

We apply the former definition of power spectral density and correlation functions to the energy balance equation. Taking the Fourier transforms of Eq. (1.1), the energy balance in frequency domain reads

$$-i\omega\widehat{E}(\omega) = \widehat{P}_{inj}(\omega) - \widehat{P}_{diss}(\omega). \tag{1.3}$$

We can deduce from Eq.(1.3) an interesting relationship between the typical time scales of injection and dissipation and their *rms* values. Multiplying Eq.(1.3) by $\widehat{P}_{inj}(\omega)^* + \widehat{P}_{diss}(\omega)^*$, the equation reads

$$-i\omega\widehat{E}(\omega)(\widehat{P}_{inj}(\omega)^* + \widehat{P}_{diss}(\omega)^*) = |\widehat{P}_{inj}(\omega)|^2 - |\widehat{P}_{diss}(\omega)|^2 + \widehat{P}_{inj}(\omega)^*\widehat{P}_{diss}(\omega) - \widehat{P}_{inj}(\omega)\widehat{P}_{diss}(\omega)^*. \quad (1.4)$$

This lengthy expression can be simplified by taking $\omega = 0$. Due to the fact that both variables are real, we have $\widehat{P}_{inj}(0) = \widehat{P}_{inj}(0)^*$ and $\widehat{P}_{diss}(0) = \widehat{P}_{diss}(0)^*$, which eliminate the crossed products. This leads to the zero-frequency equality of the power spectral densities of both variables $|\widehat{P}_{inj}(0)|^2 = |\widehat{P}_{diss}(0)|^2$, or, written in time-domain using the Wiener-Khinchin theorem,

$$\int_0^\infty (\langle P_{inj}(t)P_{inj}(0)\rangle - \langle P_{inj}\rangle^2)dt = \int_0^\infty (\langle P_{diss}(t)P_{diss}(0)\rangle - \langle P_{diss}\rangle^2)dt. \quad (1.5)$$

In order to extract direct information on the *rms* fluctuations, we can assume that the autocorrelation functions of the injected and dissipated power have exponentially decreasing behavior as $C_{P_{ing}P_{inj}}(t) \sim \sigma^2_{P_{inj}} e^{-|t|/\tau_{inj}}$ and $C_{P_{diss}P_{diss}}(t) \sim \sigma^2_{P_{diss}} e^{-|t|/\tau_{diss}}$, by doing so, we obtain the relationship

$$\sigma^2_{P_{inj}}\tau_{P_{inj}} = \sigma^2_{P_{diss}}\tau_{P_{diss}}, \quad (1.6)$$

where σ_X and τ_X are the *rms* and correlation time of the variable X. This relates both correlation times to the standard deviations of the injection and dissipation. In that sense, their *rms* values are fixed by the constrain of Eq.(1.6).

All the above relationships can be derived by integrating directly Eq. (1.1) in the long time limit. It is instructive to deduce the later relation between the zero-frequency spectrum of P_{inj} and P_{diss} in the stationary regime as follows [12]

$$\begin{aligned}
\sigma^2_{P_{inj}}\tau_{inj} &= \int_0^\infty \left[\langle P_{inj}(t)P_{inj}(0)\rangle - \langle P_{diss}\rangle^2\right] dt \\
&= \int_0^\infty \left[\left\langle (\dot{E}(t) + P_{diss}(t))(\dot{E}(0) + P_{diss}(0))\right\rangle - \langle P_{diss}\rangle^2\right] dt \\
&= \left\langle (E(\infty) - E(0))(\dot{E}(0) + P_{diss}(0))\right\rangle + \int_0^\infty \left[\left\langle P_{diss}(t)(\dot{E}(0) + P_{diss}(0)\right\rangle - \langle P_{diss}\rangle^2\right] dt \\
&= \langle E\rangle \langle P_{diss}\rangle - \langle E(0)P_{diss}(0)\rangle + \int_0^\infty \left[\left\langle P_{diss}(0)(\dot{E}(-t) + P_{diss}(t)\right\rangle - \langle P_{diss}\rangle^2\right] dt \\
&= \int_0^\infty \left[\langle P_{diss}(t)P_{diss}(0)\rangle - \langle P_{diss}\rangle^2\right] dt \\
&= \sigma^2_{P_{diss}}\tau_{diss} \quad (1.7)
\end{aligned}$$

where we have only used the stationarity of the system.

We have shown that the two quantities, P_{inj} and P_{diss}, and their fluctuations drive the dynamics and control the statistical properties of the internal energy E of an out-of-equilibrium system in a steady state ($\langle \dot{E}\rangle = 0$). In a statistically steady state, they are related by equations such as (1.6). Although experimentally, we cannot impose the form of dissipation the system will use to eliminate the excess of energy given by the injected power, it is an interesting task to modelised P_{diss} in simple systems, satisfying the previous results.

1.2 Constant Dissipation

The simplest choice of dissipation in an out-of-equilibrium system is the case where the dissipated power P_{diss} is constant and no dynamical considerations are taken into account for its fluctuations. This functional form is not completly unphysical: in granular gases it has been shown that in the elastic limit, the dissipated power can be taken as a constant [6]. Naturally, for a given type of injection operator P_{inj} (which we will call I from now on), the dissipated power P_{diss} cannot remain constant for an infinite ammount of time and it must eventually develop dynamical fluctuations in order to satisfy Eqs.(1.1) and (1.6). Anyway it is an interesting question to study this type of dissipation form.

For the case of constant dissipation, the energy balance reads

$$\frac{dE}{dt} = I(t) - \langle I \rangle \equiv \delta I(t),$$

where the energy fluctuations are related only to the autocorrelation function of the injection operator, beacuse $R(t) = \delta I(t)$. Although it is the simplest differential equation, in terms of stochastic processes, it has several aplications describing different physical processes such as brownian motion [13] proposed by Langevin or effective diffusion in hydrodynamic turbulence [14] proposed by Taylor. Eq. (1.1) can be formally integrated, to compute $E(t) = \int_0^t (I(u) - P_{diss}(u))du = \int_0^t R(u)du$. We can fix the zero energy level at will and by doing so, the mean value of the energy $\langle E \rangle$, which will be fixed at zero for simplicity.

1.2.1 Energy Fluctuations

The energy fluctuations can be calculated directly from Eq.(1.1) integrating it twice, giving the expression

$$\left\langle E^2 \right\rangle = \lim_{t\to\infty} 2 \int_0^t dt' \int_0^{t'} \langle R(t')R(s) \rangle \, ds, \tag{1.8}$$

which relates them directly to the time-integrated autocorrelation function of the forcing term $R(t)$. By the same arguments, we can calculate the n-th moment of the energy $\langle E^n \rangle$, but we will focus mainly on the *rms* fluctuations.

The fluctuations of global observables in a stationary state must remain bounded. To maintain the energy fluctuations bounded, we must impose certain conditions on the time-integrated autocorrelation of $R(t)$. As before, assuming an exponentially decreasing time correlation function $C_{RR}(t') \sim \sigma_R^2 \exp(-|t'|/\tau_R)$, Eq.(1.8) reads at a fixed time t,

$$\left\langle E^2 \right\rangle (t) = \sigma_R^2 \tau_R^2 (t/\tau_R - 1 + \exp(-t/\tau_R)). \tag{1.9}$$

For short times compared to the correlation time of the forcing $t \ll \tau_R$, $\langle E^2 \rangle$, which is related directly to the energy fluctuations, grows as $\sigma_R^2 t^2$ (balistic limit) and for long times $t \gg \tau_R$ they grow as $\sigma_R^2 \tau_R t$ (diffusive limit). For both of these limiting behaviors, the *rms* value of E diverges in the asymptotic limit $t \to \infty$.

One way to eliminate the divergence of the moments of E is to impose $\int_{-\infty}^{\infty} \langle R(0)R(s) \rangle \, ds = \sigma_R^2 \tau_R = 0$, meaning that the zero frequency part of the power spectral density $|\widehat{R}(\omega = 0)|^2$ must be zero. This can be understood from Eq. (1.8), arguing that if the integral of the autocorrelation function decreases fast enough we can separate the two integrals: one related to the zero-frequency

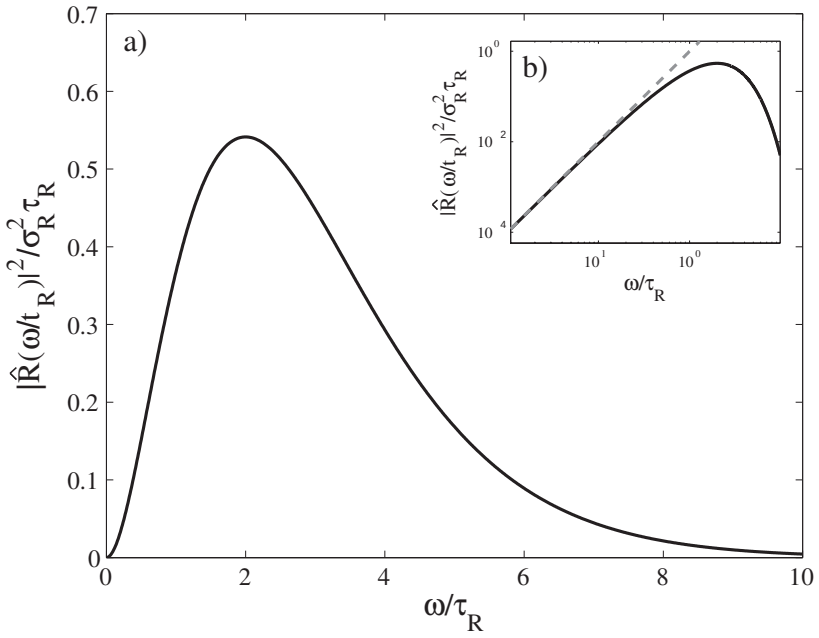

Figure 1.5: a) Functional form of the normalised power spectral density ($|\widehat{R}(\omega)|^2/\sigma_R^2\tau_R$ as a function of the normalised frequency ω/τ_R. b) Inset: Log-Log plot. The dashed line shows the asymptotic behavior $|\widehat{R}(\omega)|^2/\sigma_R^2\tau_R \to \omega^2$ close to $\omega = 0$.

part of the power spectral density and another that grows linearly in time. This is just the diffusive limit for long times, as it was already shown above. It is a strong assumption, because using the fact that the autocorrelation function is exponentially decreasing we can see from Eq. (1.9) that the *rms* value will not only be bounded, but actually zero. This means that the autocorrelation function of $R(t)$ does not behave as simply as a decaying exponential in any way. Using Eq. (1.1) and taking the Fourier transform $|\widehat{E}(\omega)|^2 = |\widehat{R}(\omega)|^2/\omega^2$, and integrating it in ω-space, we get

$$\langle E^2 \rangle = \int_{-\infty}^{\infty} \frac{|\widehat{R}(\omega)|^2}{\omega^2} d\omega. \tag{1.10}$$

With this expression we can study the *rms* fluctuations of E by means of the spectral properties of $\widehat{R}(\omega)$. If we assume that the forcing *rms* fluctuations $\langle R^2 \rangle$ are bounded and knowing that $|\widehat{R}(0)|^2 = 0$, we can assume that

$$\begin{aligned} \lim_{\omega \to 0} |\widehat{R}(\omega)|^2/\sigma_R^2\tau_R &\to \omega^{\alpha} \\ \lim_{\omega \to \infty} |\widehat{R}(\omega)|^2/\sigma_R^2\tau_R &\to \omega^{-(1+\beta)} \end{aligned} \tag{1.11}$$

with $\alpha, \beta > 0$. Including this in Eq. (1.10) and impossing bounded *rms* fluctuations of the energy, we see that $\alpha \geq 2$ to prevent divergences at zero frequency (that is, the diffusive limit). Indeed, due to the fact that R is real and assuming that it is bounded when $t \to \infty$, we can expand in series its power spectrum close to $\omega = 0$. From $|\widehat{R}(0)|^2 = 0$, we can assume that $|\widehat{R}(\omega)|^2 \sim \sigma_R^2\tau_R((\omega^2/\tau_R^2) + O((\omega/\tau_R)^4)$ when $\omega \to 0$. The typical shape of $|\widehat{R}(\omega)|^2$ following this limit in frequency is shown in Fig. (1.5).

Although all of these calculations are made for the case of constant dissipative power, the general relationships drawn for $R(t)$ and $E(t)$ can be applied for any type energy flux that satisfies Eq. (1.1), for instance when the dissipative power is proportional to the energy of the system, as we will study in the next parragraph.

1.3 Linear damping

Let us take Eq.(1.1) and assume that the dissipated power P_{diss} is proportional to the energy of the system $E \propto P_{diss}$, with a coefficient of proportionality with units of frequency called damping rate, much like the case of a damped brownian particle [13] or water surface waves in incompressible viscous fluids [15]. The balance equation (1.1) then reads

$$\frac{dE(t)}{dt} = I(t) - \gamma' E(t) \tag{1.12}$$

where the damping rate γ' does not depend on the energy of the system and will be regarded as a constant in the following calculations. It is straightforward to show that in the steady state $\langle E \rangle = \langle I \rangle / \gamma'$ and the initial conditions are lost after a characteristic time of order γ'^{-1}. Furthermore, due to the linearity of 1.12, we can integrate it directly to solve the linear differential equation. That means that for a given injection power process, all the cumulants and moments of the energy are just the integrated cumulants and moments of I with a certain weight function. This weight function is in this case a decreasing exponential $\exp[-\gamma' t]$where the damping rate takes the role of a characteristic correlation time of the dissipative process.

1.3.1 Energy Fluctuations

From the linear system, we compute the solution simply as

$$E(t) = \int_0^t I(t') e^{\gamma'(t-t')} dt'$$

where the initial condition of the energy are neglected in the stationary regime when a time of the order of $1/\gamma'$ has passed. For the second moment $\langle E^2 \rangle$, the expression reads

$$\left\langle E^2 \right\rangle = \lim_{t\to\infty} \int_0^t \int_0^t \langle I(u) I(v) \rangle \, e^{-\gamma'(t-u))-\gamma'(t-v)} du dv, \tag{1.13}$$

In the case where the autocorrelation function of I behaves exponentially, and assuming stationarity of the system, we have $C_{II}(t) = \sigma_I^2 \exp(-t/\tau_I)$, where $\sigma_I = \sigma_{P_{inj}}$ and $\tau_I = \tau_{P_{inj}}$. Computing now $\langle E^2 \rangle$ for the stationary regime, we get

$$\left\langle E^2 \right\rangle = \frac{\sigma_I^2 \tau_I}{\gamma'} + \frac{\langle I \rangle^2}{\gamma'^2} = \frac{\sigma_I^2 \tau_I}{\gamma'} + \langle E \rangle^2 \tag{1.14}$$

From the later equation, we can compute the standard deviation of E, which is simply $\sigma_E = \sigma_I \sqrt{\tau_I / \gamma'}$. For higher moments, i.e., $\langle E^n \rangle, n > 2$, we have to know in advance how the n-point correlation function of I behaves. For instance, the third order moment $\langle E^3 \rangle$ can be written as

$$\lim_{t\to\infty} \int_0^t \int_0^t \int_0^t \langle I(u) I(v) I(w) \rangle \, e^{-\gamma'(3t-u-v-w)} du dv dw$$

where we need explicitly the form of the 3-point correlation function of I.

In the frequency domain, we can also extract some interesting conclusions relating the power spectral densities of both the energy and the injected power. Taking the Fourier transform from Eq.(1.12), we have

$$-i\omega \widehat{E}(\omega) + \gamma' \widehat{E}(\omega) = \widehat{I}(\omega).$$

From the absolute value of the Fourier transform of the energy $|\widehat{E}(\omega)|^2$, we find

$$|\widehat{E}(\omega)|^2 = \frac{|\widehat{I}(\omega)|^2}{\omega^2 + \gamma'^2}, \tag{1.15}$$

which means that the autocorrelation function of E is given by the Fourier transform of Eq. (1.15), and, using the Wiener-Khinchin theorem, we also have

$$\int_{-\infty}^{\infty} (\langle E(t)E(0)\rangle - \langle E\rangle^2)dt = \frac{1}{\gamma'^2}\int_{-\infty}^{\infty} (\langle I(t)I(0)\rangle - \langle I\rangle^2)dt,$$

which is just Eq. (1.6), written for a dissipated power proportional to the energy. In fact, supposing exponentially decreasing autocorrelation functions for both observables, this gives

$$\sigma_E^2 = \sigma_I^2 \tau_I/\gamma'.$$

Thus, in the case where P_{diss} is proportional to E, the main parameters controling the energy fluctuations are the zero-frequency component of the power spectral density of I and the damping rate γ', which acts as an impedance to the energy flux input. This type of dissipative power dependence on the energy will be further studied in the next chapter.

1.3.2 Injection and Dissipation Correlations

Time and space correlations are indeed present in out-of-equilibrium systems and have important effects on the dynamics of the internal degrees of freedom. Using (1.12) we can also study the cross-correlation functions of injection and dissipation. The non-zero correlation of both observables is clear from the fact that E and its moments depend linearly on I, mainly because

$$C_{IP_{diss}}(t) = \langle I(0)P_{diss}(t)\rangle - \langle I\rangle^2 = \int_0^t (\langle I(0)I(t')\rangle - \langle I\rangle^2)e^{-\gamma'(t-t')}dt'.$$

In the case of exponentially decreasing autocorrelation functions, this is just the integration of two decreasing exponentials with caracteristic times τ_I and $\tau_{diss} = \gamma^{-1}$.

Straightforward calculations lead to the function $C_{IP_{diss}}(t) = \sigma_I^2 f(t)$, with

$$f(t) = \frac{\gamma'\tau_I}{\gamma'\tau_I - 1}(\exp[-t/\tau_I] - \exp[-\gamma' t]),$$

which is always possitive, as shown in Fig.(1.6). It has a maximum that decreases when $\gamma'\tau_I$ grows. This means that I and P_{diss} lose their statistical dependence when their time scales begin to separate. We can also show that the correlation time t^*/τ_I for the pair of variables, i.e. where $C_{IP_{diss}}$ is maximum, grows logarithmically in the normalised time variable t/τ_I as a function of $\gamma'\tau_I$, as shown in Fig.(1.7).

1.4 Conclusions

In this Chapter we have shown several examples and simple systems where the energy balance equation takes part in describing the interaction of injected power $P_{inj} = I$ and dissipated power P_{diss} when a dissipative system is maintained in an out-of-equilibrium stationary state. Although dissipation is hard to measure (and in some cases even not accessible), certain relationships can be sorted out, by acknowledging the fact that the injected power furnished by the forcing device has to be dissipated. Correlation times and standard deviations of both observables can be related and, in some cases, even restrictions for them can be given.

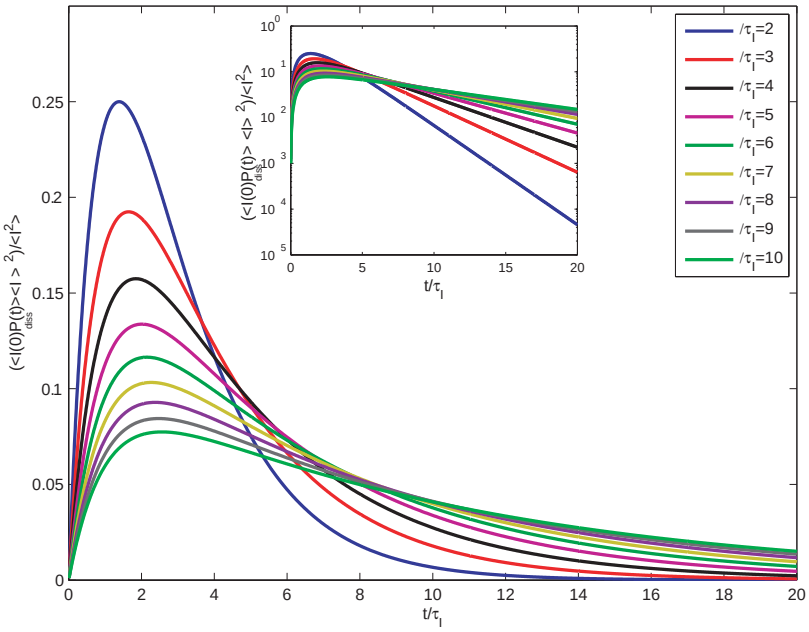

Figure 1.6: Normalised cross correlation function $f(t)$ as a function of the normalised time t/τ_I. Inset: Log-log plot of $f(t)$.

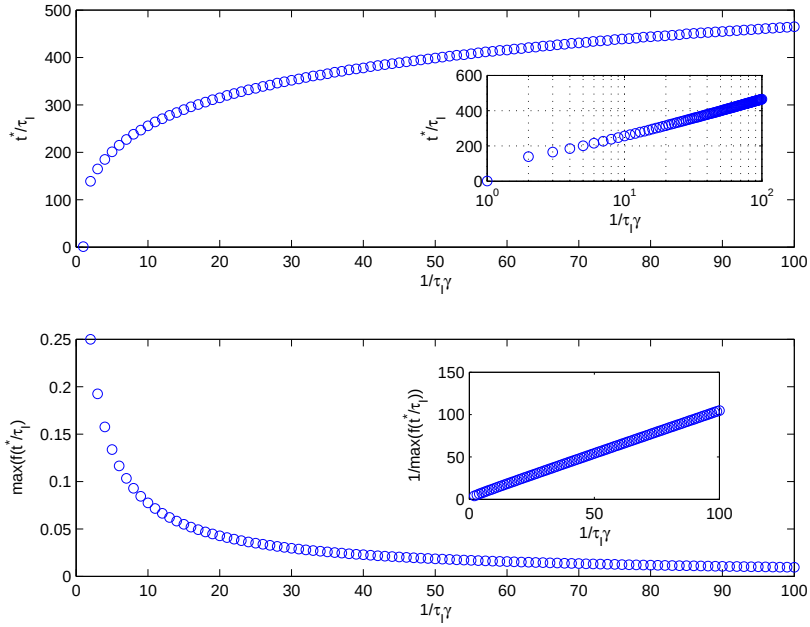

Figure 1.7: Functional dependence of the normalised correlation time t^*/τ_I (Inset: Semilog plot of t^*/τ_I) and the maximum of the cross correlation function $max(f(t^*/\tau_I))$ (Inset: Inverse of $max(f(t^*/\tau_I))$) versus the dimensionless parameter $1/\tau_I\gamma'$.

Bibliography

[1] Uriel Frisch, *Turbulence: The Legacy of A. N. Kolmogorov* (Cambridge University Press, New York, 1996)

[2] R. Labbé, J. F. Pinton and S. Fauve, J. Phys. II France **6** (1996) pp. 1099-1110; F. Petrelis *et al.*, Phys. Rev. Lett. **90**, 174501 (2003)

[3] E. Falcon, S. Aumaitre, C. Falcón, C. Laroche, S. Fauve , Phys. Rev. Lett. **100**, 064503 (2008)

[4] S. Aumaître, PhD thesis, Ecole Normale Supérieure de Lyon, March 1999; S. Aumaître, S. Fauve, S. McNamara and P. Poggi, Eur. Phys. J. B, **19** 449 (2001).

[5] P. Visco, PhD thesis, Université Paris VI Pierre et Marie Curie, June 2007

[6] S. Aumaître, A. Alastuey, S. Fauve, Eur. Phys. J. B **54**, 263 (2007)

[7] P.G. Drazin ann W.H. Reid, *Hydrodynamic stability* (Cambridge University Press, New York, 1981)

[8] Xia *et al.*, Phys. Rev. Lett. **90**, 074501 (2003)

[9] R. Labbé in *Instabilities and Nonequilibrium Structures IX (Nonlinear Phenomena and Complex Systems)* edited by Orazio Descalzi, Javier Martínez, Sergio Rica (Kluwer Academic Publishers, U.S.A., 2004) pp. 209-217.

[10] S. Aumaitre and S. Fauve, *Europhys. Letters*, **62** 822-828 (2003).

[11] N. G. Van Kampen, *Stochastic Processes in Physics and Chemistry*, Academic Press, New York (1992).

[12] J. Farago, Physica A, **331** 69-89 (2004)

[13] P. Langevin, C. R. Acad. Sci. (Paris) **146**, 530 (1908); for an english translation, see D. S. Lemons, and A. Gythiel, Am. J. Phys. **65**, 1079 (1997)

[14] G.I. Taylor, Proc. London Math. Soc. **20** (1921), p. 196

[15] L. D. Landau and E. M. Lifshitz, *Couse of Theoretical Physics, Volume 6* (2nd English edition, Pergamon Press, 1987)

Chapter 2

Injected Power into randomly forced dissipative systems in stationary out-of-equilibirum states

In this Chapter we study the statistical properties of the injected power I into a dissipative system in the case where the forcing driving the system into a steady out-of-equilibrium state can be modelised by a random Gaussian noise with a characteristic time scale. In Section 2.1 and Section 2.2 we set the theoretical background for the calculation of the injected power fluctuations in this simple model. In Section 2.3 we study experimentally this type of forcing in an electronic RC circuit, where the random forcing is externally controlled. The probability density function (PDF) of the injected power displays exponential tails and a cusp close to $I = 0$. This PDF can be computed and is generic since it appears in several systems driven out of equilibrium, as we wil show in Section 2.4.

2.1 Langevin equation with random forcing

The injected power I provides a permanent energy input into a dissipative system, in order to maintain it in a dynamical state, different from the one at equilibrium. It has been often considered theoretically as a constant input parameter in out-of-equilibrium systems (for instance in the approach of Kolmogorov of fully developed turbulence [1]). However, even when the number of components or degrees of freedom of the system under study is large, I can fluctuate strongly and rearding it as a constant is nor realistic neither suited for its description.

Its mean value $\langle I \rangle > 0$ cannot be fixed solely by the external forcing: it depends on the impedance of the system. As shown in the previous chapter, its *rms* fluctuations have to satisfy certain constrains in order to maintain the forced system in a statistically stationary out-of-equilibrium state. In certain simple limits, it controls the internal energy fluctuations and its higher moments. It is then an interesting question to study the statistical properties of the injected power I and its relation to the internal energy fluctuations.

To do so, we will study one of the simplest dissipative systems, described by a linear Langevin equation. Although it is the canonical example of fluctuations in equilibrium statistical mechanics [2] describing the thermalization of a brownian particle, it can also be envisioned as a strongly out-of-equilibrium system [3], as we will show below.

We will use a simple model where the response of the system to a random forcing follows the

linear Langevin equation

$$\frac{dv(t)}{dt} = -\gamma v(t) + f(t), \tag{2.1}$$

as one of the simplest dissipative system, where $v(t)$ is the response of the system (for instance, the velocity of a damped particle [4], γ is the damping rate coefficient and $f(t)$ is a random forcing. This modelisation only assumes that the response of the system is proportional to the forcing (mainly that the *rms* fluctuations of v are proportional to the *rms* fluctuations of f). Eq. (2.1) is clearly dissipative and can be written as an energy balance equation by multiplying it by $v(t)$. The energy of the system $E = v^2/2$ is pumped by the injected power $I = fv$ and later dissipated, $P_{diss} = \gamma v^2 = 2\gamma E$. In a stationary out-of-equilibrium state, dissipation is proportional to the energy of the system, therefore the general relationships presented in the previous Chapter hold.

This simple system was first studied as a simple dissipative system by Farago [3] for forcing f which is a gaussian white noise (with zero correlation time) and later for a colored noise (non-zero correlation time) with a given autocorrelation function. Here, we will take the forcing f acting on the system to be an Orstein-Ulhembeck (O-U) type of noise with an exponentially decreasing autocorrelation function satisfying, thus

$$\frac{df(t)}{dt} = -\lambda f(t) + \zeta(t). \tag{2.2}$$

where $\zeta(t)$ is a gaussian white noise with zero mean value and autocorrelation function $\langle \zeta(t)\zeta(t') = D\delta(t-t')$. Here, D is the noise intensity and $\delta(t)$ is the delta function satisfying $x(t) = \int_\Omega x(t')\delta(t-t')dt'$, when $t \in \Omega$ and zero otherwise. In that sense the forcing f and the response v follow the same type of equation. For the forcing f satisfying Eq.(2.2) the autocorrelation function is $\langle f(t)f(t')\rangle = \frac{D}{\lambda}e^{-\lambda|t-t'|}$.

Both variables f and v are by no means statistically independent. This comes from the fact that $\langle I\rangle = \langle fv\rangle$ is positive in order to maintain the system in an out-of-equilibrium state. Given the linearity of the Eq. (2.1), we can calculate explicitly $\langle I\rangle$.

We will study the injected power fluctuations in this system in the next section. We will see that they present large exponential tails and a cusp near $I \simeq 0$. Given the fact that the system is in a stationary state and both variables are gaussian, we will also calculate explicitly the injected power PDF, as shown in the next section.

2.2 Calculation of the Probability Density Function of the Injected Power

Supposing that the forcing f on the system is a random gaussian noise with zero mean and due to the linearity of Eq.(2.1), so will be v. The fluctuations of both variables can be described by a joint Probability Density Function (PDF) $\mathcal{P}(v, f, t)$, which can be calculated from the Fokker-Planck equation [6] of the system. This procedure is explained in the Appendix. In the stationary limit, $\mathcal{P}(v, f)$ reads

$$\mathcal{P}(v,f) = \frac{1}{2\pi\sigma_v\sigma_f(1-r^2)^{1/2}} \exp\left[-\frac{1}{2(1-r^2)}\left(v^2/\sigma_v^2 - 2rvf/(\sigma_v\sigma_f) + f^2/\sigma_f^2\right)\right].$$

Here σ_v and σ_f are the *rms* fluctuations of v and f respectively and r is the normalised correlation coefficient $r = \langle vf\rangle/(\sigma_v\sigma_f)$. From Eqs.(2.1) and (2.2), we can compute directly these coefficients as

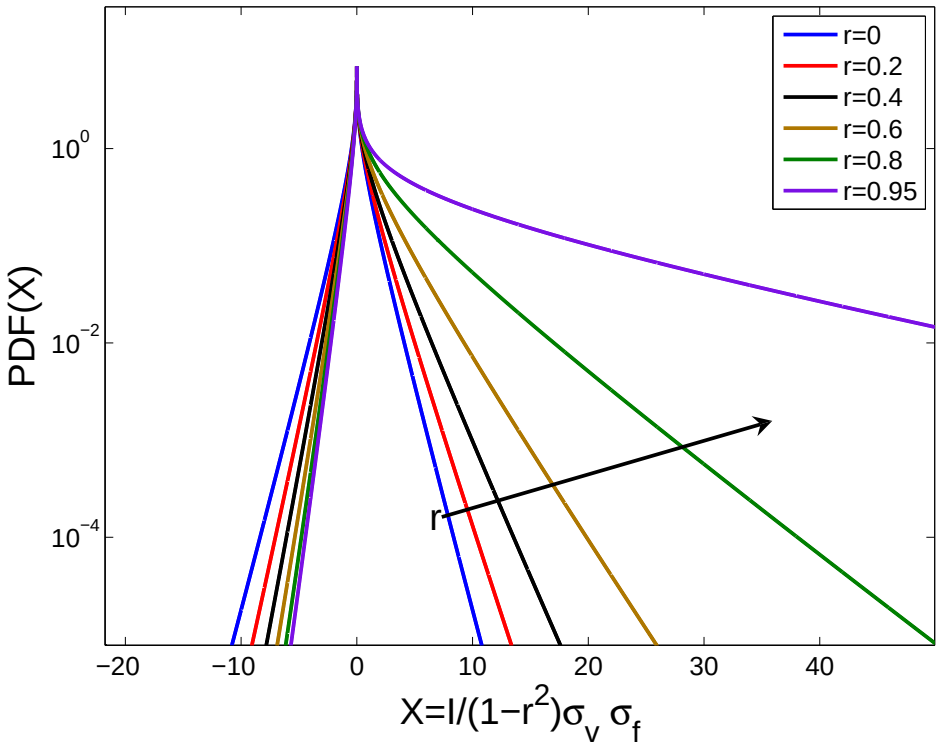

Figure 2.1: PDF of $X = I/(1-r^2)\sigma_v\sigma_f$ for different values of r. The arrow shows increasing values of r at fixed values of σ_v, σ_f.

functions of D, λ and γ as

$$\sigma_f = \sqrt{\frac{D}{2\lambda}}, \tag{2.3}$$

$$\sigma_v = \sqrt{\frac{D}{2\lambda\gamma(\lambda+\gamma)}}, \tag{2.4}$$

and

$$r = \frac{\langle I \rangle}{\sigma_v\sigma_f} = \sqrt{\frac{\gamma}{\gamma+\lambda}} \tag{2.5}$$

The normalised correlation coefficient r is also the normalised mean injected power into the dissipative system. This coefficient must be positive (in order to inject energy into the system) and smaller than 1 due to the Cauchy-Schwartz identity [5] $\langle fv \rangle \leq \sqrt{\langle v^2 \rangle \langle f^2 \rangle}$. Integrating directly the expression of $\mathcal{P}(f, v)$ to calculate the mean values of v or f gives $\langle v \rangle = \langle f \rangle = 0$.

From the expression of the joint PDF, we can integrate directly the PDF of the injected power I. To do so, we change variables from v and f to $I = fv$ and $u = v$, for example. The calculations are straightforward, giving the expresion for the PDF of I

$$P(I) = C \exp\left(r\frac{I}{(1-r^2)\sigma_v\sigma_f}\right) K_0\left(\left|\frac{I}{(1-r^2)\sigma_v\sigma_f}\right|\right), \tag{2.6}$$

where $C = (\pi\sigma_v\sigma_f\sqrt{1-r^2})^{-1}$ is a normalisation constant and $K_0(x)$ is the zeroth order modified Bessel function of the 2nd kind. In the normalised variable $X = I/[(1-r^2)\sigma_v\sigma_f]$, we can see that the

only parameter that controls the assymetry of the PDF is the correlation coefficient r, related directly to the mean dissipated power $\langle D \rangle = \langle I \rangle$. For a given value of r, we show in Fig.(2.1) the typical shape of the PDF of the injected power fluctuations for a system described by Eqs. (2.1) and (2.2). Knowing the PDF of the injected power, all of its moments and cumulants can be directly computed, as it is shown in the Appendix. For instance, the first 4 moments are $\langle I \rangle = r$, $\langle I^2 \rangle = 1 + 2r^2$, $\langle I^3 \rangle = 9r + 6r^3$ and $\langle I^4 \rangle = 9 + 72r^2 + 24r^4$.

For any value of $r \in (0, 1)$, the cusp at zero can be also deduced from the asymptotic behavior of $K_0(x)$, because $\lim_{x \to 0} K_0(x) \sim -\log(x)$. The PDF displays large exponential asymmetric tails and a cusp near $I = 0$. We can estimate both exponential tails using the assymptotic behavior of

$$\lim_{x \to \infty} K_0(x) \sim \exp(-x),$$

which means that the PDF of X can be computed, using the steepest descent method as

$$P(X) = C' \frac{\exp\left(rX - |X|\right)}{\sqrt{|X|}}, \tag{2.7}$$

with C' a normalisation constant. We refer to the Appendix for this calculation. From ths approximate expression both exponential tails are

$$P(X) \;\; \rightarrow \;\; \exp\left(-(1-r)X\right) \quad \text{for} \;\; X > 0 \tag{2.8}$$

$$P(X) \;\; \rightarrow \;\; \exp\left(-(1+r)\,|X|\right) \quad \text{for} \;\; X < 0. \tag{2.9}$$

The limiting cases where $r = 0$ and $r = 1$ can be understood as follows. When $r = 0$, both variables v and f are statistically independent and no correlation between them exists. In this case the PDF of X is symmetric with respect to zero (see Fig. (2.1)), as it is for $K_0(|X|)$ which behaves as an exponential function for large X. In this limiting case no mean injected power enters the system, hence it cannot be viewed rigorously as an out-of-equilibrium system. When $r = 1$, both variables are statistically dependent in the sense that $v \propto f$ and the PDF of X is the PDF of a squared gaussian random variable, therefore it follows a χ-square distribution of 1 degree of freedom. In this case the χ-square distribution displays an exponential tail for positive events and no negative events occur.

2.3 Injected power into a simple experimental system: RC circuit

To test the later theoretical results, we can use a simple physical system: an electronic circuit with a resistor of resistance R in series with a capacitor of capacitance C, which is submitted to a stochastic voltage $\zeta(t)$, as shown in Fig. (2.2).

The voltage continuity equation, applied to the circuit reads (see Chapter 2)

$$\gamma^{-1} \frac{dV(t)}{dt} + V(t) = \zeta(t), \tag{2.10}$$

where $RC = \gamma^{-1}$. The quasi-gaussian stochastic forcing $\zeta(t)$ is generated by a Spectrum Analyzer (Hewlett-Packard HP 35670A). This noise is low-pass filtered at a cut-off frequency λ fixed to 5 kHz, unless specified otherwise. The control parameter of this system is the noise amplitude D defined by the constant value of its power spectral density, as an analogy to the white noise limit. C is

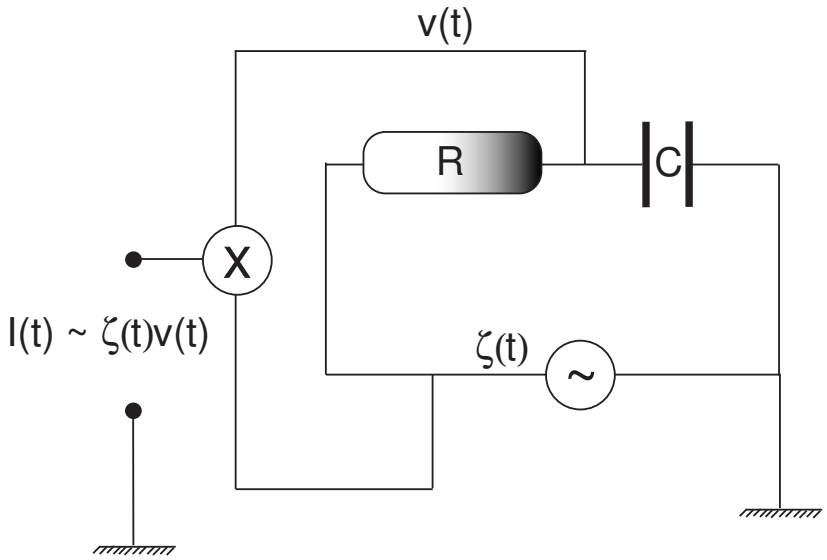

Figure 2.2: Electronic RC dipole submitted to a stochastic voltage $\zeta(t)$.

fixed to 1 μF, and R can be varied between 200 Ω and 10 kΩ leading to values of γ from 50 Hz to 10 kHz. The output $V(t)$ of the RC circuit is multiplied by the random forcing $\zeta(t)$ by means of an analog multiplier (Analog Devices AD540). The resulting voltage $V(t)\zeta(t)$ is proportional to the injected power (as it was shown in Chapter 1) and it is acquired with a Digital-to-Analog Acquisition card (AT-MIO-16X) at 100 kHz sampling frequency for 10 s, with a resolution of 0.3 mV. This simple system mimics the Langevin equation of a brownian particle, submitted to a random forcing. Multiplying the latter equation by $V(t)$ leads to the same fundamental balance equation (Eq. (1.1)), where the energy of the system $E(t) = \frac{1}{2}V(t)^2$, $I(t) = \gamma\zeta(t)V(t)$ and $P_{diss}(t) = \gamma V(t)^2 = 2\gamma E(t)$. The analog multiplication gives directly $\zeta(t)V(t)$, which is proportional to $I(t)$.

A typical temporal trace of the normalised injected power $I/\langle I\rangle$ is displayed in Fig.(2.3). Quiescent periods with a small amount of injected power are observed and interrupted by bursts where $I(t)$ can take both positive and negative values, although $\langle I\rangle \geq 0$. These fluctuations are large with respect with the mean value, equal to $\langle I\rangle$=6.6 x 10^{-2} Vrms^2 Hz.

The aim is now to study the probability distribution function (PDF) of these injected power fluctuations in the RC circuit.

2.3.1 Statistical properties of the Injected Power

We study in this section the statistical properties of the injected power through its probability density function. The PDF of the injected power, I, is shown in Fig.(2.4) for different values of the noise amplitude D, and the damping rate γ. For all values of D and γ, the PDFs exhibit two asymmetric exponential tails and a cusp near $I \simeq 0$. As shown in Fig.(2.4), the PDF asymmetry increases strongly with γ at fixed D. Moreover, the extremal fluctuations increase strongly with D at a fixed γ.

At a fixed value of γ, the PDFs of I are plotted in Fig. (2.5) for 9 different increasing noise amplitudes. As shown in the inset of Fig. (2.5), all these PDFs collapse on the same curve when plotted in the centered-reduced variable, $(I-\langle I\rangle)/\sigma_I$, where σ_I is the *rms* value of I, and $\langle I\rangle$ its mean value. Such a collapse means that all the moments of I scale as σ_I. As shown in Fig.(2.6), σ_I (as well as $\langle I\rangle$) scales linearly with D. This linear dependence with D of the moments of I can be recovered

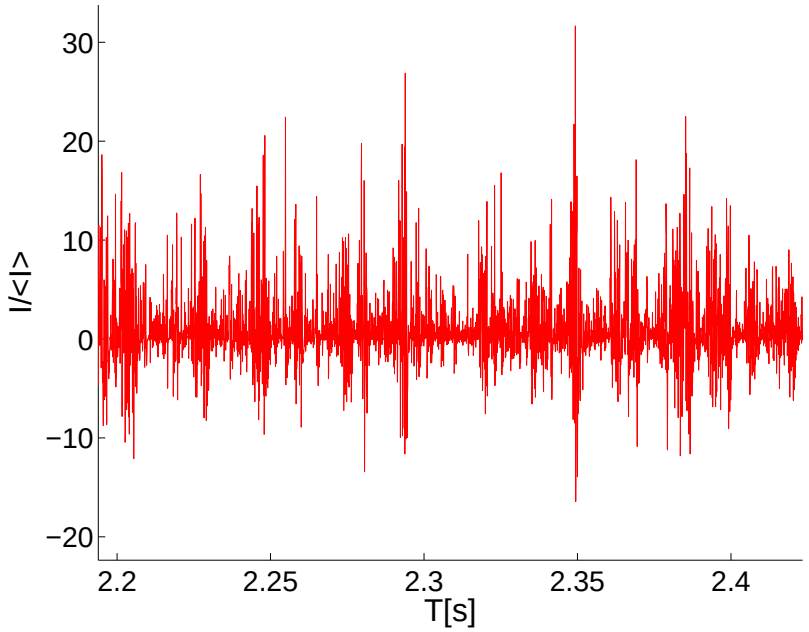

Figure 2.3: Temporal trace of the normalised injected power $I/\langle I\rangle$ in the RC circuit over 0.5 s (D= 1.56 x 10^{-3} Vrms^2/Hz,γ = 200 Hz, λ=5 kHz). $\langle I\rangle$=6.6 x 10^{-2} Vrms^2 Hz.

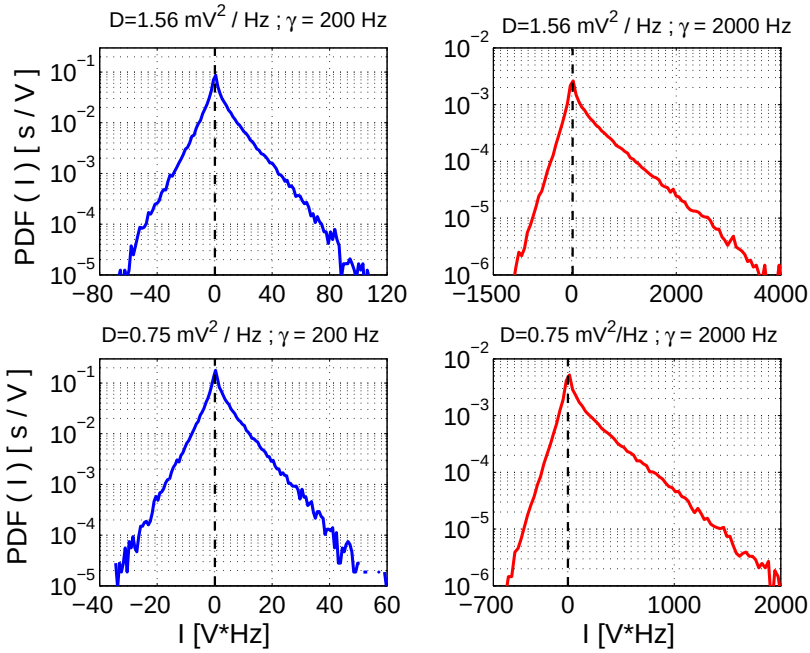

Figure 2.4: Probability density functions of the injected power I for two different noise amplitudes (D = 7.55 x 10^{-4}, 1.56 x 10^{-3} Vrms^2/Hz), and damping rates (γ = 200, 2000 Hz).

by dimensional analysis from the linear Langevin Eqs. (2.1) and (2.2). Due to the linearity of this set of equations, the *rms* fluctuations of the forcing σ_f are proportional to D, and the *rms* fluctuations of the forcing σ_v are proportional to the ones of the σ_f, and hence $\sigma_v \propto \sigma_f$. Consequently, $I \propto D$, and all of its higher order moments follow a similar scaling $\langle I \rangle^n \propto D^n$. Following this reasoning, the slopes of the exponential tails scale as D^{-1}, so when the noise amplitude D is doubled, the typical fluctuation scale of I is doubled.

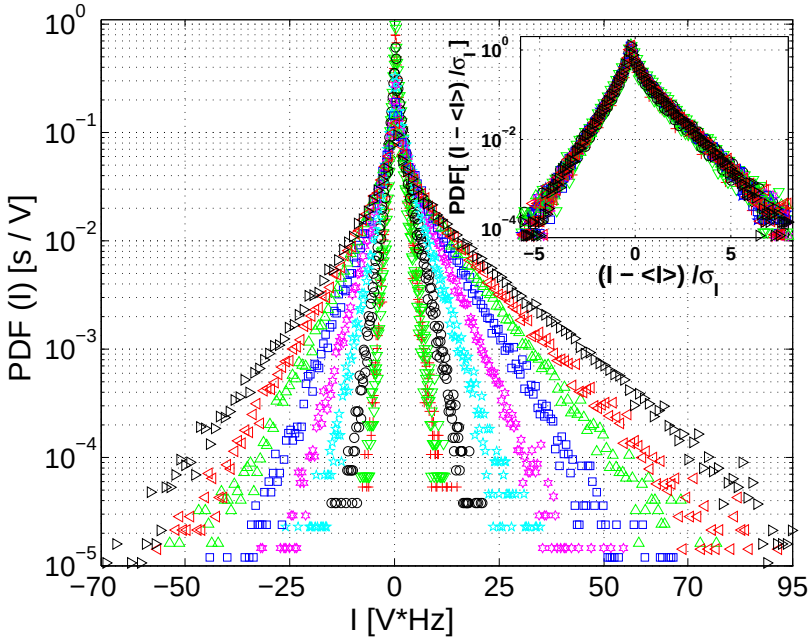

Figure 2.5: Probability density functions of injected power, I, for $D = 0.06$ (+) to 1.56 (▷) x 10^{-3} V^2_{rms}/Hz, for $\gamma = 200$ Hz. Inset: Probability density functions in the re-scaled variable $(I - \langle I \rangle)/\sigma_I$.

The noise amplitude D is now fixed in order to study the effect of the damping rate γ on the injected power fluctuations. For different values of γ, $\langle I \rangle$ and σ_I are plotted in Fig.(2.6). Both scale as power laws of γ with two different exponents. As they scale differently with γ, no collapse occurs when the PDFs of I are plotted in the centered-reduced variable for differents values of γ. However, as displayed in Fig.(2.8), both the exponential tails of positive and negative values of I show power law dependences with γ. The slope of the positive exponential tails scales like $\sim \gamma^{-1.65\pm0.05}$, whereas the negative one scales like $\sim \gamma^{-1.33\pm0.05}$. This means that the probability of having negative values of injected power decreases faster than the probability of having positive ones as the system becomes more and more dissipative. As γ increases, the correlation time of the voltage $V(t)$ decreases, making the random voltage $\zeta(t)$ and the voltage $V(t)$ more and more dependent of each other, increasing their correlation coefficient $r = \langle I \rangle / \sigma_V \sigma_\zeta$. Therefore, as γ is increased, the negative fluctuations of the injected power tend to zero.

Taking into account both the effects of D and γ, the PDF of the positive values of I behaves, far from the cusp at $I \simeq 0$, as

$$P_+(I) \sim \exp\left(-\alpha_+ \frac{I}{D\gamma^{1.65}}\right). \tag{2.11}$$

Similarly, the PDF of the negative values of I behaves as

$$P_-(I) \sim \exp\left(\alpha_- \frac{I}{D\gamma^{1.33}}\right) \tag{2.12}$$

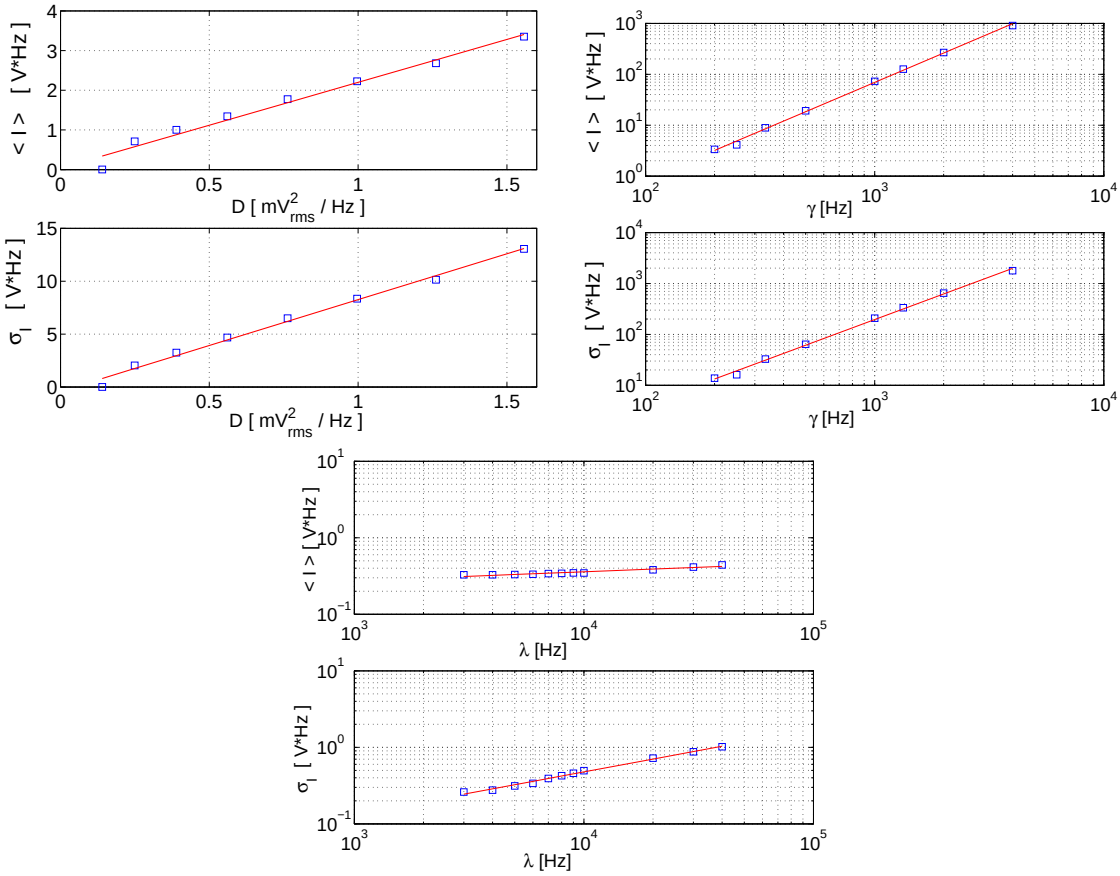

Figure 2.6: **Top Left:** Mean $\langle I \rangle$ and standard deviation σ_I of the injected power as linear functions of the noise amplitude D. $\gamma = 200$ Hz. **Top Right:** Mean $\langle I \rangle$ and standard deviation σ_I of the injected power as a function of the damping rate γ. $D = 0.75$ x 10^{-3}V^2/Hz and $\lambda = 5$ kHz. $(-)$: linear best fits of slopes 1.9 V and 1.59 V, respectively. **Bottom Center:** Scaling of the mean $\langle I \rangle$ and standard deviation σ_I with the cut-off frequency λ. $D = 0.75$ x 10^{-3}V^2/Hz and $\gamma = 200$ Hz.$(-)$: linear best fit of slopes 0.11 V and 0.56 V, respectively.

where $\alpha_\pm$ are two constants.

The experimental shape of the distribution of injected power can be compared with the prediction of Eq.(2.6). Here, there are no adjustable parameters. This is shown in Fig.(2.7) for two different values of γ. The computed PDFs display a cusp at $I = 0$ and exponential asymmetrical tails for large values of I in good agreement with the experimental shapes. As shown in Fig.(2.7), increasing the damping rate γ with all the other parameters fixed leads to more and more asymmetrical PDFs with less and less negative events. The asymmetry then increases when the damping rate γ increases. The asymmetry or skewness of the injected power distribution is then controlled by the damping parameter γ, or said differently, on the mean dissipated power.

Let us now have a look on the scaling of first cumulants ($\langle I \rangle$ and σ_I) with the parameters D, γ and λ. For D and γ fixed, we study the effect of the the random noise cut-off frequency λ on $\langle I \rangle$ and σ_I. As shown in Fig.(2.6), when λ is varied from 3 kHz to 40 kHz, the mean injected power slightly increases with λ, whereas σ_I scales as the square root of λ.

Thus, one has experimentally that the two first cumulants of the injected power can be written as a function of D, γ and λ as

$$\langle I \rangle \sim D\gamma^{1.90} \quad \text{and} \quad \sigma_I \sim D\gamma^{1.59}\lambda^{0.50}. \tag{2.13}$$

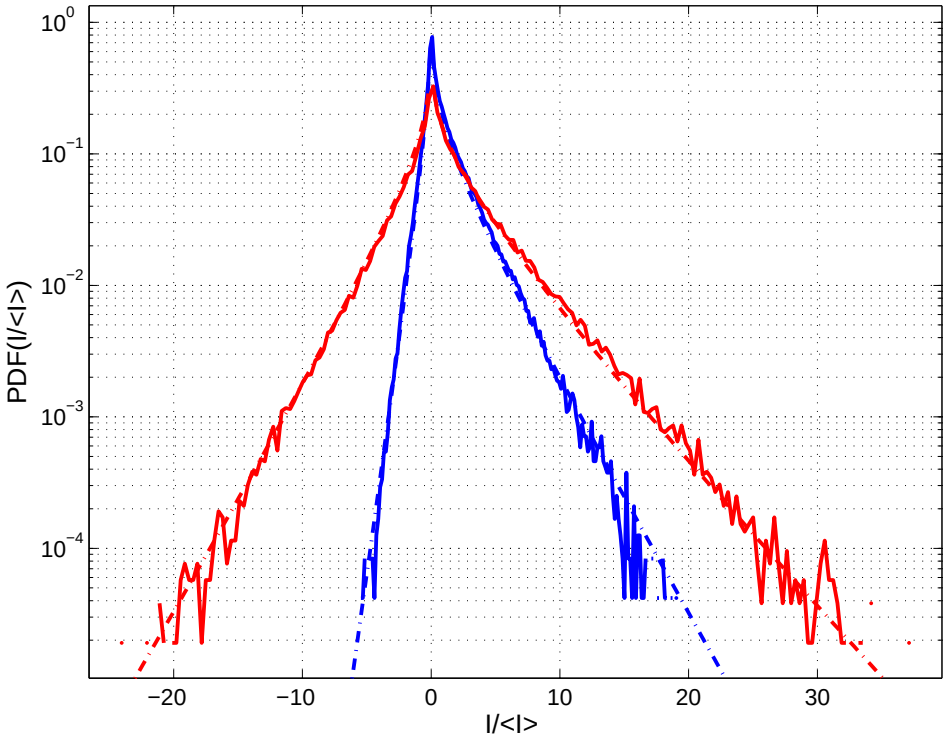

Figure 2.7: PDFs of $I/\langle I\rangle$: Comparison between experiment $(-)$ and theory $(--)$ for two different values of the damping rate $\gamma = 2000$ Hz $(\frac{<I>}{\sigma_V \sigma_\zeta} = 0.45)$ (blue) and $\gamma = 200$ Hz $(\frac{<I>}{\sigma_V \sigma_\zeta} = 0.15)$ (red). The cut-off frequency λ is fixed to 10 kHz.

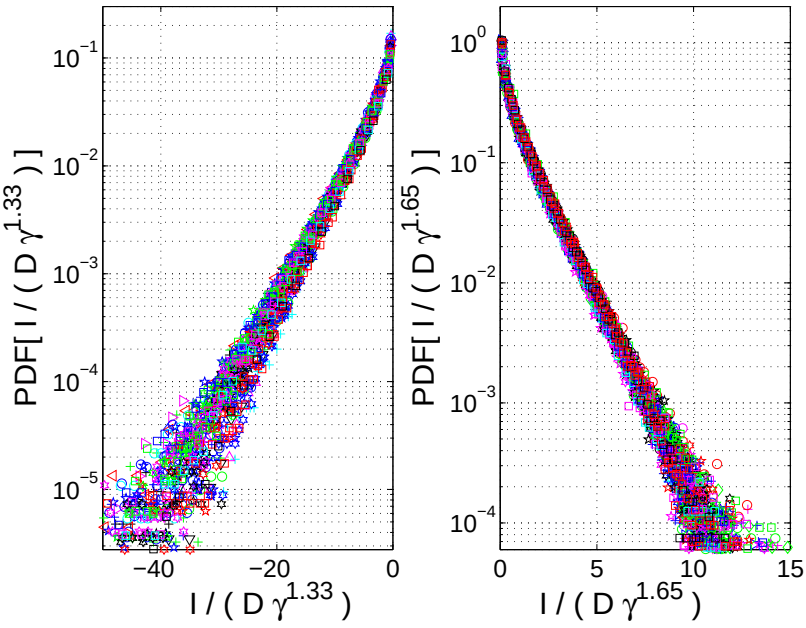

Figure 2.8: Scaling of the PDFs of the negative values (left) and the positive values (right) of injected power I, for 9 values of D, and 10 values of γ at fixed λ= 5 kHz.

All these exponents are measured with a precision of ± 0.05. Thus, the noise amplitude D is found to drive the scale of the injected power fluctuations whereas the damping rate γ controls the asymmetry of the PDF of I for a fixed correlation time λ^{-1}.

Theoretically, one can calculate the mean and *rms* values of I directly from the PDF of Eq.(2.6) (or from the set of Eqs.(2.1) and (2.2) by direct integration). They can be written, in the stationary limit, as[6]

$$\langle I \rangle = \gamma^2 \frac{D\lambda}{\lambda + \gamma}, \tag{2.14}$$

$$\sigma_I = \gamma^2 \frac{D\lambda}{\lambda^{1/2}\gamma^{1/2}}. \tag{2.15}$$

In the limit $\gamma/\lambda << 1$, Eq. (2.14) yields

$$\langle I \rangle \sim D\gamma^2, \tag{2.16}$$

which does not depend on the cut-off frequency λ, and Eq. (2.15) yields

$$\sigma_I \sim D\gamma^{3/2}\lambda^{1/2} \tag{2.17}$$

The range of γ used experimentally is between 50 and 2000 Hz, and the frequency cut-off λ is in the range from 3 kHz to 40 kHz. This leads to $\gamma/\lambda \sim 0.1$ in the worst case. The first two cumulants of Eqs. (2.16) and (2.17) derived from the O-U process thus are in good agreement with the experimental results of Eqs. (2.13).

2.4 Application to various systems

The typical shape of the PDF of I can be found in several systems submitted to a random forcing. Even when the forcing is not completely gaussian, some features are generic, being mainly the exponential tails and cusp near zero, the sole contol parameter is the mean injected power. We present some of these systems in the following section.

2.4.1 Wave turbulence

Wave Turbulence deals with the statistical steady state of a set of weakly nonlinear interacting waves, whose properties will be explained in Chapter 6. To drive this state, a constant input of energy must be supplied. Theoretically, only the mean flux of energy $\langle I \rangle$ has been considered and is seen as a control parameter. However, experimentally large fluctuations of I appear and, moreover, the mean flux is determined by the system itself balancing injection and dissipation. Here, we present two wave turbulence experiments where this point is studied in the frame of random forcing.

Wave Turbulence experiments in water and mercury:

A wavemaker is used to generate waves at the surface of a fluid that can display out-of-equilibrium stationary states such as wave turbulence [7]. The velocity $V(t)$ of the wave maker and the force $F_A(t)$ applied by the moving blade of the wavemaker are measured simultaneously. The velocity $V(t)$ of the wave maker is measured using a coil placed on the top of the electromagnetic shaker (B

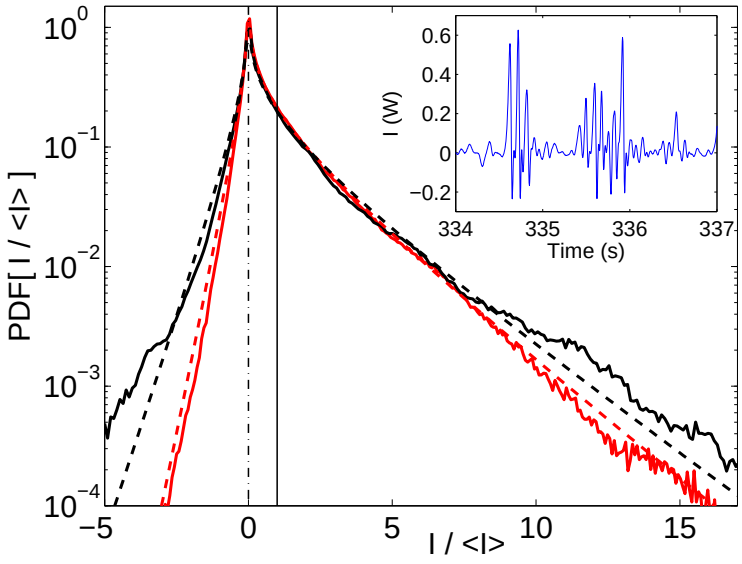

Figure 2.9: PDF on the power injected by the random vibrations of a wavemaker into the surface wave turbulence for experiments in small (black) and large (red) container of mercury (from [7]). Data are normalized by their mean value $\langle I \rangle = 0.05$ W. The forcing is a gaussian low frequency noise of bandwidth $[0, 6]$ Hz. Dashed line fits correspond to the formula (2.6). Vertical full and dashed lines show the corresponding average and most probable value. Inset: Temporal trace of the injected power over 3 s and $\langle I \rangle = 0.05$ W.

& K 4809). This shaker drives the wavemaker with a low-frequency gaussian random noise. The induced voltage generated by the moving permanent magnet of the vibration exciter is proportional to the excitation velocity. The force $F_A(t)$ applied by the electromagnetic shaker to the wave maker is measured by a piezoresistive force transducer (FGP 10 daN). Both signals display statistics close to gaussian of zero mean value.

For a given forcing with a low-pass filtered bandwidth, the *rms* value of velocity is proportional to the applied tension driving the shaker and does not depend on the fluid density ρ. The force *rms* fluctuations, on the contrary, increases with increasing fluid density. The power injected into the fluid by the wave maker is $I(t) \equiv -F_R(t)V(t)$ where $F_R(t)$ is the force applied by the fluid on the wave maker. This value generally differs from the measured one, $F_A(t)V(t)$ because of the piston inertia, comparable in some cases with the one of the fluid (in the case of water) which is been pushed. The mean values of $F_R(t)V(t)$ and $F_A(t)V(t)$ are the same, though. Keeping this in mind, we have also measured the acceleration of the piston $\dot{V}$ to deduced the force exerced over the wavemaker from Newton's law

$$M\dot{V} = F_A(t) + F_R(t),$$

for the piston of mass M. In the case of mercury, $M\dot{V}$ is negligible and $I(t)$ can be estimated accurately by $-F_A(t)V(t)$. In the case of water, inertia has to be taken in to account in computing the fluctuating values of the injected power.

The fluctuating injected power displays bursts and large fluctuations with respect to the average injected power $\langle I \rangle$. Figure (2.9) shows the PDF of the injected power for two different experimental configurations. Here, the main change in the experimental conditions is the size of the containers. For the computed curves, the working fluid is mecury (density $\rho = 13.6$ x 10^4 kg/m^3, kinematic viscosity

ν= 1.2 x 10^{-7} m^2/s and surface tension σ= 0.4 N/m). Once again, we see a cusp at $I \simeq 0$ and asymmetric tails. Using the acquired traces of both $F_A(t)$ and $V(t)$, we compute the mean injected power and their correlation coefficient r. For the small container $r \sim 0.6$ and for the large container $r \sim 0.7$. Using this information we can compare these PDFs with the computed ones (Eq.(2.6)). There is a good agreement between theoretical and experimental results, although we can see that in the smaller container the tails slightly depart from exponential fit. There is no asjustable parameter being used in this comparison.

Wave Turbulence experiments in elastic plates:

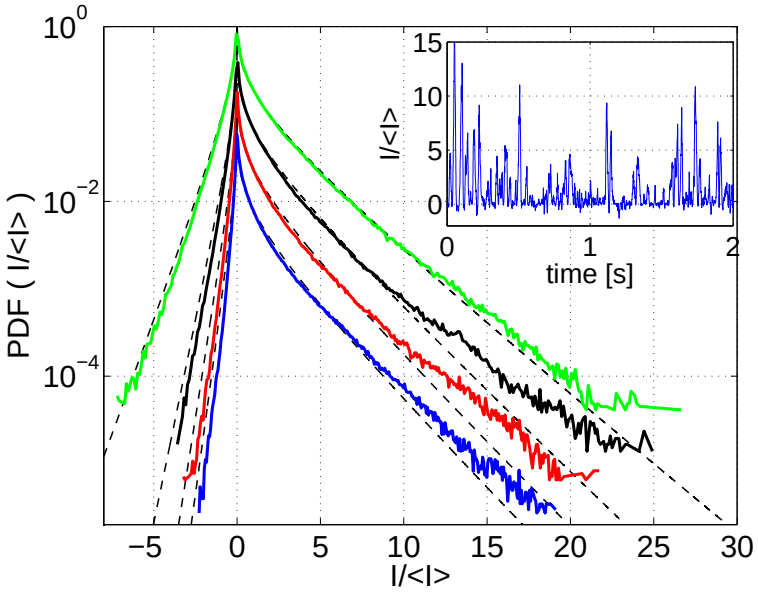

Figure 2.10: PDF of injected power into the bending elastic wave turbulence, from [9] (N. Mordant, Private Com.). Data are normalized by their mean value and the 4 curves have been shifted by a factor 3 for clarity. The forcing is a gaussian low frequency noise of bandwidth $[0, 15]$ Hz. From bottom to top $\langle I \rangle = 0.64$, 0.33, 0.124 and 0.022 W. Dashed line fits correspond to the formula (2.6). Inset: Temporal trace of the injected power over 2 s and $\langle I \rangle = 0.64$ W.

Bending waves on an elastic plate can also display wave turbulence. It has been theoretically predicted[8] and experimentally measured[9] that these waves can interact non-linearly between them to achieve a nonequilibrium steady state in thin elastic plates. Measurements of the injected power to maintain this out-of-equilibrium steady state have been performed, as in the experimental set-up described above. A 2 x 1 m^2 steel plate, 0.4 mm of thickness (Young modulus E= 2.0x10^{11} N/m^2, density ρ=7.85xg/cm^3) is pinched on its top (short) side and hangs under its own weight. The other three sides are free except from the two bottom corners which are loosely held by springs of low stiffness, only to prevent too large excursions of the bottom of the plate. A vibrator type V406/8 from LDS is fixed at a point located 40 cm from the plate bottom and in the middle of the plate in the horizontal direction. This vibrator can move normally to the plate to excite bending waves. The forcing excitation here is a low-frequency gaussian random noise of bandwidth restricted to 15 Hz for example. The forcing necessary to excite the bending waves is recorded by a force probe of type NTC from FGP sensors and an accelerometer 4393V conected to a charge amplifier 2365, both from

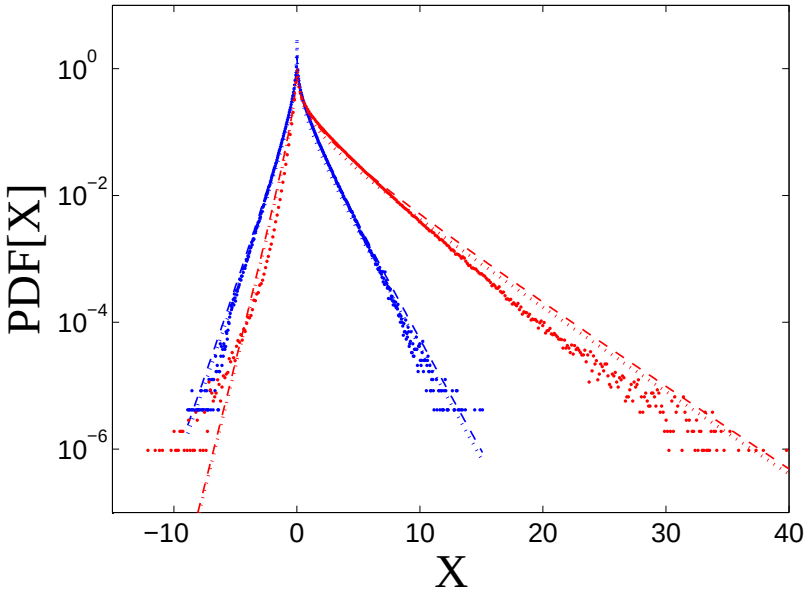

Figure 2.11: PDF of the renormalized power, $X = \frac{I/\sigma_v\sigma_f}{1-(\langle I\rangle/\sigma_v\sigma_f)^2}$, injected by a random forcing into the GOY shell model. The random force is modeled by the OU noise with $\tau_c = \lambda^{-1}$ equal to 1 (blue line) and 20 (red line) whereas other parameters: the rms value of the forcing $\sigma_f = 7.1 \cdot 10^{-2}$, the number of shells $N_s = 20$ and the viscosity $\nu = 4.0 \times 10^{-6}$, are keept constant. The dashed and dot-dashed lines are respectivelly the exact formula (2.6) and the approximated expression (2.7).

B & K. Both the recorded force $F_p(t)$ and velocity $V(t)$ display statistics close to a gaussian and the *rms* fluctuations of $V(t)$ are proportional to the ones of $F_p(t)$.

In a similar way as in [7], the injected power $I(t)$ can be estimated by the product $-F_p(t)V(t)$. Figure 2.10 shows the PDF of the injected power I for two different values of the *rms* value of the force. The typical features appear (a cusp at $I = 0$ and exponential asymmetrical tails). In this case, the larger is the rms value of the force, the larger is the asymmetry between positive and negative events of the PDF. Also we can see a small departure from the exponential tails of the PDF for large events of injected power. AS before, no adjustable parameter is being used for this comparison.

2.4.2 Other systems

The same type of statistics can be found in other complex systems with a larger number of degrees of freedom. It can even be found in systems where the probability distribution functions of the variables use to compute the injected power are **not gaussian** (as in the case of turbulent convection). We describe in the following section some examples of such systems.

The GOY shell model

The shell models in hydrodynamics have been introduced to mimic some aspects of the dynamics of fully developped turbulence in wave number space. A few tens of discrete modes are simulated with suitable short range interactions in order to reproduce the turbulent spectra. We choose here to study energy flux in the GOY shell model which have been optimized to mimic turbulence and turbulent intermittency [10]. The GOY shell model describes the energy cascade through a set of

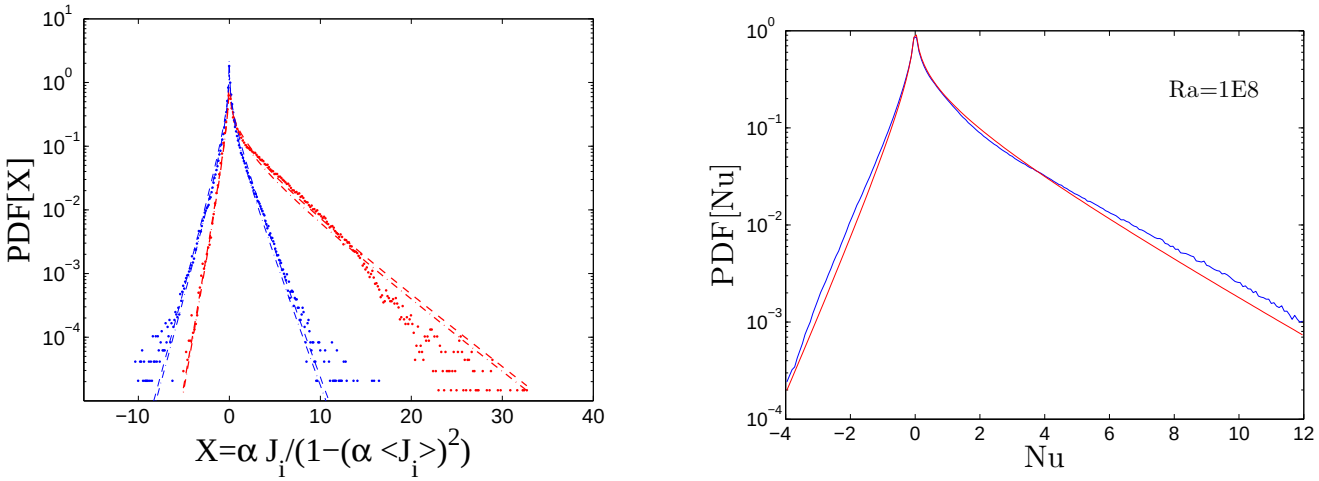

Figure 2.12: **Left**: PDF of the renormalized dimensionless local components of the heat transport, $X = \alpha J_i/(1-(\alpha\langle J_i\rangle)^2)$ with $\alpha = 1/(\sigma_{v_i}\sigma_{\delta T})$, near the side wall of a convective cell in the turbulent regime (Ra=2.6×10^9) extracted from [12]. Blue dots show the horizontal component whereas red dots show the vertical ones. The dashed and dot–dashed lines show respectivelly the relations (2.6) and (2.7). The unknown coefficient α is used as a fitting parameter. **Right**: PDF of the spatial fluctuations of the heat flux at $Ra = 10^8$ (blue) extracted from [14]. Continuous red line corresponds to relation (2.6) where r is used as a fitting parameter

differential equations

$$\frac{du_n}{dt} = ik_n\left(u^*_{n+1}u^*_{n+2} - \frac{\theta}{2}u^*_{n-1}u^*_{n+1} - \frac{1-\theta}{2}u^*_{n-2}u^*_{n-1}\right) + f_n - \nu k_n^2 u_n, \tag{2.18}$$

where u_n is the complex amplitude of the mode n and $(^*)$ stands for complex conjugate, $k_n = 2^{n-4}$ stands for the shell wave number, and f_n is the force applied on the shell n. The dissipation at each shell is given by $\nu k_n^2 u_n$, ν being the kinematic viscosity. In absense of forcing and dissipation this set of equations conserve the energy

$$E = \frac{1}{2}\sum_{i=1}^{N}|u_n^2|,$$

and depending on the value of θ, intermittency occurs in the system. θ is related to the second conserved quantity of the set of equations (which is quadratic in u_n), when no forcing nor dissipation are taken into account.

Instead of the usual constant forcing we use a random one. Such a forcing does not modify the energy cascade of the shell model. The random forcing is once again chosen as an O-U type of noise, in order to be able to keep the characteristic time scale of energy injection larger than dissipative ones. This random force is applied to the 4th shell of the model, and the injected power $I(t)$ is calculated as the real part of $u_4^* f(t)$. At this stage, the PDF of both $f(t)$ and $u_4(t)$ are gaussian. The PDF of the injected power I is shown in Fig.(2.11). For both plots of Figure 2.11, we just change thie correlation time $\tau_c = 1/\lambda$, keeping constant the *rms* value of the forcing, σ_f=7.1 x 10^{-2}, the total number of shells, $N_s = 20$, and the viscosity, ν =4.0 x 10^{-6}. In this simulation, we have used a Runge-Kutta method of order four and the time step was set at 2x10^{-5}. The asymmetry increases with τ_c.

Turbulent Convection

The same type of statistics was also found for the turbulent heat flux in convective transport. The studies on turbulent convection have been focused since a long time only on the relation between the mean temperature difference, $\Delta T = (T_d - T_u)$, and the heat transport, Q, or in dimensionless variables between the Rayleigh number Ra (defined in Chapter 2) and the Nusselt number, $Nu = Qh/(\lambda \Delta T)$. Only recently measurements have been performed on the fluctuations of the heat flux [11, 12, 13, 14].

The heat flux can be estimated as the product ot two random quantities: the velocity component $v_i(\mathbf{r}, t)$, either vertical (parallel to the temperature gradient) or horizontal (perpendicular to the temperature gradient), and the temperature perturbation $\delta T(\mathbf{r}, t)$. These quantities have been estimated locally in mid-height of a Rayleigh-Bénard experiment close to the boundary of the cell [12], or by a Langrangian probe advected by the convecting fluid [13], or in numerical simulation where the spatial fluctuations can be measured [14]. In all these cases, the PDF presents the same shape. We show on the left part of Fig. (2.4.2) the 2 components of the dimensionless local heat flux, $J_i(\mathbf{r}, t) \equiv v_i(\mathbf{r}, t) \times \delta T(\mathbf{r}, t)$, measured by Xia [12] at mid-height of the convection cell close to the lateral walls where a convective large scale wind provides most of the heat flux. In contrast to its horizontal counterpart, the average of the vertical component of this flux, $\langle J_z(\mathbf{r}, t) \rangle$, is not expected to vanish since there is an average heat flux from the bottom to top of the cell. The heat transport in the horizontal direction (x–axis) is more than ten times smaller, $\langle J_x(\mathbf{r}, t) \rangle / \langle J_z(\mathbf{r}, t) \rangle = 0.06$, therefore the PDF is almost symmetrical. This can be simply understood from the fact that the vertical velocity $v_z(\mathbf{r}, t)$ is pumped by the temperature difference $\delta T(\mathbf{r}, t)$, therefore spatio-temporal correlations between both variables must be large, as we can see from Fig. 2.4.2. On the right part of this figure, we present the instantaneous spatial fluctuations of the vertical heat flux estimated by numerical simulation in a large aspect ratio cell for a large value of the Rayleigh number Ra[14]. It is astonishing that, although in several studies the temperature fluctuations have been found to display large events that do not follow gaussian statistics, the PDF of the normalised local heat flux $J_i(\mathbf{r}, t) / \langle J_i(\mathbf{r}, t) \rangle$ displays exponential tails following the simple expressions (2.6) or (2.7), where the sole parameter is its mean value related directly to the correlation between velocity and temperature fluctuations.

2.5 Conclusions

In this Chapter, we have studied the probability distribution function of the injected power in out-of-equilibrium systems when the forcing acting on the system is a random gaussian noise. The probability distribution function (PDF) of $I(t)$ displays a cusp near $I \simeq 0$ and asymmetric exponential tails. This typical PDF shape has been observed in more complex dissipative systems (such as in granular gases, wave turbulence and convection). We have studied experimentally in a simple electronic system the dependence of $I(t)$ with respect to the damping rate rate. The relevant parameters of the system can be easily changed in our simple experiment. Using a simple model (two coupled linear Langevin equations) we can deduced the shape of the distribution of fluctuations of I. The sole control parameter in this approach is the correlation correlation coefficient r related directly to the mean dissipation, driving the asymmetry of the distribution of $I(t)$: the larger the mean dissipation, the larger is the asymmetry of the PDF.

Bibliography

[1] A.N. Kolmogorov, Dokl. Akad. Nauk SSSR **30**, 299303 (1941) [English: Sov. Phys. Dokl.]

[2] K. Huang, *Statistical Mechanics* (Wiley & Sons, New York, 1987)

[3] J. Farago, *J. Stat. Phys.* pp 781 (2002)

[4] P. Langevin, C. R. Acad. Sci. (Paris) **146**, 530 (1908); for an english translation, see D. S. Lemons, and A. Gythiel, Am. J. Phys. **65**, 1079 (1997)

[5] R. Kubo, M. Toba, N. Hashitsume, *Statistical Physics II: Nonequilibrium Statistical Mechanics*, (Springer Series in Solid–State Sciences, Springer, Berlin 1985).

[6] H. Risken, *The Fokker-Planck Equation–Method of Solution and applications* (2d Ed, Springer, Berlin, 1996); W. Feller *An introduction to Probability Theory and Its Applications* Vol. II (2d Ed, J. Wiley & sons, NY, 1971) .

[7] E. Falcon, C. Laroche, and S. Fauve, Phys. Rev. Lett. **98**, 094503 (2007); E. Falcon, S. Aumaître, C. Falcón, C. Laroche, and S. Fauve, Phys. Rev. Lett. **100**, 064503 (2008)

[8] G. Düring, C. Josserand, and S. Rica, Phys. Rev. Lett. **97**, 025503 (2006)

[9] N. Mordant, Phys. Rev. Lett. **100**, 234505 (2008); A. Boudaoud, O. Cadot, B Odille, and C. Touzé, Phys. Rev. Lett. **100**, 234504 (2008)

[10] E.B. Geldzer, Sov. Phys. Dokl. **18** (1973); M. Yamada, K. Ohkitani, J. Phys. Soc. Jpn **56** pp 4210 (1987); L. Biferale Annu. Rev. Fluid Mech. **35** (2003) pp 441-468

[11] S. Aumaître, S. Fauve, Europhys. Lett. **62**–6 (2003) 822–828

[12] X.-D. Shang, X.-L. Qiu, P. Tong, K.-Q. Xia, Phys. Rev. Lett. **90** 074501(2003)

[13] W.L. Shew, Y. Gasteuil, M. Gibert, P. Metz and J.F. Pinton arXiv:physics/0703245

[14] O. Shiskina and C. Wagner, Phys. Fluids **90** n^o 085107 (2007)

Chapter 3

Injected power fluctuations and the Fluctuation Theorem in dissipative systems

This Chapter is devoted to probe the validity of the Fluctuation Theorem (FT) in an experimental, and therefore dissipative, system driven out-of-equilibrium in a stationary state. The Fluctuation Theorem describes the asymmetry of distribution of a fluctuating global quantity such as the injected power I, averaged over a time τ much larger than its typical correlation time τ_c. In that sense, the FT relates directly the injected power fluctuations and the internal energy fluctuations when a dissipative system is set in an out-of-equilibrium stationary state. The experimental device used to test the FT is the simple electronic RC circuit described in Chapter 2.

The Chapter is divided as follows: in the first part (Section 3.1) we recall what the FT states and the hypothesis that it necessitates for its application to a dissipative system. In the second part (Section 3.2), we experimentally test the FT in an electronic RC circuit forced by a quasi-gaussian random noise. We find out that in this simple system it does not hold. We test the FT also in wave turbulence experiments performed in fluids and elastic sheets as shown in Section 3.3.

3.1 Fluctuation Theorems and their application to dissipative out-of-equilibrium systems

A dissipative system set in a statistically stationary out-of-equilibrium state necessitates a constant influx of energy. This point has been discussed *in-extenso* in Chapters 1 and 2, where the statistical properties and the distribution function of the injected power fluctuations have been studied in simple examples (for instance when the dissipated power P_{diss} is constant or proportional to the internal energy E) and related to the internal energy fluctuations of the system under study. A pertinent question is if there is a suitable way to describe these fluctuations and how the relationships that we have found can be extended to dissipative systems forced strongly out of equilibrium in a statistically steady state, where there is no external control on the injected and dissipated power fluctuations. We know that in equilibrium statistical mechanics, the distribution function $P(O)$ of an observable O in thermodynamic equilibrium, is a gaussian centered around its mean value $\langle O \rangle$,

$$P(O) \sim \exp\left[\frac{O - \langle O \rangle}{\sigma_O^2}\right], \tag{3.1}$$

with σ_O the standard deviation of O, which, as the number of degrees of freedom of the system N grows, goes to zero $\sim N^{-1/2}$. This is a consequence of the central limit theorem: the sum of a

large number of independent random variables, each one of them having a finite mean and standard deviation, will be approximately normally distributed. In an isolated system (or a system in contact of with a thermal bath at temperature T) consisting of a large number of non interacting particles, the energy of the system at any instant of time $E(t)$ can be written as the sum of the kinetic energy of each particle which fluctuates due to thermal agitation. For a large number of particles, the distribution function of the energy will follow Eq. (3.1). When a system is set in an out-of-equilibrium state, this is usually not the case for the distribution functions of its global observables.

In this context, theoretical approaches to the problem of distribution functions in out-of-equilibrium systems have been given in recent years. Universal distributions, such as Gumbell, χ-squared[1] or other distributions [2] have been proposed to describe quantities in systems forced strongly out-of-equilibirum or into turbulent-like states. Although they seem to fit accurately certain sets of experimental or numerical data, there is no generalization of these distributions to a larger class of dissipative systems. In that sense, instead of searching for "universal" distribution functions, the attention has been focused on fluctuation relations.

Fluctuation relations have received much attention, since the early work of Nyquist and Johnson [3] and of Callen and Welton [4] on the fluctuation-dissipation theorem, which relates the out-of-equilibrium behavior of a system from its reversible fluctuations in thermodynamic equilibrium. Although the relationship between equilibrium fluctuations with irreversible behavior was already found by Einstein in his theory of brownian motion [5], it was not given rigorous mathematical proof until the works of Onsager [6] and Kubo [7]. Later, they where expanded to the nonlinear regimes [8], or as conections between equilibrium states through out-of-equilibirum processes [9], but always in the context of equilibrium distributions or small perturbations of them.

Far from equilibrium, there has been theoretical advances in fluctuation relations. These relations describe mainly the asymmetry of the distribution function of the global observable O averaged in the long time limit $\tau \to \infty$, which is much larger than the autocorrelation time τ_c of O. The smoothing or running average of O, O_τ, defined as

$$O_\tau(t) = \frac{1}{\tau}\int_t^{t+\tau} O(t')dt', \tag{3.2}$$

is used to compute the asymmetry function [10]

$$\rho(\epsilon) \equiv \lim_{\tau\to\infty} \frac{\tau_c}{\tau} \log\left[\frac{P(\epsilon)}{P(-\epsilon)}\right], \tag{3.3}$$

where $\epsilon = O_\tau/\langle O\rangle$ is the normalized observable which follows a distribution $P(\epsilon)$. This function is thus an indicator of the asymmetry of the distribution function of the averaged normalised observable ϵ. By computing the running average O_τ, we smear out the large fluctuations or transient dynamics of the system. It is clear that by averaging in an interval of length τ, the fluctuations of O_τ will decrease strongly. In the assymptotic limit $\tau \to \infty$, one would expect ϵ to converge to 1, and its fluctuations to be distributed as a gaussian

$$P(\epsilon) \simeq \exp[\tau(\epsilon-1)^2/2\sigma_\epsilon^2], \tag{3.4}$$

where

$$\sigma_\epsilon \equiv \lim_{\tau\to\infty}\int_{-\tau}^{\tau} \frac{\langle O(t')O(0)\rangle - \langle O\rangle^2}{\langle O\rangle^2}dt'$$

is the temporal integral of the autocorrelation function of O, and by the Wiener-Khinchine theorem, the zero-frequency component of its power spectrum density $|\widehat{O}(\omega)|^2$.

The asymmetry function $\rho(\epsilon)$ is the starting point to study the Fluctuation Theorem (FT). The FT (also called the Gallavotti–Cohen relation) [11, 12, 13] was first introduced in a numerical simulation where a newtonian fluid was subjected to an external shear[8]. Later, a mathematical proof was given [14]. It states that,

$$\rho(\epsilon) = \beta\epsilon, \tag{3.5}$$

which means that in the long time limit $\rho(\epsilon)$ loses the temporal dependence on τ and only depends on ϵ linearly. The constant β, independent of the averaging time τ and value of the normalized observable ϵ, is related to the internal energy fluctuations and therefore related directly to the "temperature" of the system. Therefore the FT can relate the computed probability density function $P(\epsilon)$ of the measured observable ϵ to the internal fluctuations of the system, accessing information that otherwise could not be accessed. To do so, large negative and possitive fluctuations of ϵ must occur.

It is important to recall the hypothesis under which the FT is valid. First, for the application of the FT the internal dynamics of the system under study must be microscopically reversible in time. This point means that inverting the temporal evolution of the system leaves the equations of motion of the inner degrees of freedom unchanged. The second hypothesis is that the system must be dissipative, contracting the phase space. Lastly, the dynamics on the phase space should be chaotic. This is an analogy to ergodicity in equilibrium statistical mechanics, where the available phase space is completely occupied and invariant measures can be defined and used to extract and compute averages of observables [11, 12, 13]. The type of systems where these hypothesis are satisfied are very special: they can interchange dissipation with injection just by changing $t \to -t$. Experimentally, a system that fulfills these restrictions are very hard (not to say impossible) to find.

The relation of Eq.(3.5) has been tested experimentally in granular gases [15], turbulent flows [16], liquid crystals [17], electric dipoles [18], mechanical oscillators [19] and colloidal particles [20] and also numerically in granuar gases [21] and turbulent flows [22]. In all the different studies, for long averaging times, the linear relation between ϵ and $\rho(\epsilon)$ has been observed, but for a small range of ϵ. We will study experimentally the fulfillment of Eq.(3.5) in a simple system where large values of ϵ can be reached ($\epsilon \simeq 3$), in the next section.

The PDF of $P(\epsilon)$ for large averaging τ can be defined also by means of the Large Deviation Function (LDF) $f(\epsilon)$. It is generally defined as

$$f(\epsilon) \equiv \lim_{\tau\to\infty} \frac{\tau_c}{\tau} \log\left[P\left(\epsilon \equiv O_\tau/\langle O\rangle\right)\right], \tag{3.6}$$

and it describes how the fluctuations of ϵ with respect to $\langle\epsilon\rangle$=1 behave as the averaging time τ/τ_c in the smoothing average becomes larger and larger. Developing Eq. (3.3) using the definition of the LDF leads to

$$\rho(\epsilon) = f(\epsilon) - f(-\epsilon). \tag{3.7}$$

Developing Eq. (3.7) up to first order in ϵ, thus taking into account only the terms close to $\epsilon \simeq 0$, leads to

$$\rho(\epsilon) \simeq 2f'(0)\epsilon,$$

which easily satisfies the Gallavotti-Cohen relation of Eq. (3.5). It is just needed that the LDF has a linear part $f(\epsilon) = \alpha\epsilon + g(\epsilon)$, where $g(\epsilon)$ is a nonlinear function of the normalized variable ϵ. For instance, if the PDF of ϵ is similar to Eq. (3.4), the LDF is $f(\epsilon) = (\epsilon - 1)^2/2\sigma_\epsilon^2$ and the relation of

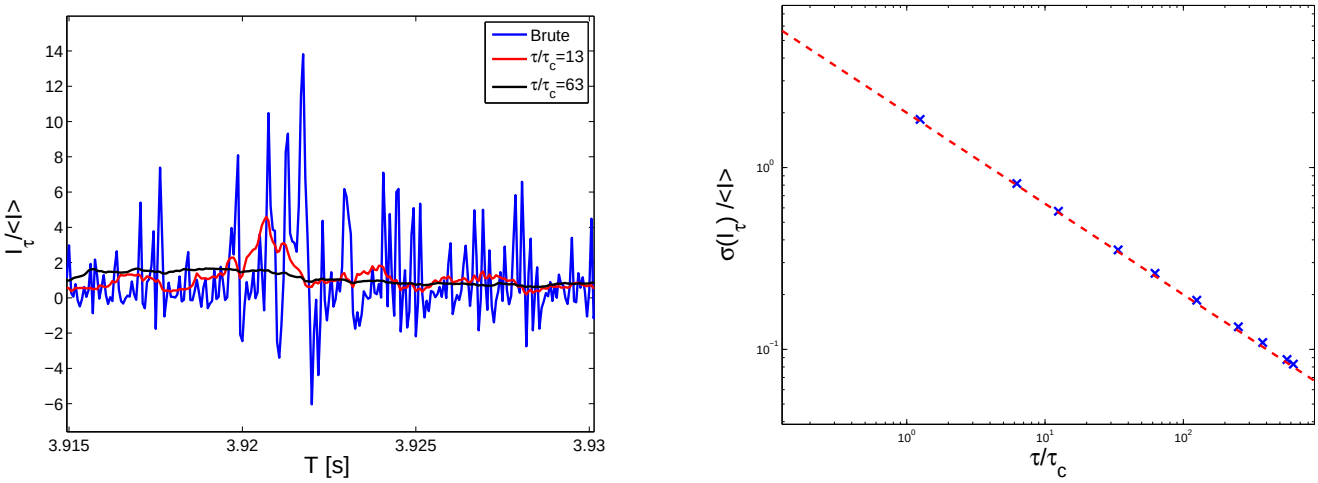

Figure 3.1: **Left:** Typical temporal traces of $\epsilon = I_\tau / < I >$ for the τ/τ_c=0 (blue), 13 (red) and 63 (black) for $\gamma = 1/RC = 500$ Hz. **Right:** Standard deviation $\sigma_{I_\tau}/\langle I \rangle$ as a function of the average normalised time τ/τ_c for $\gamma = 1/RC = 500$ Hz. Best fit is $\sigma_{I_\tau}/\langle I \rangle \sim (\tau/\tau_c)^{-0.51}$.

Eq. (3.7) gives $\rho = 2\epsilon/\sigma_\epsilon^2$, satisfying the FT with $\beta = 2\sigma_\epsilon^{-2}$. The linear aproximation of the LDF as an explanation of the linearity found in experiences and numerics was first conjectured by Aumaître in his PhD thesis [21] and then predicted in a Langevin equation in a dissipative regime by Farago [10].

3.2 Experimental test of the Fluctuation Theorem in an electronic RC circuit

We will test experimentally whether the FT is satisfied in a simple dissipative system maintained in an out-of-equilibrium steady state. For this matter, we will continue to use the electronic RC circuit of Chapter 2. As it was explained before, this simple circuit can be viewed as a mimic of a brownian particle strongly forced out -of-equilibrium. The forcing is still a random Gaussian noise with zero mean and a characteristic correlation time $1/\lambda$ where λ is the frequency cut-off of its power spectrum density.

The smoothing average of the injected power I_τ is computed from the previous data of I as

$$I_\tau(t) = \frac{1}{\tau}\int_t^{t+\tau} I(t')dt', \tag{3.8}$$

where τ stands for the time of average of the signal, which is several times the correlation time τ_c of the injected power I. For our experimental set-up, the correlation time τ_c is the inverse of the cut-off frequency, $1/\lambda$, which is now fixed to 10^{-4} s. We show a typical temporal trace of $\epsilon = I_\tau/\langle I \rangle$ in Fig.(3.1), as we increase the averaging time. We can see how, by increasing the averaging time τ, the fluctuations around the mean, $\langle \epsilon \rangle$ =1, decrease their value. The *rms* fluctuations decrease with τ/τ_c as a power law $\sim (\tau/\tau_c)^{-1/2}$, just as in the case of the central limit theorem. With this data, one can compute $\rho(\epsilon)$.

First, it should be noted that our simple system is not time reversible, therefore the hypothesis used to derive the FT are not fulfilled in this system. However, we will try to test the relation Eq.(3.5) with our experimental data.

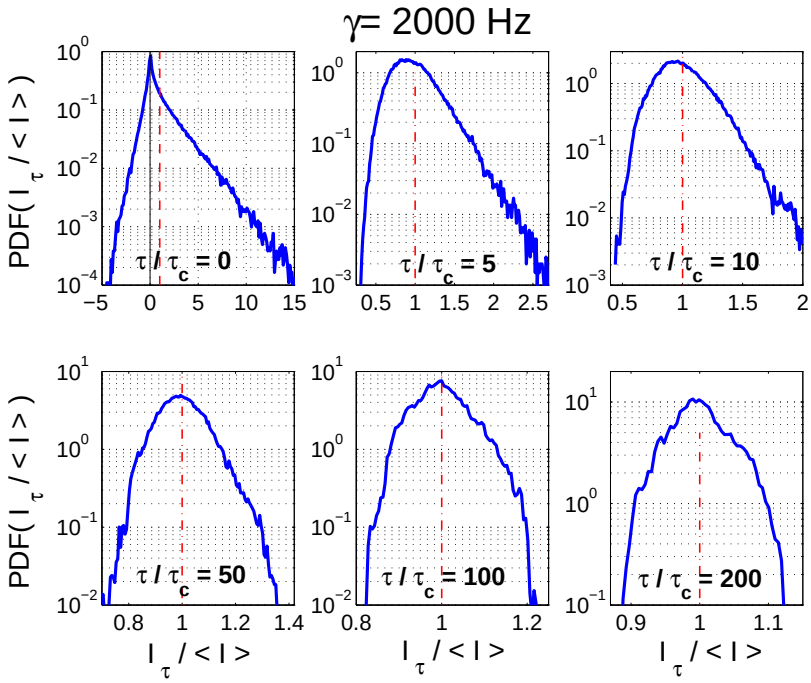

Figure 3.2: PDF of $I_\tau/\langle I\rangle$ for various values of $\tau/\tau_c = 0$, 5, 10, 50, 100 and 200 at a fixed value of $\gamma = 2000$ Hz. The straight line $(-)$ correspond to $I_\tau/\langle I\rangle = 0$ and the dashed line $(--)$ to $I_\tau = \langle I\rangle$.

Fig. (3.2) displays the PDF of time-averaged injected power $I_\tau/\langle I\rangle$ when τ/τ_c is increased. Several features appear. First, the negative injected power events decrease with increasing τ until they disappear for $\tau \gtrsim 5\tau_c$. Second, when τ/τ_c is increased, the PDF shape for negative values of $I_\tau/\langle I\rangle$ changes from an exponential shape to a Gaussian one, whereas the exponential shape of the positive part is quite robust. Only when $\tau \gg \tau_c$, the PDF shape close to the maximum tends towards a gaussian, as one would expect from the central limit theorem. In Fig.(3.2), when τ/τ_c increases, the PDF most probable value ϵ^* (i.e., where the PDF amplitude is maximum) increases slowly from $I_\tau/\langle I\rangle = 0$ to 1 (the mean value of the injected power). This dependence of ϵ^* is shown in Fig. (3.4) as a function of τ/τ_c. We will see below that this dependence is very important with respect to the possible fulfillment of the FT.

The question that needs to be addressed is what happens when ϵ is far from zero. The experimental values of the asymmetrical function $\rho(\epsilon)$ are shown in Figs. (3.5) and (3.6) for two different values of $\gamma = 1/RC$, as a function of ϵ with $0 \leq \epsilon < 3$. The accessible values of ϵ are large with respect to the later experimental studies. For small ϵ, $\rho(\epsilon)$ increases linearly as expected, then $\rho(\epsilon)$ saturates when ϵ is increased further. For each value of τ/τ_c, the beginning of the saturation occurs for a critical ϵ value, smaller than the average $\langle\epsilon\rangle$=1. The saturation value of the curve corresponds the most probable value of the PDF of ϵ as we can see Fig. (3.4)). For values of $\epsilon < \epsilon^*$, the linear fit of Eq. (3.5) is satisfied, but for values $\epsilon > \epsilon^*$, the asymmetric function departs from Eq. (3.5), as it is shown in Fig. (3.4). After that point there is a change of behavior of the PDF: for values of ϵ larger than the most probable value ϵ^* the PDF behaves exponentially, contrary to the smoother behavior of the PDF ϵ smaller than ϵ^* (see Figs. (3.2) and (3.3)). Moreover, increasing γ at a fixed value of τ/τ_c leads to decreasing available values of ϵ necessary to probe the FT, as it is displayed in Figs. (3.2) and (3.3). With these PDFs we compute the asymmetry function $\rho(\epsilon)$, as displayed in Figs.(3.5) and (3.6)). It comes from the fact that when γ is increased, the number of negative injected power events, $\epsilon < 0$, decreases (γ controls the skewness of the PDF at a given $\tau_c \sim 1/\lambda$).

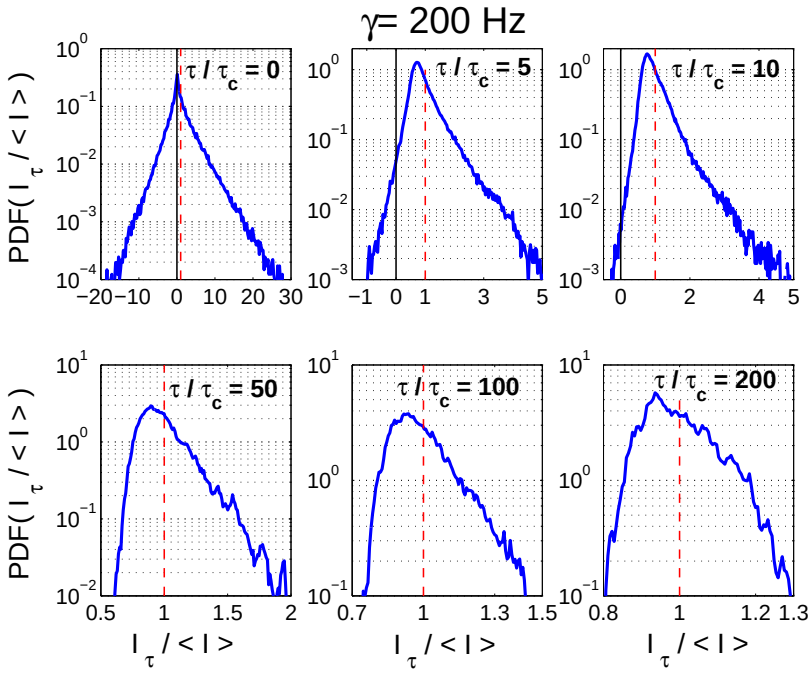

Figure 3.3: PDF of $I_\tau/\langle I\rangle$ for various values of $\tau/\tau_c = 0$, 5, 10, 50, 100 and 200 at a fixed value of $\gamma = 200$ Hz. The straight line $(-)$ corresponds to $I_\tau/\langle I\rangle = 0$ and the dashed line $(--)$ to $I_\tau = \langle I\rangle$.

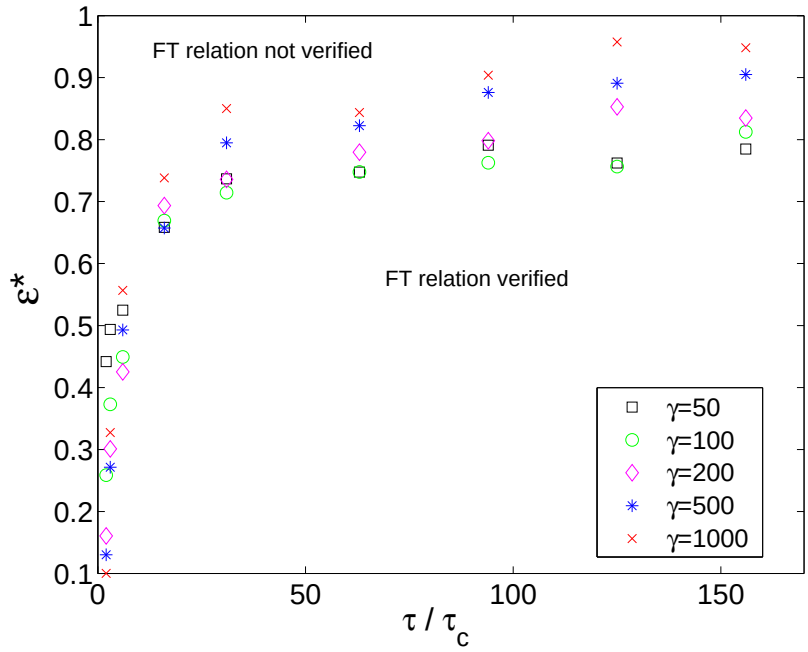

Figure 3.4: Most probable value ϵ^* of PDF$(I_\tau/\langle I\rangle)$ as a function of τ/τ_c for $\gamma = 50$, 100, 200, 500 and 1000 Hz. For $\epsilon < \epsilon^*$, the FT relation is verified, whereas it does not hold for $\epsilon > \epsilon^*$ (see text).

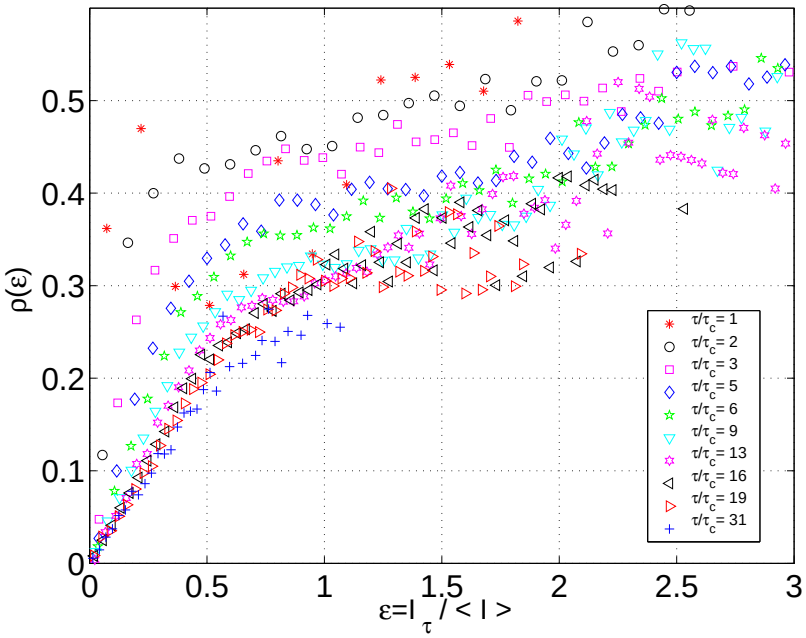

Figure 3.5: Asymmetrical function $\rho(\epsilon) = \frac{\tau_c}{\tau} \ln\left[\frac{P(\epsilon)}{P(-\epsilon)}\right]$ as a function of ϵ for different integration times $\tau/\tau_c = 1$ ($\star$) to 31 (+) at fixed $\gamma = 100$ Hz and $D = 1.56$ mV$^2_{\rm rms}$/Hz.

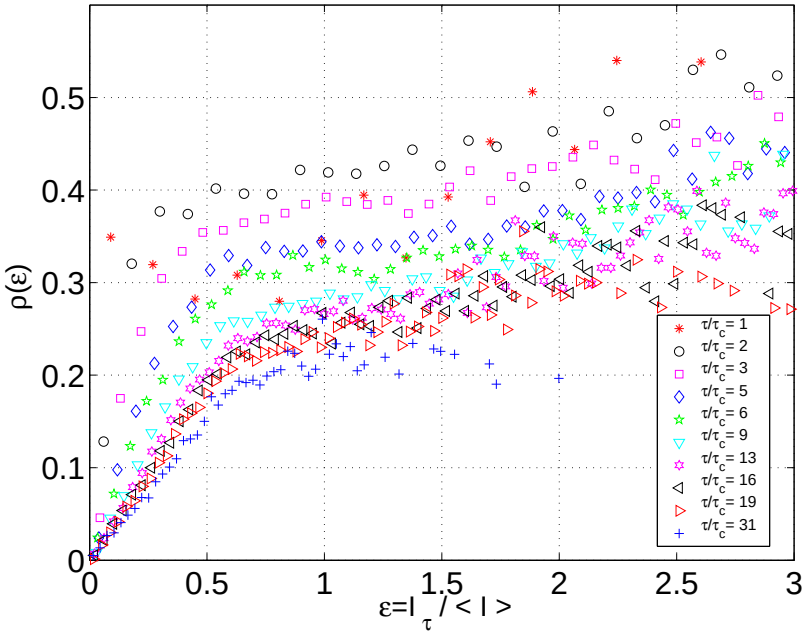

Figure 3.6: Asymmetrical function $\rho(\epsilon) = \frac{\tau_c}{\tau} \ln\left[\frac{P(\epsilon)}{P(-\epsilon)}\right]$ as a function of ϵ for different integration times $\tau/\tau_c = 1$ ($\star$) to 31 (+) at fixed $\gamma = 50$ Hz and $D = 1.56$ mV$^2_{\rm rms}$/Hz.

We stress the fact that the damping rate γ, and therefore the mean dissipation, is not chosen in this simple experiment in an *ad-hoc* manner to satisfy time-reversibility. The smoothing of the signal around $\langle I \rangle$ also decreased the number of available negative events.

In most of the previous experimental and numerical tests of the Fluctuation Theorem (as the

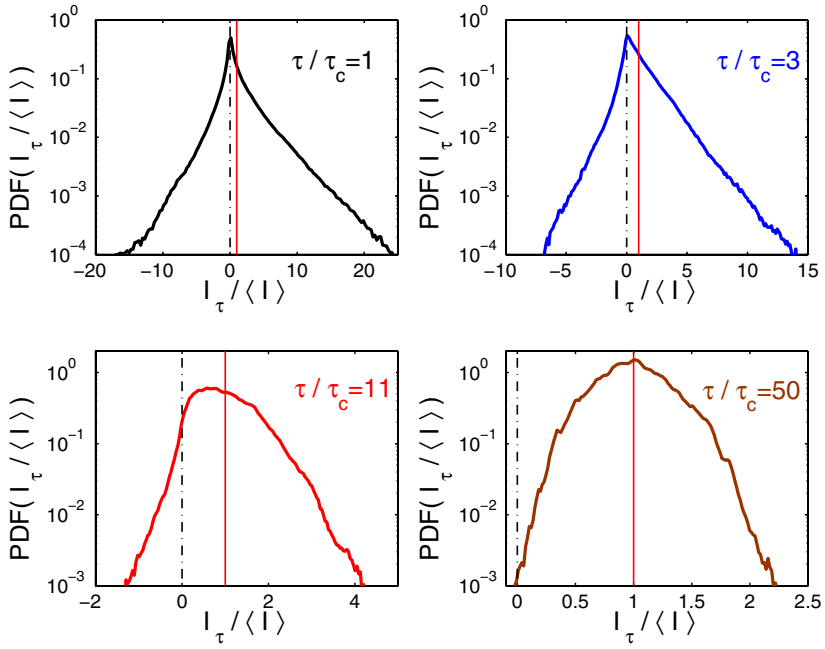

Figure 3.7: Probability density function $P(\epsilon = I_\tau / < I >)$ for τ/τ_c =1, 3, 11 and 50. Solid line indicate the mean value $\epsilon = 1$. This PDF corresponds to the injected power when the working fluid is water with depth of $h = 23$ mm. (Taken from [23]).

ones in the references above), the linear relationship between ϵ and ρ stated in Eq. (3.5) has ben observed. As explained above using Eq. (3.7), this is due to the small range of explored $\epsilon \leq 0.8$ at high $\tau/\tau_c \leq 20$. In our experiment, large range of ϵ (up to 3) is also available even for high $\tau/\tau_c \simeq 20$. This allows us to test in a deeper way the FT. As explained above, the FT works only for ϵ values smaller than the most probable value as it is shown in Fig. (3.4). Above this value, a saturation occurs, due to the different behaviors of the PDF. Large events of injected power are not described by the FT, and lead to the observed saturation of $\rho(\epsilon)$. To further investigate this point we test the FT in other systems with a larger number of degrees of freedom and more complex internal dynamics. A larger range of ϵ has been reached experimentally in a different experimental device in wave turbulence experiments. With this larger available range, the FT was tested, founding, again, that it was not satisfied. We show these results in the following section.

3.3 Experimental test of the Fluctuation Theorem: Wave Turbulence experiments

We have also studied the validty of the FT in more complex systems, with a large number of degrees of freedom. As we have already explained in the previous section, the probability distribution function of the injected power $I(t)$ necessary to excite the turbulent-like regime of surface wave turbulence (in fluids) and bending wave turbulence (in elastic sheets) displays exponential tails and a cusp close to $I \simeq 0$. With the recorded fluctuations of $I(t)$, we computed the normalised smoothing averages $\epsilon = I_\tau / \langle I \rangle$ and their probability density functions $P(\epsilon)$ for different averaging times. We show the main results with respect to the fulfillment of the FT for these experiments.

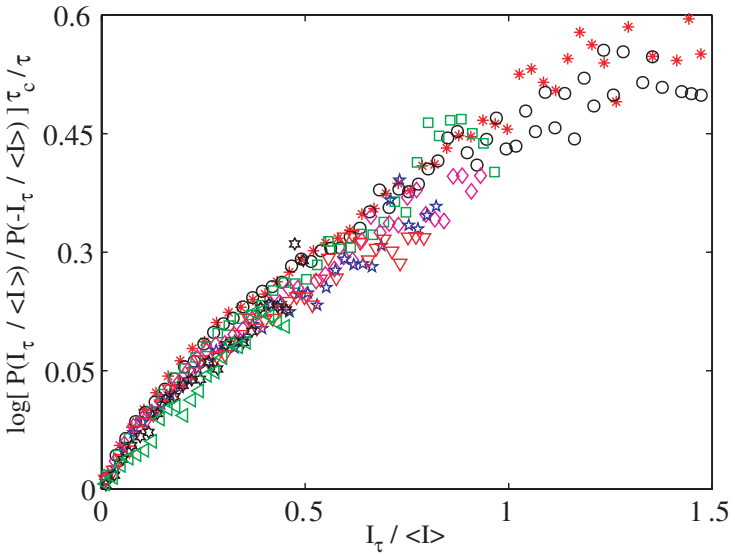

Figure 3.8: Plot of $\rho(\epsilon)/\tau_c = \frac{1}{\tau}\log\left[\frac{P(\epsilon)}{P(-\epsilon)}\right]$ for $16<\tau/\tau_c<39$. (Taken from [23]).

3.3.1 Wave Turbulence experiments in fluids

Following [23], we present the probability density function of ϵ for 4 different values of τ/τ_c =1, 3, 11 and 50, shown in Fig.(3.7). The correlation time of the injected power is τ_c =0.03 s, calculated from the autocorrelation function of $I(t)$. As τ/τ_c grows, the PDF of the normalized running average becomes smoothly peaked around $\epsilon = 1$, as it converges to the LDF of the averaged normalized variable. The convergence to the asymptotic shape of the LDF is slower than in the case of the electronic circuit, taking averaging times of the order of $\tau \simeq 50\tau_c$ to converge closely to the LDF. As in the case of the RC circuit, the amount of negative events becomes negligible as τ/τ_c grows. With the PDFs computed for different averaging times, we calculate the asymmetrical function $\rho(\epsilon)$, displayed in Fig.(3.8). We found that the FT is not fulfilled, i.e it does not follow Eq. (3.5), when large values of ϵ are achieved. For a given value of τ/τ_c, as ϵ grows, the function $\rho(\epsilon)$ smoothens and the linear behavior is not fulfilled. Increasing the averaging time shortens the available ϵ range, which will not surpass the average value $\langle\epsilon\rangle$=1. In this small range, as explained in Section 3.1, the linear behavior of $\rho(\epsilon)$ in ϵ is recovered, as a consequence of the expansion of the LDF of ϵ close to $\epsilon \sim 0$.

3.3.2 Wave Turbulence experiments in elastic plates:

In bending wave turbulence over elastic sheets, the injection of energy is needed to excite the turbulent-like regime. Using the temporal traces of the injected power $I(t)$ taken from the experiment by Mordant [24], we have also studied the statistics of the injected power I_τ averaged over a time interval τ. The correlation time of the injected power in the experimental set-up described in [24] is $\tau_c = 0.06$ s. This correlation time is of the same order of magnitude as the frequency cut-off of applied force on the elastic sheet f_{drive} calculated from the autocorrelation function of $I(t)$. We show, in Fig.(3.9), the computed asymmetrical function $\rho(\epsilon)$. We found that the FT is not fulfilled when large values of ϵ are achieved, as in the previous example of suface wave turbulence. Increasing the values of ϵ, the asymmetrical function departs from linearity instead of being linear in ϵ as for small values with respect to the mean $\langle\epsilon\rangle$=1. We show also the value of $\rho(\epsilon)$ for the instantaneous

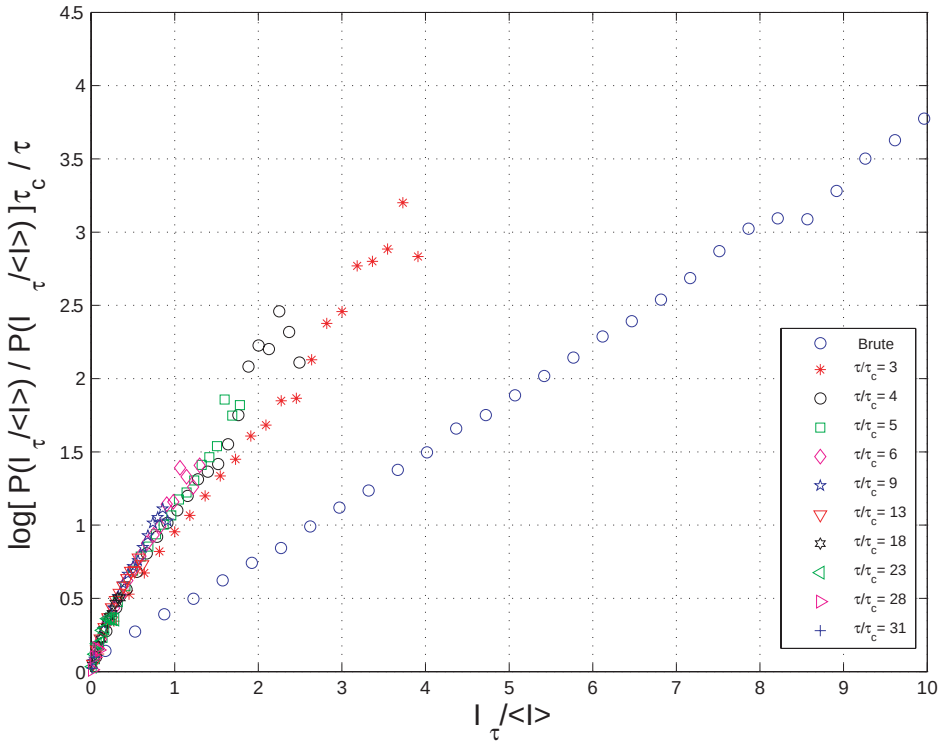

Figure 3.9: Plot of $\rho(\epsilon)/\tau_c = \frac{1}{\tau}\log\left[\frac{P(\epsilon)}{P(-\epsilon)}\right]$ for $0<\tau/\tau_c<31$.

fluctuations of the injected power. Due to the exponential behavior of the PDF, the linearity holds.

Comment on the Fluctuation Theorem and Instantaneous Fluctuations: In Fig.(3.9), we have shown the behavior of $\rho(\epsilon)$ as a function of the averaging time τ/τ_c. For all values of $\tau/\tau_c>0$, the asymmetrical function does not follow the relation of Eq.(3.5). But for the instantaneous fluctuations of $I(t)$, a fluctuation relation is satisfied. Taking into account the probability distribution function of the injected power described in the previous chapter

$$P(I) \simeq \exp[rI/\sigma_v\sigma_f(1-r^2)] \times K_0(|I|/\sigma_v\sigma_f(1-r^2)),$$

we can calculate the "instantanteous" asymmetrical function $\rho_{inst}(I)$ as

$$\rho_{inst}(I) = \log[\frac{P(I)}{P(-I)}] = \frac{2r}{\sigma_v\sigma_f(1-r^2)}I, \tag{3.9}$$

where $\frac{2r}{\sigma_v\sigma_f(1-r^2)}$ is constant. If we use the definitions of $\sigma_f^2 = D/2\lambda$, $\sigma_v^2 = D/2\lambda\gamma(\lambda+\gamma) = \sigma_f^2/\gamma(\lambda+\gamma)$ and $r = \sqrt{\gamma/(\gamma+\lambda)}$ the expression of Eq.(3.9) can be written as

$$\rho_{inst}(I) = \frac{2}{\sigma_v^2\lambda}I,$$

where λ is the inverse of the correlation time of the injection and $\sigma_v^2/2 = E$ is the internal energy of system. In that sense, we can estimate the energy of the system, by computing the slope $\frac{d\rho_{inst}(I)}{dI}$ and the correlation time of the injected power.

3.4 Conclusions

In this Chapter we have experimentally studied the possible application of the Fluctuation Theorem (FT) on a simple dissipative system: an electronic RC circuit excited by an stochastic voltage. The FT has been probed by measuring the asymmetrical function $\rho(\epsilon)$ with $\epsilon = I_\tau/\langle I\rangle$, and I_τ the smoothing average on a time lag τ, much larger than the correlation time of the injected power. In this simple experiment, large fluctuations of ϵ have been observed ($\epsilon \simeq 3$) even for long averaging time ($\tau/\tau_c \simeq 20$). We have found out that the FT is only satisfied for small values of ϵ with respect to the most probable value of the its distribution function. For larger values, the asymetrical function is no longer linear with ϵ but saturates. Thus, the FT does not hold for the large values of ϵ even at large τ/τ_c. This disagreement is not a particular feature of this electronic system, but seems to be generic in several other systems, such as two different wave turbulence experiments, as soon as large fluctuations of ϵ are experimentally achieved.

Bibliography

[1] A. Papoulis, *Probability, Random Variables, and Stochastic Processes* (2nd ed. New York, McGraw-Hill), pp. 104,148, (1984)

[2] S.T. Bramwell, P.C.W. Holdsworth, J.-F. Pinton Nature, **396**, 552-554, (1998)

[3] J. Johnson, Phys. Rev. **32**, 97 (1928); H. Nyquist, Physical Review **32**, 110113

[4] H. B. Callen and T. A. Welton, Phys. Rev. **83**, 34 (1951)

[5] A. Einstein, Annalen der Physik **17**, 549-560

[6] L. Onsager, Phys. Rev. **37**, 405 - 426 (1931)

[7] R. Kubo, M. Toba, N. Hashitsume, *Statistical Physics II: Nonequilibrium Statistical Mechanics*, (Springer Series in Solid–State Sciences, Springer, Berlin 1985).

[8] D. J. Evans and G. P. Morriss, Phys. Rev. A, **30**, pp. 1528-1530 (1984), D. J. Evans and G. P. Morriss, Mol. Phys, **54**, 629(1985)

[9] C. Jarzynski, Phys. Rev. Lett. **78**, 2690 (1997) G. E. Crooks, J. Stat. Phys. **90**, 1481 (1998)

[10] J. Farago, J. Stat. Phys. **107**, 781 (2002)

[11] D. J. Evans, E. G. D. Cohen and G. P. Morriss, Phys. Rev. Lett. **71**, 2401 (1993)

[12] D. J. Evans and D. J. Searles, Phys. Rev. E **50**,1645 (1994);

[13] D. J. Searles and D. J. Evans, J. Chem. Phys **112**, 9727 (2000)

[14] G. Gallavotti and E. G. D. Cohen, Phys. Rev. Lett. **74**, 2694 (1995); D. J. Evans and D. J. Searles, Adv. Phys. **51**, 1529 (2002)

[15] K. Feitosa and N. Menon, Phys. Rev. Lett. **92**, 164301 (2004)

[16] S. Ciliberto and C. Laroche, J. Phys. IV (France) **8**, 215 (1998); X.-D. Shang, P. Tong and K.-Q. Xia, Phys. Rev. E **72**, 015301(R) (2005); S. Ciliberto et al., Physica A **340**, 240 (2004).

[17] W. I. Goldburg, Y. Y. Goldschmidt and H. Kellay, Phys. Rev. Lett. **87**, 245502 (2001)

[18] N. Garnier and S. Ciliberto, Phys. Rev. E **71**, 060101(R) (2005)

[19] F. Douarche, PhD thesis, Ecole Normale Supérieure de Lyon, November 2005; F. Douarche et al., Phys. Rev. Lett. **97**, 140603 (2006)

[20] G. M. Wang et al. Phys. Rev. Lett. **89**, 050601 (2002); D. M. Carberry et al., Phys. Rev. Lett. **92**, 140601 (2004); V. Blickle et al., Phys. Rev. Lett. **96**, 070603 (2006)

[21] S. Aumaître, S. Fauve, S. McNamara and P. Poggi, Eur. Phys. J. B, **19** 449 (2001); S. Aumaître, PhD thesis, Ecole Normale Supérieure de Lyon, March 1999

[22] T. Gilbert, Europhys. Lett. **67**, 172 (2004)

[23] E. Falcon et al., Phys. Rev. Lett. **100**, 064503 (2008)

[24] N. Mordant, Phys. Rev. Lett. **100**, 234505 (2008); A. Boudaoud, O. Cadot, B Odille, and C. Touzé, Phys. Rev. Lett. **100**, 234504 (2008)

Part III

Fluctuations in Wave Systems

Chapter 4

Fluctuations in Surface Waves

In the present Chapter we review some basic results about waves at the interface between a horizontal fluid layer or between two inmiscible fluids. These systems are used as tools to study the properties of out-of-equilibrium stationary states that can develop from interacting waves. We will start by giving the working frame of wave propagation in Section 4.1, defining the dispersion relation and the wave equations of motion.

4.1 Wave motion

Waves can propagate over interfaces. We can observe them in different systems such as bending waves in elastic membranes and sheets [1, 2], Rayleigh waves or Love waves at the surfaces of elastic solids [3] or Rossby waves at the surface of the ocean [4]. We are used to see wave propagation every day at fluid surfaces as it is shown in Fig. 4.1, where the disturbances propagate at different speeds, with different wavelengths oscillating at different frequencies.

The way to relate these parameters, when the wave amplitude is small with respect to the wavelength, is through the dispersion relation of surface waves

$$\omega(\mathbf{k}, \{\theta\}) = \omega, \tag{4.1}$$

which relates the pulsation frequency ω with the wavevector $\mathbf{k}$ of a wave and the parameters of the fluid $\{\theta\}$ which enable wave propagation, such as its density ρ, surface tension σ, dielectric constant ϵ, etc. We will assume the fluid that sustains surface wave propagation is homogenous and isotropic, so the pulsation ω only depends on the modulus of the wave vector $|\mathbf{k}| = k$. This relation describes also the phase $c_p(k) = \frac{\omega(k)}{k}$ and group $c_g = \frac{\partial\omega(k)}{\partial k}$ velocities at a given wave vector. In this first approximation, we will not be concerned by viscous damping, as explained in the following sections.

The dispersion relation is also related to the restitution forces that sustain waves. In the next paragraph, we compute the dispersion of the surface waves in a fluid of depth h, in presence of gravity and surface tension.

4.1.1 Gravity-capillary waves

Waves are driven by gravity effects, when the fluid balances its inertia with the action of gravity that tries to keep its surface in its equilibrium flat possition with a heavier fluid under a lighter one. In contrast, waves are driven by capillarity when the restoring mechanism balances the curvature effects of the fluid surface and its inertia. The equations of wave propagation come from the fluid equations

Figure 4.1: Ripples at the surface of water.

of motion when the interface dynamics are taken into account. To wit, we consider the case of two inmiscible and inviscid fluids indexed by $i = 1, 2$. We will assume that the fluids are contained in a box of height $2h = h_1 + h_2$ and unbounded in the orthogonal coordinates $\mathbf{r} = (x, y)$. $\eta(\mathbf{r}, t)$ corresponds to the surface elevation between them, ρ_1 is the density of the bottom fluid ($-h_1 < z < \eta$), ρ_2 the density of the upper fluid ($\eta < z < h_2$) with $\rho_1 > \rho_2$ and σ the surface tension coefficient between the two fluids. The velocity fields $\mathbf{v_i}(\mathbf{r}, t)$ are governed by the incompressible Euler equations

$$\begin{aligned} \nabla \cdot \mathbf{v}_i &= 0, \\ \left[\frac{\partial \mathbf{v}_i}{\partial t} + \mathbf{v}_i \cdot \nabla \mathbf{v}_i\right] &= -\frac{\nabla p_i}{\rho_i} + \mathbf{g}, \end{aligned} \tag{4.2}$$

where the first equation is the flow incompressibility condition and the second equation is just the momentum conservation. Here, ∇p_i is the pressure gradient across the fluid of density ρ_i and $\mathbf{g}$ is the acceleration of gravity, pointing vertically in the $\hat{\mathbf{z}}$ direction. The normal velocity of the fluid should be zero at the solid boundaries of the container, which means

$$\mathbf{v}_1(z = -h_1) \cdot \hat{\mathbf{z}} = \mathbf{v}_2(z = h_2) \cdot \hat{\mathbf{z}} = 0, \tag{4.3}$$

where we have chosen the normal to the solid boundaries in the $\hat{\mathbf{z}}$ direction. At the interface between the fwo fluids, the velocity fields $\mathbf{v}_i$ must satisfy the kinematic continuity condition

$$\frac{\partial \eta}{\partial t} + \mathbf{v}_i \cdot \nabla_\perp \eta = \mathbf{v}_i \cdot \hat{\mathbf{z}} \tag{4.4}$$

where $\mathbf{v}_i$ is evaluated at the interface $z = \eta(\mathbf{r}, t)$ and $\nabla_\perp$ stands for the gradient in the $\mathbf{r}$ coordinates.

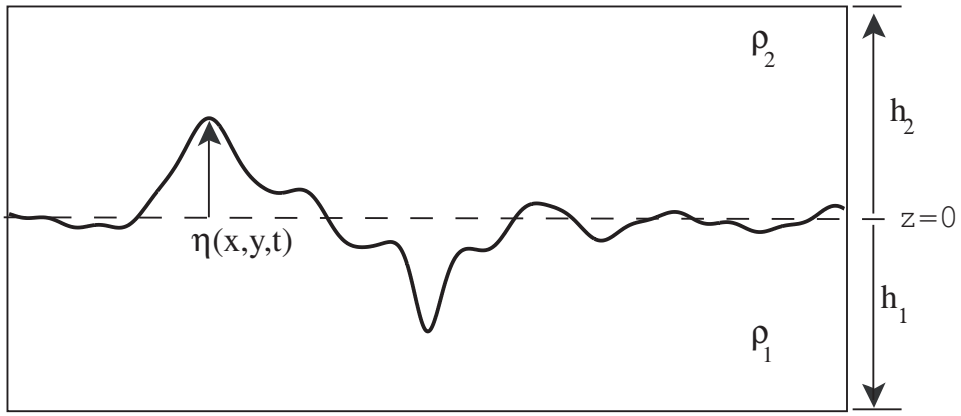

Figure 4.2: Local amplitude perturbation $\eta(x, y, t)$ of the interface (at $z = 0$) between two inviscid inmiscible fluid layers of depths h_1 and h_2. The fluid densities are ρ_1 and ρ_2 respectively.

The propagation of waves is a dynamic phenomenon. Therefore, we need a dynamic condition over the force balance across the interface to explain the mechanism of wave propagation. In absence of viscous stresses, this is given by the pressure difference $\Delta p = p_1 - p_2$ between the upper and lower fluid, normal to the free surface. This pressure jump across the interface $z = \eta(\mathbf{r}, t)$ is given by the Laplace force related to the principal radii of curvature R_1 and R_2, namely,

$$\Delta p = \sigma \left(\frac{1}{R_1} + \frac{1}{R_2} \right) = -\sigma \nabla_\perp \cdot \frac{\nabla_\perp \eta}{(1 + |\nabla_\perp \eta|^2)^{1/2}}, \tag{4.5}$$

where the last term is just the mathematical expression of the mean curvature $\kappa = \left(\frac{1}{R_1} + \frac{1}{R_2} \right)$ of the surface $\eta(\mathbf{r}, t)$ at the point $\mathbf{r}$.

When the surface is in equilibrium, it rests flat. In this state the the velocity fields are zero and pressure fields follow the hydrostatic solution of Eq. (4.2), i.e. $p_i^{eq} = -\rho_i g z$. As the interface is deformed, the hydrostatic solution does not hold. The velocity fields generate deformations across the surface, which in turn create a dynamic pressure component. These disturbances must satisfy Eqs. (4.2) and the boundary conditions (Eqs. (4.3) and (4.4)). We will simplify the problem by assuming that the perturbed velocity fields are irrotational $\nabla \times \mathbf{v}_i = 0$. By Thompson's theorem [1], this is true for all times when the fluid is inviscid. The irrotational condition means that $\mathbf{v}_i$ can be determined from a potential function ϕ_i as $\mathbf{v}_i = -\nabla \phi_i$. Therefore, Eqs. (4.2) can be written as

$$\begin{aligned} -\nabla^2 \phi_i &= 0, \\ -\nabla \left[\frac{\partial \phi_i}{\partial t} + \frac{|\nabla \phi_i|^2}{2} \right] &= -\frac{\nabla p_i}{\rho_i} + \mathbf{g}, \end{aligned} \tag{4.6}$$

where the first equation is just the definition of an harmonic field and the second is Bernoulli's equation of energy conservation. This condition is fulfilled over the whole fluid, including its free surface. The whole condition can be rewritten as a first integral of the hydrodynamic problem, namely as

$$\rho_i \frac{\partial \phi_i}{\partial t} + \rho_i \frac{|\nabla \phi_i|^2}{2} + p_i + \rho_i g z = B,$$

with B a constant that can be introduced in p_i or in ϕ_i to renormalise its value, given the fact that only pressure differences and velocities $\nabla \phi_i$ are important in the dynamical evolution of disturbances. Now, we can state the problem in terms of only two types of variables: the potential functions ϕ_i,

which generate the pressure differences and velocity fields *inside* the fluids and η which relates the pressure jump *across* the fluids. We write the kinematic

$$\frac{\partial \eta}{\partial t} + \nabla_\perp \phi_i \cdot \nabla_\perp \eta = \frac{\partial \phi_i}{\partial z}, \tag{4.7}$$

and dynamic

$$(\rho_1 - \rho_2) g\eta + \rho_2 \frac{\partial \phi_2}{\partial t} - \rho_1 \frac{\partial \phi_1}{\partial t} + \frac{1}{2}\left[\rho_2 |\nabla \phi_2|^2 - \rho_1 |\nabla \phi_1|^2\right] = -\sigma \nabla_\perp \cdot \frac{\nabla_\perp \eta}{(1 + |\nabla_\perp \eta|^2)^{1/2}} \tag{4.8}$$

conditions evaluated at the free interface $z = \eta(x, y, t)$. In the former conditions, nonlinearities can be neglected if we assume that the disturbances across the interface are small with respect to the wavelength ($\nabla_\perp \eta \ll 1$). In this linearized case, the evaluated fields at the interface $z = 0$ for small amplitude of the perturbations satisfy

$$\begin{aligned} \frac{\partial \eta}{\partial t} &= \frac{\partial \phi_i}{\partial z}|_{z=0}, \\ (\rho_1 - \rho_2) g\eta + \sigma \nabla_\perp^2 \eta &= -\left[\rho_2 \frac{\partial \phi_2}{\partial t} - \rho_1 \frac{\partial \phi_1}{\partial t}\right]|_{z=0}. \end{aligned} \tag{4.9}$$

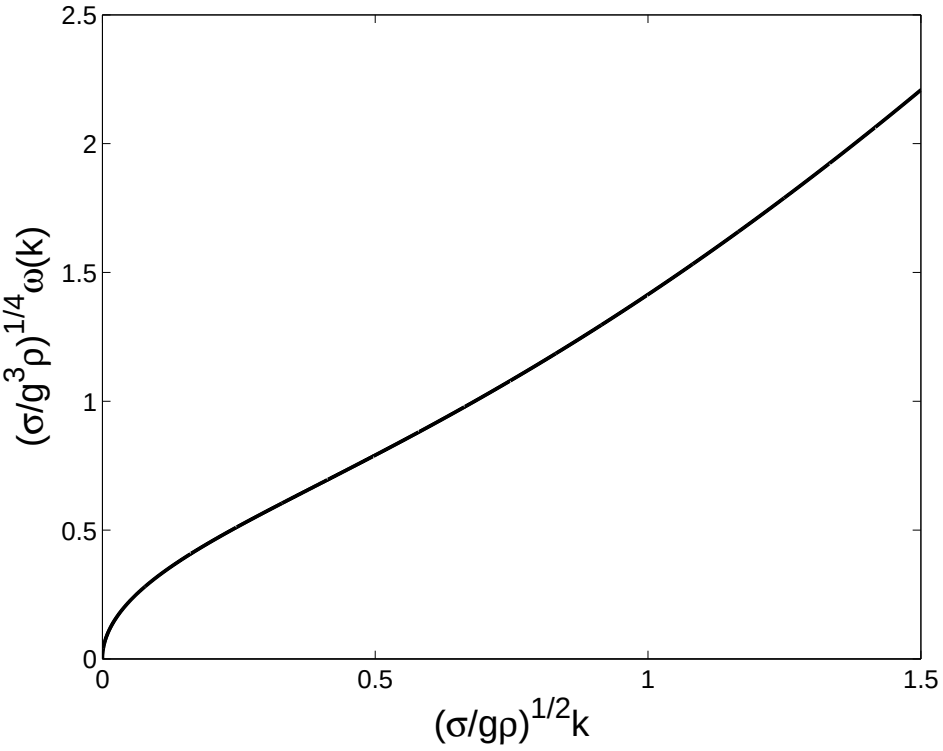

Figure 4.3: Adimensional dispersion relation $(\frac{\sigma}{g^3 \rho_1})^{1/4} \omega(k)$ for gravity-capillary waves as a function of the adimensional wave vector $(\frac{\sigma}{g\rho_1})^{1/2} k$.

To study wave propagation and the dispersion relation, we consider sinusoidal disturbances of the interface $\eta(\mathbf{r}, t) = \eta_0 \exp i(\mathbf{k}_\perp \cdot \mathbf{r} - \omega t)$ and of the potential functions $\phi_i(\mathbf{r}, z, t) = f_i(z) \exp i(\mathbf{k}_\perp \cdot \mathbf{r} - \omega t)$, where $\mathbf{k}_\perp$ is the orthogonal wave vector and $|\mathbf{k}_\perp| = k_\perp = k$. The separation of the potential functions in orthogonal and vertical components is related to Eq. (4.3), which states that their

normal derivative to the solid boundaries are zero. From the harmonic definition of $\nabla^2\phi_i = 0$, the potential functions satisfy the equations

$$\frac{d^2 f_i(z)}{dz^2} - k^2 f_i(z) = 0,$$

subjected to the boundary conditions $f_1(z = -h_1)' = f_2(z = h_2)' = 0$ with $(\cdot)'$ the derivative with respect to the z coordinate. The equations for both $f_i(z)$ are of second order, therefore, two constants are needed to calculate the full solution. Using the boundary conditions, we can write

$$f_1(z) = f_1^0 \frac{\cosh k(z + h_1)}{\cosh kh_1}, \qquad f_2(z) = f_2^0 \frac{\cosh k(z - h_2)}{\cosh kh_2},$$

where f_i^0 can be traced back to the initial surface perturbation η_0, using the dynamic condition of pressure difference. Through the kinematic condition of velocity continuity normal to the interface (Eq. (4.4)), we have

$$-i\omega\eta_0 = f_1^0 k_\perp \tanh(kh_1) = -f_2^0 k_\perp \tanh(kh_2).$$

These relationships, coupled to pressure jump across the interface of Eq. (4.9), gives the dispersion relation

$$\omega^2 = \frac{(\rho_1 - \rho_2)gk + \sigma k^3}{\rho_1 \coth kh_1 + \rho_2 \coth kh_2}. \tag{4.10}$$

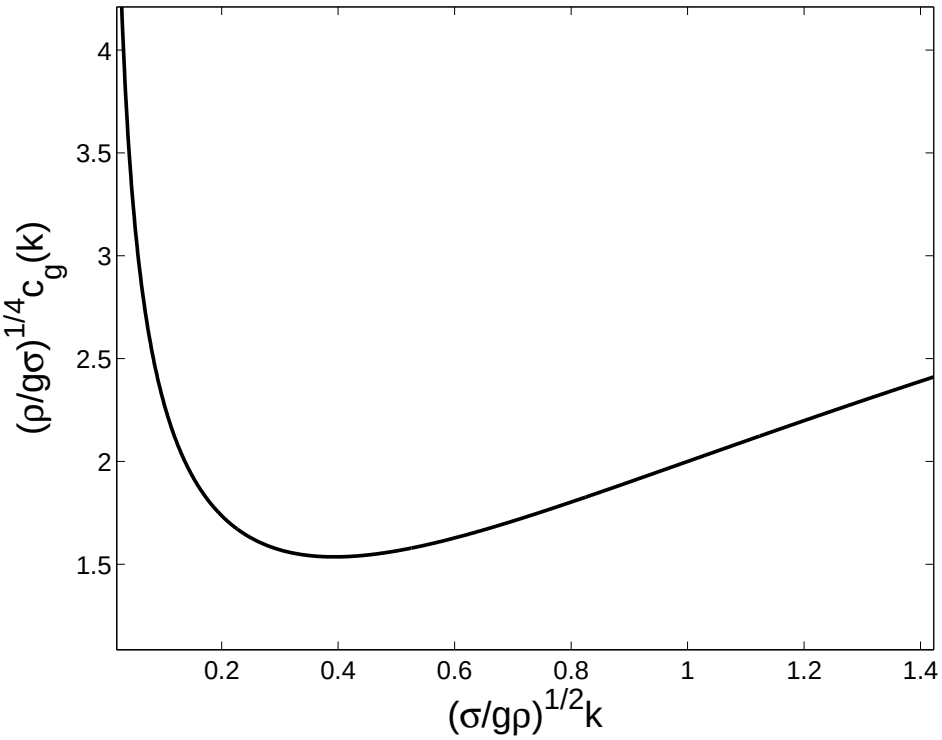

Figure 4.4: Adimensional group velocity $(\frac{\rho_1}{g\sigma})^{1/4} c_g(k)$ for gravity-capillary waves as a function of the adimensional wave vector $(\frac{\sigma}{g\rho_1})^{1/2} k$.

With this expresion we can relate the wavelength $\lambda = \frac{2\pi}{k}$ with the pulsation frequency of a perturbation $\omega = \omega(k)$. The above relation displays several interesting limits. When $\rho_2/\rho_1 \ll 1$, the

dispersion relation reads

$$\omega^2 = \left[gk + \frac{\sigma}{\rho_1} k^3 \right] \tanh kh_1.$$

This is the typical case of a liquid-vapor interface (such as air-water or nitrogen-mercury interfaces, used in the following chapters). The first term on the right hand side is related to gravity and the second to capillary forces. The multiplicative term $\tanh(kh_1)$ is related to the effect of the characteristic penetration length of the wave (which in this case is of the order of the wavelength) on the propagation of a wave in a finite depth layer h_1 of fluid.

From this expression, we can see there are two cross-over lengths. One, where the effects of both restitution forces are equal $l_c = \sqrt{\frac{\sigma}{\rho_1 g}}$ and another one where the depth of the layer is comparable to the wavelength. For infinite depth ($kh_1 \gg 1$) the multiplicative term is constant. In this regime, the waves with wavelengths larger than l_c propagate with a pulsation frequency $\omega_g = \sqrt{gk}$ and are called gravity waves. The phase velocity $c_p(k) = \frac{\omega(k)}{k} = \sqrt{g/k}$, that is, the velocity at which a front of constant phase $\psi = \mathbf{k}_\perp \cdot \mathbf{r} - \omega(k_\perp)t$ propagates, is larger as the wavelength is larger. The group velocity $c_g(k) = \frac{\partial \omega(k)}{\partial k} = \sqrt{g/4k}$, that is the velocity at which a wave modulation in amplitude propagates, is twice as small as the phase velocity. This means that waves with large wavelength propagate faster than waves with smaller wavelength.

When the wavelength is smaller than l_c, the dispersion relation reads $\omega(k) = (\frac{\sigma}{\rho_1})^{1/2} k^{3/2}$. The waves that follow this relationship are called capillary waves. The phase velocity $c_p(k) = \frac{\omega(k)}{k} = (\frac{\sigma}{\rho_1})^{1/2} k^{1/2}$ is larger as the wavelength is smaller. The group velocity $c_g(k) = \frac{\partial \omega(k)}{\partial k} = \frac{3}{2}(\frac{\sigma}{\rho_1})^{1/2} k^{1/2}$ is larger than the phase velocity. Therefore, as a wave packet containing wavelengths smaller than l_c propagates, its shape changes as the small wavelengths propagate faster than the larger ones. Surface waves on fluid surfaces are dispersive because of this latter fact: wave packets do not maintain their shape as they propagate.

When we take into account wavelengths that are comparable to the fluid depth of the layer h_1, the dispersion has to take into account this fact. In this limit, $\tanh kh_1 \sim kh_1$ and, hence, we can express the pulsation frequency as $\omega(k) = \sqrt{gh_1}k$. With this expression, we can see that wave propagation is non-dispersive for large wavelength with a constant velocity $c_g = c_v = \sqrt{gh_1}$.

We can also calculate the dispersion relation by energy considerations, given the fact that waves transport energy, as well as momentum. To simplify the calculations we consider the limit where $\rho_2/\rho_1 \ll 1$, so we can neglect the upper fluid. The energy E of the system can be written as a kinetic contribution

$$K = \rho_1 \int_V \frac{v^2}{2} dV,$$

and a potential contribution

$$U = \rho_1 g \int_V z dV + \sigma \int_{\partial V} dA,$$

where V stands for the volume of the fluid of density ρ_1 and ∂V its free surface. We will use the equipartition of energy $\overline{K} = \overline{U}$, where $\overline{(\cdot)}$ stands for the average over a period of the wave oscillation. This approach will only be valid in the small amplitude aproximation, as it will be discussed in following sections. The gravitational term of the potential energy can be rewritten as

$$U_g = \rho_1 g \int d\mathbf{r} \int_{-h_1}^{\eta} z dz = \rho_1 \frac{g}{2} \int \eta^2 d\mathbf{r} + U_g^0,$$

where U_g^0 is constant. The surface component of potential energy can be expressed as

$$U_c = \sigma \int \sqrt{1+|\nabla\eta|^2} d\mathbf{r} \simeq \frac{\sigma}{2}\int |\nabla\eta|^2 d\mathbf{r} + U_c^0,$$

where, as before, U_c^0 is constant. Therefore, the equipartition of energy then reads,

$$\overline{\int_{-h_1}^{\eta} dz \int \frac{\rho_1 |\nabla\phi|^2}{2} d\mathbf{r}} = \overline{\frac{1}{2}\int \left[\rho_1 g\eta^2 + \sigma|\nabla\eta|^2\right] d\mathbf{r}} \tag{4.11}$$

for kinetic and potential energy averged over a wave period. We can use the solutions of Eqs. (4.3) and (4.4), to relate both the potential and interface disturbances. This approach can be useful to estimate also the bulk dissipation of the fluid in the small viscosity limit, as we will will see next.

4.1.2 Viscous effects in gravity-capillary waves

When we take into account the viscosity effects in the fluid, we cannot assume the flow to be potential everywhere. Even for small values of the kinematic viscosity ν, vorticity, which is just the curl of the velocity field $\nabla\times\mathbf{v}$ is non-zero. It is generated in small and shallow layers close the boundaries where the velocity field suffers strong shear. The penetration length δ, that is, the typical size of the boundary layer where the fluid is not potential can be estimated by balancing the temporal derivative of the velocity field $\frac{\partial\mathbf{v}}{\partial t}$ and the viscous term $\nabla^2\mathbf{v}$ in the Navier-Stokes equation as $\delta \sim \sqrt{\nu/\omega}$.

Using the same simple analysis one can estimate the bulk dissipation in the fluid. To do so, we assume that viscosity is low, therefore we can neglect the boundary layer contribution to the kinetic energy. Also, for simplicity we can assume that we are in the "deep layer limit" $kh_1 \gg 1$, where the flow does not reach the bottom. In this limit, the dissipation rate of the energy γ can be estimated by $\gamma = \overline{\frac{P_{diss}}{E}} = \overline{\frac{P_{diss}}{2K}}$. The dissipated power by viscous stresses $P_{diss]}$ is given by

$$P_{diss} = \frac{1}{2}\rho_1\nu\int_V e_{ij}^2 dV,$$

where e_{ij} is the second order tensor related to the symmetric part of the velocity gradients. Since we have assumed that the viscous layer is negligible and thinner than the layer depth, we can express P_{diss} as

$$P_{diss} = \frac{1}{2}\rho_1\nu\int_V \left(\frac{\partial^2\phi}{\partial x_i \partial x_j}\right)^2 dV = 8\rho_1\nu k^4 \int_V \overline{\phi^2} dV.$$

Therefore, the dissipation rate is just $\gamma = 2\nu k^2$. Using the Navier-Stokes equation, we can also estimate the surface layer contribution $\gamma_S = (\nu k^2)^{3/2}\omega_k^{-1/2}$ to the damping of surface waves, which is of higher order in the viscosity, and can be neglected in the present analysis[7]. As for the boundary layer contribution γ_B, it can be found from dimensional analysis, when one balances the dissipated power over the bondary of depth δ with the kinetic energy of the fluid in the layer. Taking δ as the characteristic scale where the velocity field gradients and v_0 its characteristic value, the dissispated power due to viscous stresses per unit of area is $P_{diss} \sim \rho_1\nu v_0^2/\delta$. The kinetic energy per unit of area, on the contrary, is going to be integrated over a characteristic distance l as $\sim \rho_1 v_0^2 l$. In the small viscosity limit, $\delta \ll l$ we will not get any contribution of the boundary layer dissipation rate for a deep layer layer of fluid $kh_1 \gg 1$, because the waves only penetrate close to the free surface over a distance of the order of the wavelength. For shallow layers, that is, in the limit $kh_1 \ll 1$, the wave generated flow reaches the bottom of the fluid and therefore the typical length l is of the order of the fluid depth. In this case, the dissipation rate related to the boundary layer is $\gamma_B \sim \nu/\delta h_1 \sim \sqrt{\nu\omega}/h_1$.

Bibliography

[1] A. L. Fetter and J. D. Walecka, *Theoretical Mechanics for Particles and Continua* (McGraw-Hill, New York, 1980)

[2] L. D. Landau, L. P. Pitaevskii, A. M. Kosevich and E.M. Lifshitz, *Course of theoretical Physics, Volume 7* (Butterworth-Heinemann, 3rd edition, New York, 1986)

[3] A. E. Love, *Treatise on the Mathematical Theory of Elasticity* (Dover Publications, 4th edition, New York, 1927)

[4] J. Lighthill *Waves in Fluids* (Cambridge University Press, Cambridge (1978))

[5] G. B. Whitham, *Linear and Nonlinear Waves*, (John Wiley & Sons, New York (1974))

[6] E. Guyon, J. P. Hulin and L. Petit, *Hydrodynamique physique* (Editions du CNRS, Meudon (1991))

[7] S. Fauve, "Waves on interfaces" in *Free Surface Flows*, International Centre for Mechanical Sciences Courses and Lectures, No. 391 (Springer- Wien, New York, 1998)

[8] L. D. Landau and E.M. Lifshitz, *Course of theoretical Physics, Volume 6* (Butterworth-Heinemann, 3rd edition, New York, 1986)

Chapter 5

Fluctuations in Parametrically Excited Surface Waves

We present in this chapter two experimental studies on the statistical properties of the local amplitude fluctuations of parametrically excited waves at the surface of a fluid layer. We recall first the mechanism of parametric amplification of surface waves by means of a simple amplitude equation of the envelope close to the instability threshold. In Section 5.1, following these theoretical considerations, we present our experimental studies. First, in Section 5.2, we study the local dynamics of wave amplitude fluctuations in an out-of-equilibrium stationary state refered to as *defect-mediated turbulence*, where defects appear over the pattern of standing waves. We describe this turbulent-like regime and characterize its appeareance by means of the qualitative changes of the PDF and PSD of the local wave amplitude. Then, in Section 5.3, we present an experimental study on the effect of spatio-temporal fluctuations on a set of parametrically amplified surface waves. An underlying vortex flow generated by a periodic Lorentz force takes place over the bulk of a conducting fluid (in this case mercury) acting as the source of these fluctuations. For that matter we measure both the local wave amplitude and velocity field of the parametric surface waves. We show that the main effects of these spatio-temporal fluctuations are to increase the threshold value of the parametric instability and also to decorrelate the wave amplitude in different places over the container, making the parametrically amplified mode lose its coherence over the container.

5.1 Parametric Amplification of Surface Waves

The fundamental idea behind parametric amplification is the temporal or spatial modulation of the frequency of an oscillator or a wave to achieve an exponential growth of their amplitude. It was first experimentally studied by Faraday [1]. He realized that a set of surface waves on a layer of fluid appear when the container was vibrated periodically at a given frequency. In his experimental set-up, a set of standing waves oscillating at half the forcing frequency (twice the period T of the forcing) appeared over the whole surface, when a threshold value of the control parameter (the vibration amplitude) was surpassed. These waves formed a pattern with different geometries, depending on the frequency and amplitude of the forcing. This instability was then given theoretical background when Mathieu[2] studied the motion of an oscillating elliptic membrane. It has become clear that parametric resonance is involved in several processes and areas of physics, ranging from optical and electronic parametric amplification to Bragg scattering in periodic lattices and energy bands in solid state physics[3].

To ilustrate this phenomenon in surface waves, we write the evolution equation for the amplitude $\eta_k(t)$ of the mode with wave number k and pulsation ω_k given by the dispersion relation. Benjamin and Ursell[4] have shown that $\eta_k(t)$ follows a Mathieu equation

$$\ddot{\eta_k}(t) + \omega_k^2(1 + \Gamma_k \cos(\Omega t))\eta_k(t) = 0, \tag{5.1}$$

in the linear aproximation for vanishing kinematic viscosity ν (negligible viscous layer $\delta h \sim \sqrt{\nu/\omega_k^2}$). Here, ω_k^2 satisfies the dispersion relation of surface waves, Γ_k is the parametric forcing amplitude and Ω is the forcing frequency. In the case where the aceleration of gravity is modulated sinusoidally $g_{eff}(t) = g + a\cos(\Omega t)$, as it is in Faraday's experiment where the container is shaken. Γ_k can be written as $\Gamma_k = ak/\omega_k^2$ for a deep layer of fluid[5].

Following the experimental findings of Faraday regarding the subharmonic behavior of the standing surface waves, we choose $\Omega = 2(\omega_k + \Delta)$, where Δ is called the detunning and represents the mismatch between the eigenfrequency ω_k of the surface wave of wave number k and the subharmonic frequency of the standing wave pattern $\Omega/2$. The first mode of wave number k_c to be amplified is the one with the smallest detunning at a given critical forcing amplitude Γ_{k_c}. Close to the instability onset $\gamma = \varepsilon\Gamma_k$ ($\varepsilon \ll 1$) of the flat surface we can derive an assymptotic normal form for the amplitude of the mode with wave number k_c by writing $\delta = \varepsilon\Delta$. Here ε is a small parameter associated with the time scale separation between the fast time scale $t \sim \omega_k^{-1}$ (related to the wave pulsation period of oscillation) and the slow time scale $T = \varepsilon t$ which corresponds to the instability growth rate. We expand

$$\eta_k(t) = A(T)e^{i\frac{\Omega}{2}t} + \overline{A}(T)e^{-i\frac{\Omega}{2}t} + h.o.t.,$$

where $A(T)$ is a complex amplitude, $\overline{A}(T)$ is its complex conjugate and higher order terms (h.o.t.) close to the instability threshold. The variable A describes the slow dynamical evolution of the envelope of the standing wave pattern at frequency $\Omega/2$. Applying what is called a solvability condition, i.e. a condition to eliminate from the solution $\eta_k(t)$ secular terms that grow on a time scale of the order $\sim \varepsilon t$, we find the evolution equation of the slow time dynamics of the envelope

$$\partial_T A = -i\delta A + i\frac{\gamma}{8}\overline{A}.$$

Phenomenologically, we can add the effect of dissipation in the limit of vanishing viscosity as $\Lambda = \varepsilon\lambda$ and nonlinear saturation by symmetry arguments to the lowest order in the developement in powers of ε. In that case, one can write a phenomenological equation for the evolution of the nonlinearly saturated wave amplitude

$$\partial_T A = -(\lambda + i\delta)A + i\frac{\gamma}{8}\overline{A} + \beta|A|^2 A, \tag{5.2}$$

where β is a complex number associated with nonlinear renormalization of the amplitude (real part of β) and frequency (imaginary part of β). This equation is known as the complex Ginzburg-Landau equation with parametric forcing and has been extensively studied in several out-of-equilibrium systems[6]. It can be rigorously calculated for the parametrically forced pendulum, where all the coefficients can be computed. The threshold value of the instability is found by balancing the the forcing term γ coming from the parametric forcing with the dissipation and detunning. A straightforward calculation gives the instability threshold curves $\gamma_c^2 = \lambda^2 + \delta^2$. When the normalized control parameter $\epsilon = (\gamma - \gamma_c)/\gamma_c$ is larger than zero, the flat surface becomes unstable to small perturbations and a mode of wave number k_c grows and invades the whole space. A set of standing waves appear oscillating at a frequency $\Omega/2$, forming a pattern. For working fluids such as mercury

and water, the pattern geometry is made of squares. Depending on the sign of the detunning Δ, the nonlinearly saturated wave amplitude behaves differently as ϵ grows, as it is shown in Fig. 5.1. For positive detunning, the behavior of the nonlinearly saturated wave amplitude A is supercritical and there is no coexistance with the flat solution $A = 0$. For negative detunning, A behaves subcritically and there exists a hysteresis loop that connects the nonzero and the flat solution. In the particular case where $\Delta = 0$, the real part of $\beta = 0$ and quintic terms must be taken into account to saturate A.

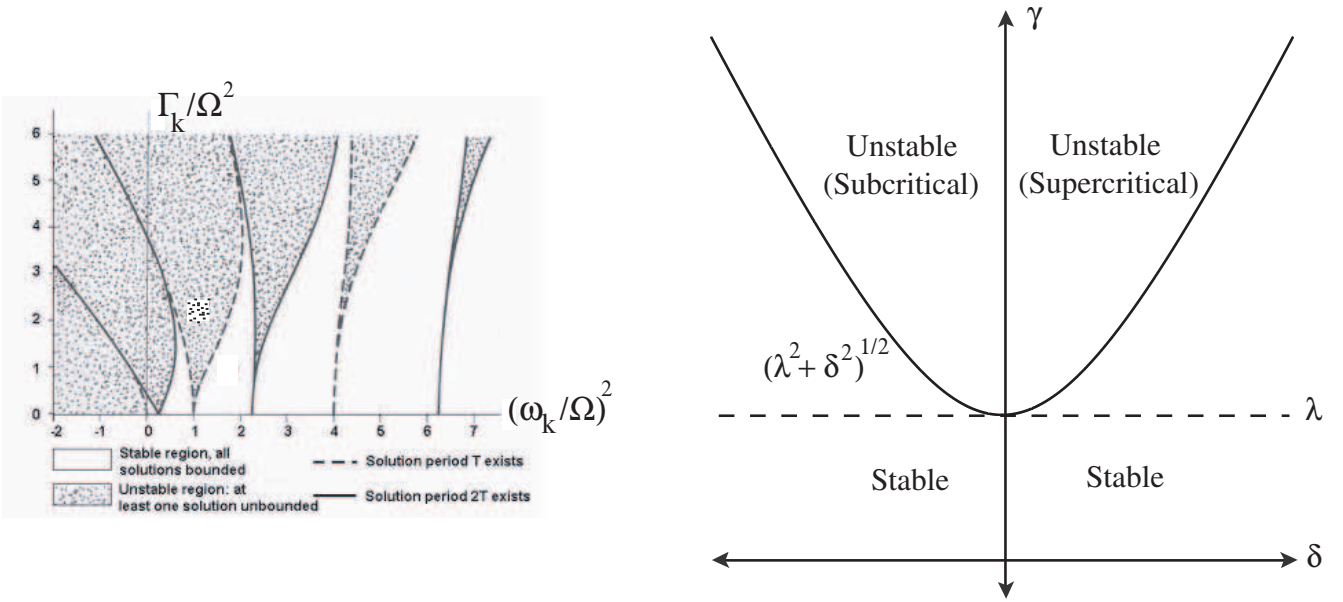

Figure 5.1: **Left:** Parametric instability curves curves for the Mathieu equation as it is written in Eq. (5.1) for different values of Γ_k, Ω and ω_k. **Right:** Instability curve close to the first parametric resonance curve for the reduced parameters γ, δ and λ.

This simple approach deals with the case of the amplification of one single mode. When the forcing amplitude is larger than threshold, a set of wave numbers k close to k_c can be also amplified. It was shown experimentally that secondary instabilities develop in parametrically amplified surface waves either at zero wave number (drift instability[7]) or at finite wave number (oscillatory instability of the k_c mode[8]). Further increase in the control parameter will lead to a larger ammount of mode coupling that can be taken into account in Eq.(5.2) to the lowest order in ϵ by adding a spatial coupling of the form $\alpha\partial_{XX}A$. Here, α is a complex number associated with diffusion (real part of α) and dispersion (imaginary part of α) and ∂_X is a large scale derivative associated with the wave number mismatch $\Delta k = k - k_c$. It is in this context that the amplitude evolution displays interesting and complex dynamics, such as kinks, domains, localized structures and turbulent-like regimes[9]. This last type of regime will be the focus of the next section, in which we study experimentally the local dynamics of the standing waves in the turbulent-like regime called *defect-mediated turbulence*.

5.2 Defects and Defect-mediated turbulence in parametrically excited surface waves

As the normalized control parameter ϵ increases, more and more modes within the gap of wave numbers $k \pm \Delta k$ are amplified and nonlinearly interact. If the gap $k \pm \Delta k$ is large enough, this mode-

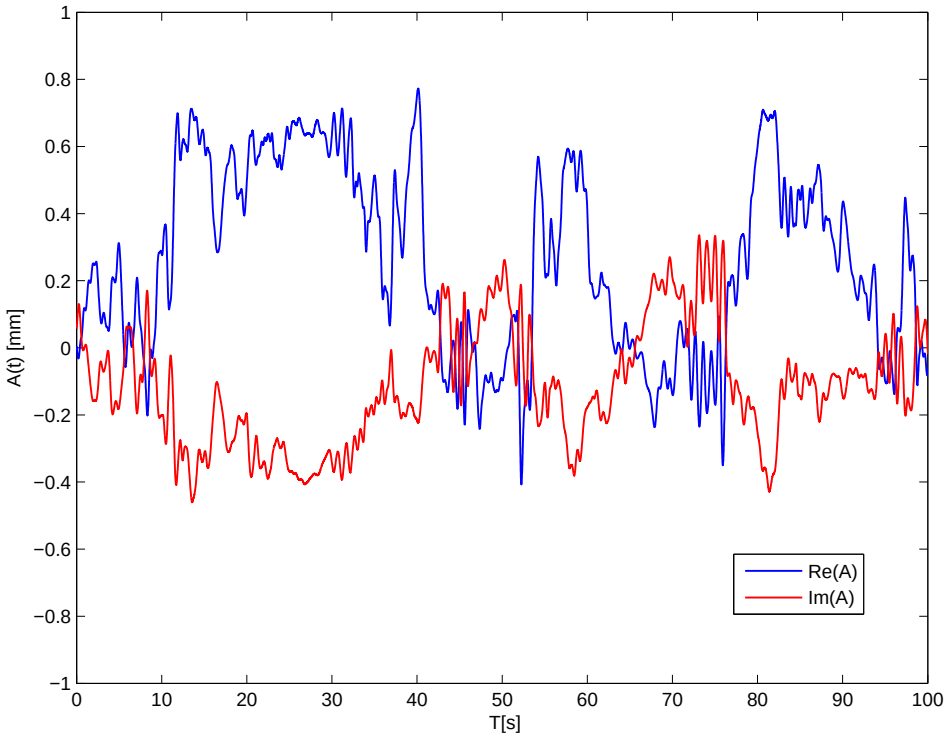

Figure 5.2: Real $Re(A)$ (blue) and imaginary $Im(A)$ (red) parts of the complex amplitude of the local wave pattern for $\epsilon = 1.41$. The locations where $A \simeq 0$ correspond to *defects*.

coupling dynamics will generate a fluctuating state where large fluctuations of the wave amplitude occur, large enough to make A approach zero in certain places at a given time. The transition from the stationary deterministic state where the complex amplitude envelope A is constant to a regime where spatio-temporal fluctuations of A occur, is achieved when the wave system is forced strongly in an out-of-equilibrium state by increasing ϵ.

There are several of these out-of-equilibrium states or turbulent-like regimes[10] that develop when cellular structures in dissipative systems are present, such as the pattern state of the parametrically amplified Faraday standing waves. Cellular structures in dissipative systems range from periodic fingers in directed solidification to oscillatory patterns in chemical reactions to convection rolls[9]. In all these cases, the amplitude envelope of the periodic field can be described by an evolution equation simlar to Eq.(5.2). For the complex amplitude envelope, the turbulent-like regime can be dominated either by phase or amplitude fluctations. In the case of phase turbulence[11], the amplitude of the wave pattern weakly depends on phase fluctuations. Therefore, no singularities in the amplitude take place, just small modulations related to the phase dynamics. When this separation between phase and amplitude dynamics no longer persists, the turbulent-like regime starts to be driven by imperfections in the pattern. The characteristic time scale of their dynamics is slow with respect to the typical time scale of the standing waves oscillation. Furthermore, their large scale fluctuations interact with the small scale of the underlying pattern, transfering the local perturbation from one place of the surface to another one. This is the so called *defect-mediated turbulence*[12], where the zeros of the wave amplitude appear at random over the pattern.

We study experimentally the dynamics and statistics of the zeros of the amplitude in the standing wave pattern. We present the experimental set-up in the following paragraph and the measuring techniques used to study the local amplitude dynamics.

5.2.1 Experimental set-up and measuring techniques

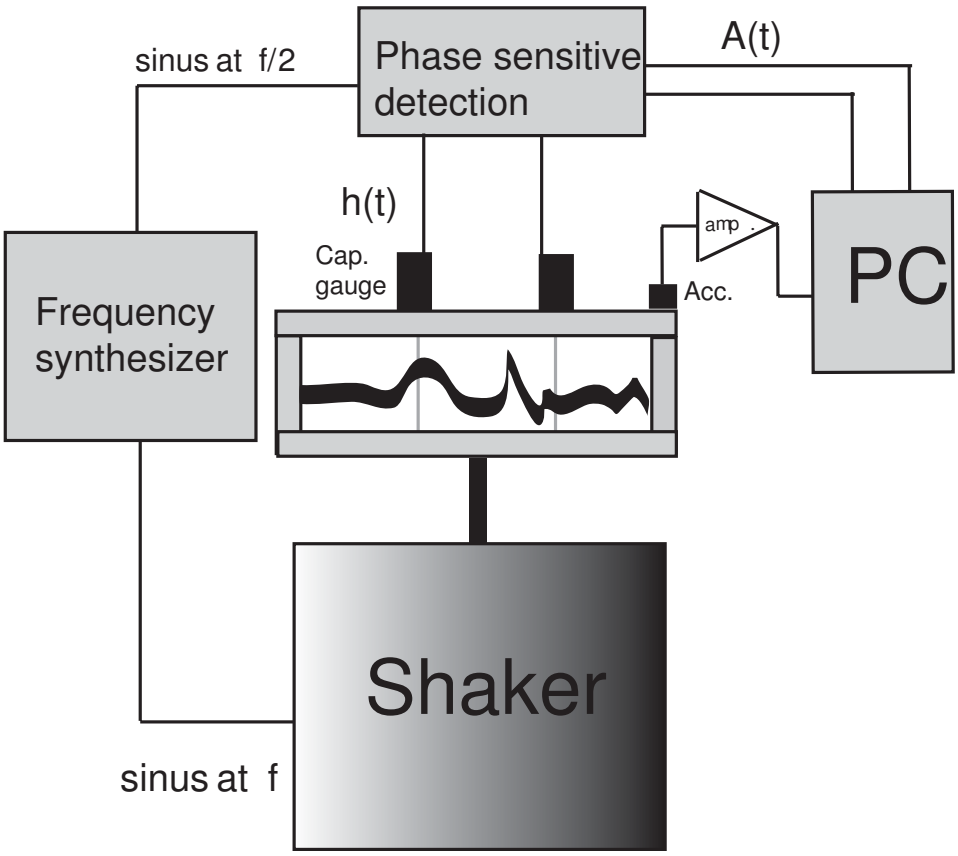

Figure 5.3: First experimental set-up: Waves at the surface of a water layer are parametrically amplified by periodic modulation of gravity which is measured by means of a piezoelectric accelerometer The local wave amplitude is measured by a capacitive gauge and later demodulated with a phase sensitive device at the subharmonic forcing frequency.

The schematic representation of the experimental set-up is shown in Fig.5.3. A 100 x 100 mm^2 Plexiglass container is filled with a 4 mm layer of water (density $\rho \simeq 10^3$ kg/m^3, kinematic viscosity $\nu \simeq 10^{-6}$ m^2/s and surface tension $\sigma \simeq 4.0$ x 10^{-2} N/m). In order to prevent evaporation of the fluid, the container is sealed with a Plexiglass plate and its temperature is controlled by circulating water at 20 $\pm$ 0.1 °C coming from a thermal bath (Lauda RC6 Chiller). To amplify parametrically the waves at the surface of the fluid, the whole container was mounted over an electromagnetic shaker (B & K 4809) driven by one of the two outputs of a frequency syntheziser (HP 8904 A). This provides a clean sinusoidal acceleration $g_{eff} = a\ cos(2\pi ft)$, where f is the excitation frequency and a is the maximum acceleration, proportional to the applied voltage V. We have chosen $f = 60$ Hz as the excitation frequency, although we also tested higher frequencies between 60 and 120 Hz. There is no qualitative difference in the pattern or in the local dynamics of the pattern defects. The vertical acceleration modulation g_{eff} is measured by a piezoelectric accelerometer (B & K 4803) fixed to the vibrating container, using a charge amplifier (B & K 2635).

The local wave amplitude is measured by two capacitive wire gauges, 0.1 mm in diameter, which are placed on one diagonal of the container, each one 2 cm away from its center. Screwed to the Plexiglass plate, they plunge perpendicularly to the fluid at rest. This technique, used mainly to measure the local height of quasi-static fluids, was applied to wavy liquids in an experiment of

wave turbulence [13]. The measuring principle of the local wave amplitude uses the fact that the capacitance of a annular capacitor, which plunges into a fluid, is proportional to the local height of the submerged part. The insulation (a varnish) of the wire gauge is then the dielectric of the annular capacitor with the wire as the inner conductor. The outer conductor is the fluid itself. For dielectric liquids, the measuring principle still holds, although the nature of the outer conductor is not clear. For an annular capacitor submerged in a dielectric liquid of dielectric constant ε_d, the capacitance C depends on $\varepsilon_d/\varepsilon_0$, ε_0 being the permitivity of vacuum, and linearly on the submerged length l, that is, the local fluid level. We have measured the capacitance C of the wire gauge with the help of a low-cost homemade analogic multivibrator acting as a capacitance meter with a response time of 0.1 ms. It can measure capacitances up to 200 pF. Depending on the dielectric constant of the fluid used to generate the waves, the linear sensing range and proportionality coefficients change. We have experimentally computed the proportionality coefficients for 3 different fluids (water, $\varepsilon_d = 88\varepsilon_0$, ethanol, $\varepsilon_d = 10\varepsilon_0$ and silicon oil, $\varepsilon_d = 2\varepsilon_0$), as shown in Table (5.2.1).

Fluid	Dielectric constant ratio $\varepsilon_d/\varepsilon_0$[1]	Proportionality constant [mm/V]
Water	88	20.15
Ehanol	24.3	0.12
Silicon Oil (PDMS)	2.2-2.9	0.02

For water-air interface the linear sensing range of the sensor allows waveheight measurements from 0.1 mm (the wire diameter) up to 2 cm with a 20 mm/V sensitivity. It can be also applied to fluid-fluid interfaces, as long as the dielectric ratio stays large (as it will be seen in the next chapter). Another important point is the dynamical range of the capacitance meter. The output of the multivibrator is low-passed filtered at 13 kHz with a Butterworth filter of order 6, but the dynamical content of the surface height fluctuations is also filtered at lower frequencies (f_{diss} ~100 Hz) by the dissipation of small scale waves at the meniscus, which is of typical size of 2 mm. For our working dynamical range, this measuring technique was previously checked with measurements performed with eddy current displacement transducers or with an optical determination of the local slope of the surface[14]. The temporal capacitance fluctuations are not polluted by the water meniscus motion formed at the local wire gauge.

Increasing the forcing amplitude a above a threshold value a_c, the flat surface is no longer stable to small pertubations and a square pattern of standing waves appear through the Faraday instability[1]. The temporal response to the sinusoidal gravity modulation at excitation frequency f of these waves is subharmonic. The surface waves make a pattern of squares with a wavelength λ of 4 mm at f=60 Hz. This is confirmed by optical observation with a stroboscopic light driven at $f/2$. At this frequency, no effect of the meniscus on the internal dynamics of the pattern was observed.

Taking the output of the capacitance meter, we have demodulated the local wave amplitude $h(t)$ at the subharmonic frequency as

$$h(t) = A(t)e^{i\frac{\omega}{2}t} + \overline{A(t)}e^{-i\frac{\omega}{2}t} + r(t),$$

where $\omega = 2\pi f$, A is the complex amplitude envelope and $\overline{A}$ its complex conjugate and $r(t)$ are higher frequency components. The higher harmonics in $r(t)$ are at least two orders of magnitude smaller than the main subharmonic response when the pattern is fully developed. To extract the slow dynamics of the envelope A we have used a phase-sensitive detection device (SR 830) driven by a carrier signal at frequency $f/2$. The carrier signal is taken from the second output of the frequency

[1]Values taken from HTTP://WWW.ASIINSTRUMENTS.COM/TECHNICAL/DIELECTRIC%20CONSTANTS.HTM

synthesizer to avoid spurious detunning between the harmonic and subharmonic modulations. In the demodulation process, the carrier and local wave amplitude signals are analogically multiplied. The product of both signals is low-pass filtered with a Butterworth filter of order 8 and a time constant of 100 ms and amplified. The resulting complex amplitude is separated in real and imaginary part.

The sampling frequency used to acquire the slow amplitude fluctuations is set at 1 kHz (unless stated differently, as shown below), to ensure a good resolution of the amplitude singularities. We show in Fig. (5.2) typical temporal traces of the real and the imaginary part $(Re(A), Im(A))$ of the complex amplitude envelope A in the dynamical regime of interest where large fluctuations in the wave pattern occur, making possible the rough cancellation of both $Re(A)$ and $Im(A)$, i.e., forming a defect. In this experimental configuration, defects are lines dividing two regions where the amplitude in one region is in phase opposition from the other. In terms of the local wave amplitude a defect is a line where the envelope passes through zero, i.e. $A = 0$, which means both the imaginary and real part of the complex amplitude are zero. These separation lines cross the container from one wall to the other along the pattern in every direction: from the upper to lower wall, from left to right or running through the diagonals of the container. The passage of these phase jumps along the separation line is measured punctually by the capacitive gauge. The resolution of the capacitive gauge is of the order of 0.1 mm.

5.2.2 Experimental results

Now, we describe the appearence of defects in the pattern of standing waves. Fixing the excitation frequency f at 60 Hz and increasing the reduced control parameter $\epsilon = (a - a_c)/a_c$ from negative to positive value, the first instability of the system occurs, where the standing parametric waves appear, oscillating at half the frequency of the forcing. At the threshold $\epsilon = 0$, only the subharmonic component in the wave system appears with a defined wave number $k_c = 2\pi/\lambda$ ($\lambda \sim$2 mm) given by the dispersion relation $\omega_c = \omega(k_c) = \pi f$. At this frequency, there is no observable detunning between the eigenfrequency ω_c and πf[15]. This means that no slow modulation of the complex amplitude appears. Hence, demodulating the local wave amplitude response provides the constant amplitude of the envelope of the pattern. Increasing ϵ further, secondary instabilities develop, as described in the preceeding section, either at zero wave number (the so called drift instability where the pattern "drifts" in a given direction at constant speed) or at finite wave number. This later secondary instability is known as an oscillatory instability, and it occurs at nonzero wave number k_c. In our experimental set-up, due to the boundary conditions of the cell, it is this later type of secondary instability that appears, at a very low frequency $\delta f \sim 1$ Hz (in this case 30 or 40 times the period of the basic pattern). δf is of the same order of magnitude of the frequency associated to the bandwith Δk related to the finite size L=100 mm of the container $\Delta k \sim 2\pi/L$. These low-frequency oscillations appear one after the other as higher harmonics of δf when ϵ is constinously increased. There is a strong hysteresis in the control parameter in the oscillatory regime. For instance, the first hysteretic loop (in between oscillations at δf and $2\delta f$) ranges from ϵ =0.7 to 0.9. In the process from the stationary amplitude regime where A is constant to the slowly oscillating one, no phase turbulence is observed. This is confirmed by extracting the local phase dynamics ϕ of the complex amplitude envelope A ($\phi = arg(A)$). No abrupt fluctuations in its time derivative $\dot{\phi}$ are found, as it should be in the case of a phase-turbulent regime[16]. This is due to the fact that parametric instabilities have a strong phase-locking between the forcing modulation and the system response. For larger values of ϵ, the regime where secondary instabilites dominate, defects appear in the wave pattern, as described above. We measure the local passage of a defect over the capacitive gauge by measuring in the temporal trace these singular points where A vanishes. A typical trace of a defect

profile in the wave pattern is shown in Fig. (5.4).

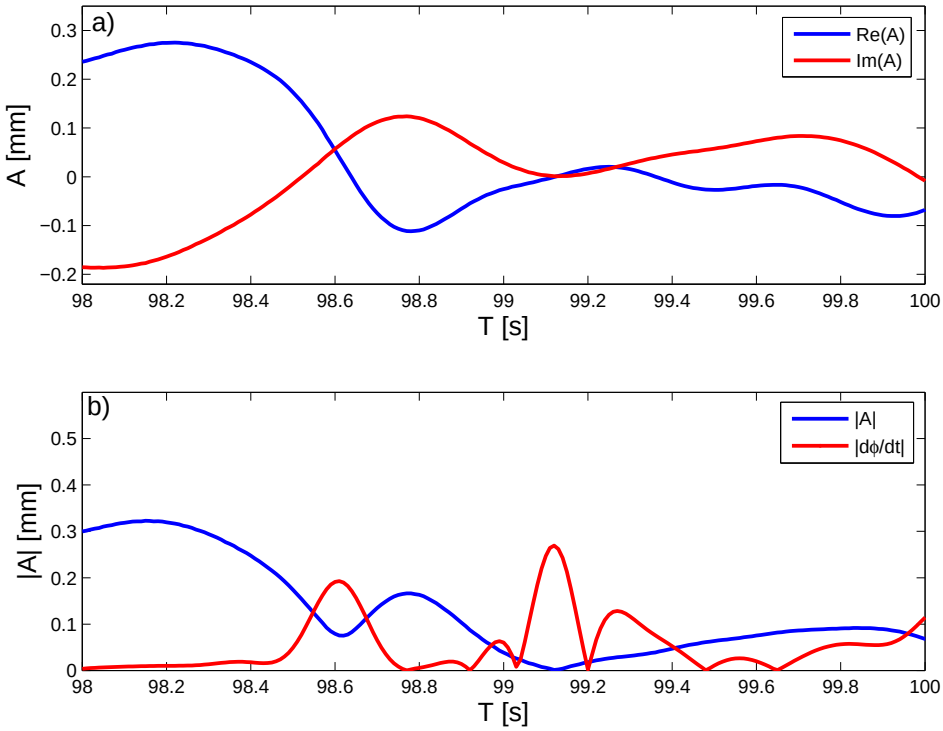

Figure 5.4: a) Temporal traces of the real and imaginary part of $A(t)$ showing the passage of a defect ($Re(A) = Im(A) = 0$). b) Temporal trace of $|A(t)|$, and the corresponding modulus of the phase derivative $|\dot{\phi}(t)|$. In this plot, $|\dot{\phi}(t)|$ has been multiplied by 0.05 to make it visible in the same scale as the amplitude fluctuations.

The points where $Re(A) = Im(A) = 0$ are the points where the phase ϕ is ill-defined and a discontinuity appears. This singularity is removed when it reaches the boundaries of the cell or when it collides with another one, therefore acting as a dynamical mechanism to eliminate fluctuations from the system. There is a strong correlation between the extrema of the phase derivative $\dot{\phi}(t)$ and the points where $|A(t)|$ reaches its minima. The profile of a defect determined with this local measurement technique is asymmetric, due to the intrinsic dynamics of the defect: it passes through the capacitive gauge at non-zero speed, and through its propagation changes the wave pattern by moving the singularity in the phase till it will reach one of the boundaries of the cell or another dislocation, thus vanishing. At this excitation frequency ($f = 60$ Hz), the passage time τ of a defect, i.e., the amount of time the amplitude $|A|$ takes to go from its mean value to zero and back, is of the order of 0.1 s, an order of magnitude smaller than the oscillation period of the amplitude modulation described above ($1/\delta f \sim 1$ s). In this regime, several defects can go through the capacitive gauge, each one with a different velocity arriving from different sides of the container.

The nucleation of a defect is a random event, happening at different places over the pattern. As we increase the control parameter, the time it takes to generate a defect that crosses the capacitive gauge decreases. In this state, we can study the statistical properties of the wave amplitude when this type of singularities control its dynamical evolution.

We show in Fig.(5.5) the probability distribution function (PDF) of the normalized amplitude $|A| \,/\, \langle |A| \rangle$. Close to zero the PDF shuts steeply to zero. This shows that the time of passage of defects is very small, and that they are isolated and singular events. It presents a maximum close to $\langle A \rangle /2$

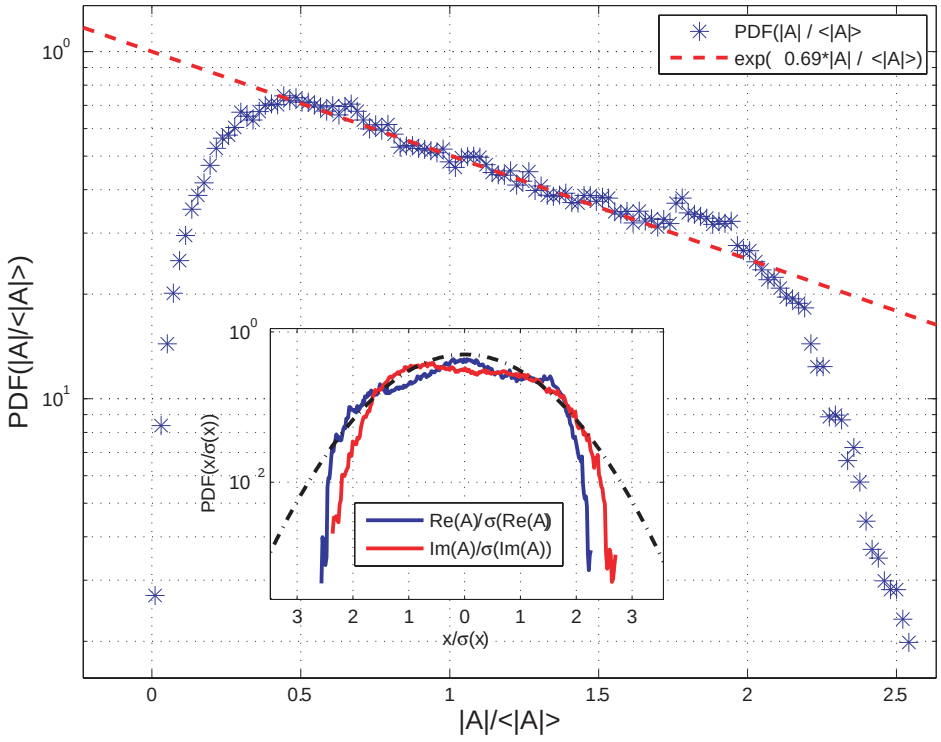

Figure 5.5: PDF of the normalized amplitude fluctuations $|A| \,/\, \langle |A| \rangle$ for $\epsilon = 1.41$ (stars) and an exponential fit (dashed line). Inset: PDF of the normalized real (blue) and imaginary (red) parts of A for $\epsilon = 1.41$. Normalized normal fit in dashed black line as an eye guide. Here, $\langle A \rangle = 0.15$ mm.

and an exponential tail for amplitude fluctuations close to $\langle A \rangle$. For large fluctuations ($|A| \,/\, \langle |A| \rangle > 2$) the PDF goes to zero abruptly, due to the fact that no cusps, burst or ejection of dropplets are seen in the experimental set-up: the wave pattern has still finite amplitude fluctuations. This is in contrast to the statistics of large amplitude events in the complex Ginzburg Landau equation with parametric forcing used to describe parametric waves [5, 6]. The theoretically predicted PDF is long-tailed and extreme fluctuations related to bursts or pulses are possible. Here, the wave pattern cannot explore large ampltiude events without wave breaking through dropplet ejection, which we avoided. Cusps cannot occur because the wavelength of the basic pattern is smaller than the capillary length $\sqrt{\gamma/\rho g} \sim 2$ mm, which prevents the formation of blow-up singularities [17].

The probability distribution functions of both the normalized real $Re(A)/\sigma(Re(A))$ and imaginary $Im(A)/\sigma(Im(A))$ parts of the complex amplitude do not present exponential tails, as we show in the inset in Fig. (5.5). Here $\sigma(x)$ stands for the standard deviation or *rms* fluctuations of the fluctuating variable x. The kurtosis of both variables is close to 2, and a small degree of negative (positive) skweness appears for the real (imaginary) part. Furthermore, the real and imaginary components of A cannot be regarded as independent variables either because the computed correlation coefficient $< Re(A)Im(A) > /\sigma(Re(A))\sigma(Im(A))$ is close to -0.9. This means that a distribution for wave amplitudes such as the Rayleigh distribution $\sim |A|e^{-|A|^2/2}$ [18], that takes into account the probability density function of the modulus of a gaussian variable, cannot fit the experimental PDF of $|A|$, even if the PDF of $Re(A)$ and $Im(A)$ where gaussian due to the large correlation between $Re(A)$ and $Im(A)$.

We focus now on the dynamical description of the fluctuating wave amplitude. The appearence of defects changes the dynamical behavior of the wave pattern amplitude, as we can see from its

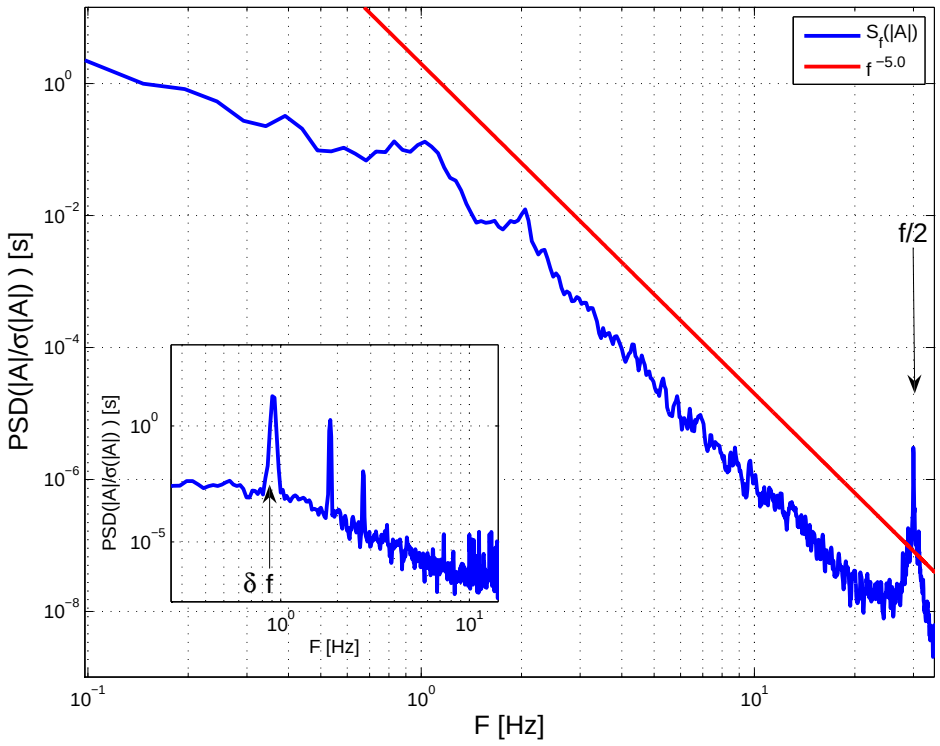

Figure 5.6: PSD of the local wave amplitude $|A|$ for $\epsilon = 1.41$. The slope (in red dashed line) is close to -5.0. Inset: PSD of the local wave amplitude $|A|$ for $\epsilon = 0.84$. The first harmonic peak is at δf =0.87 Hz. Here, the excitation frequency fixed at 60 Hz, the pattern is oscillating at 30 Hz and $\delta f \sim 1$ Hz.

power spectral density (PSD) in Fig.(5.6). In the regime dominated by the secondary oscillatory instabilities (in this case oscillatory instabilities related to the box size), the PSD of the amplitude fluctuations is peaked at δf and its harmonics (see inset of Fig. (5.6)). As ϵ is increased, defects are created in the system and a power-law type of power spectral density for $|A|$ over one decade appears for frequencies larger than δf. The frequency band where this spectrum is observed is larger than $1/\tau \sim 10$ Hz. Therefore, the dynamics of the complex amplitude in presence of defects is responsible for the scale-invariant spectral fluctuations. The computed slope is close to -5.

For smaller frequencies than δf the spectrum displays a power-law behavior $\sim f^{-1}$, related to slow modulations of the large scale wave amplitude. Large acquisitions of the order of a day have been made for this matter in order to resolve up to the mHz. At large frequencies compared to δf a peak at $f/2$ appears with a bandwidth of the order of 10 Hz. It is the harmonic component of the basic pattern that oscillates at f, shifted to $f/2$ due to the phase-sensitive detection. This takes in account the mode coupling between the harmonic and subharmonic components, mediated by the appearence of the imperfections in the wave pattern.

The power-law spectrum does not result from the filtering technique. To test this fact we have changed the order of the Butterworth filter and the time constant of the phase sensitive detection device, but maintainig the dynamical range in order to resolve the power-law spectum. No qualitative nor quantitative change was observed. Also, the PSD cannot be deduced from just the singularities of the derivative of $|A|$ when it aproaches zero. In that case its PSD would be the one of local derivative discontinuities, i.e., f^{-4}. Kuznetzov [19] has proposed several power-law spectra to take into account singularities in surface waves, depending if there are point or line singularities, or if they

propagate at a given velocity. He predicts a power-law spectrum f^{-5} when line singularities ($A = 0$) propagate at constant speed, but in our case the dynamical variable is the modulus of the envelope amplitude $|A|$. Therefore no simple relationship can be made between the experimental result and the theoretical prediction. To wit, we have changed the sampling frequency from 1 to 5 kHz. No substantial difference in the slope has been observed. The resolution of the defect core does not affect the slope of the spectrum either. This is confirmed when the excitation frequency is changed from 60 to 120 Hz to make the wavelength smaller.

These two separate statistical indicators, the PDF and the PSD of the local wave amplitude, show the qualitative change in the behavior of the parametrically excited surface waves when defects dominate their dynamics in a stationary out-of-equilibrium state. Their interaction with the wave pattern mediate the propagation of wave amplitude fluctuations from one place of the container to the other. When ϵ grows larger and larger, more defects will randomly appear over the wave pattern, speeding the propagation of these fluctuations. This out-of-equilibrium stationary state is termed *defect-mediated turbulence*.

We have shown in this section that when a large number of modes in the wave number band $k_c \pm \Delta k$ are parametrically excited, fluctuations of the local wave amplitude are strong enough to break locally the wave pattern and force the wave amplitude to vanish, forming a defect. In this out-of-equilibrium state of the wave system, no control over the wave amplitude fluctuations can be achieved. To study the case where fluctuations of the the parametric surface waves can be controlled, we present the next experimental study.

5.3 Spatio-temporal noise in parametrically excited surface waves

The calculations on the first section consider the case of the deterministic growth of the nonlinearly saturated amplitude when the forcing amplitude is close to its threshold value and no fluctuations are taken into account. A problem of both theoretical and practical interest is how parametric resonance is modified when the pump, i.e., the spatial or temporal modulation, is noisy. Only a handful of experiments have been performed [20, 21, 22, 15] to study such an effect and in each case the fluctuations of the pumping mechanism are temporal. To gain insight on the effect of spatio-temporal fluctuations on these parametrically amplified surface waves, we have developed a source of spatio-temporal noise by means of a periodic Lorentz force [23]. This force, acting on a conducting fluid (in this case, mercury) creates an underlying vortex flow that interacts with the parametrically amplified surface waves.

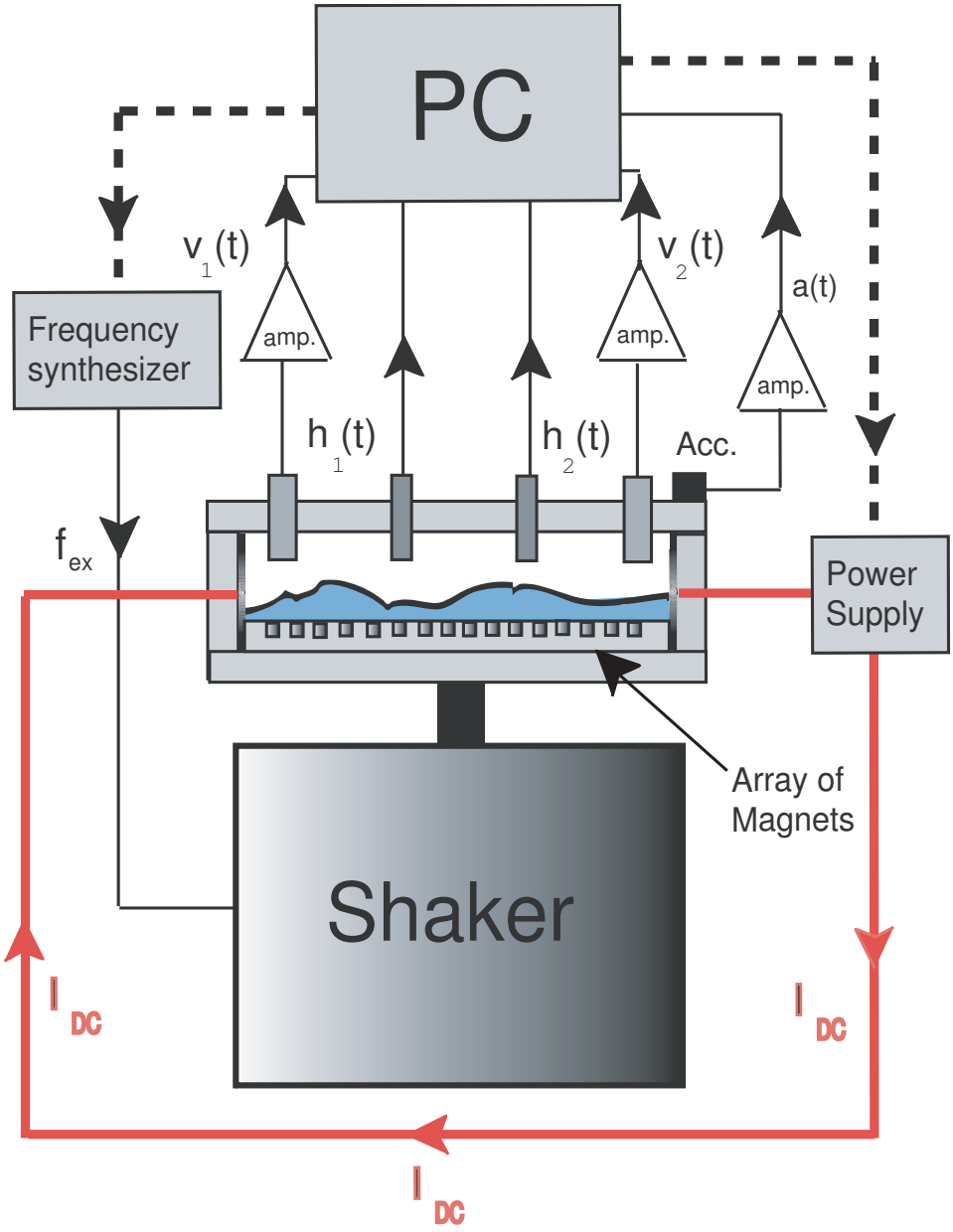

Figure 5.7: Second experimental set-up. Waves at the surface of a mercury layer are parametrically amplified by periodic modulation of gravity which is measured by means of a piezoelectric accelerometer. The local wave amplitude and velocity fields are measured by inductive sensors and potential-difference probes. A constant DC current is imposed to the mercury layer through two copper electrodes which generates a Lorentz force $\mathbf{F}_L$ due to a periodic magnetic field generated by an hexagonal array of magnets of alternating vertical polarity.

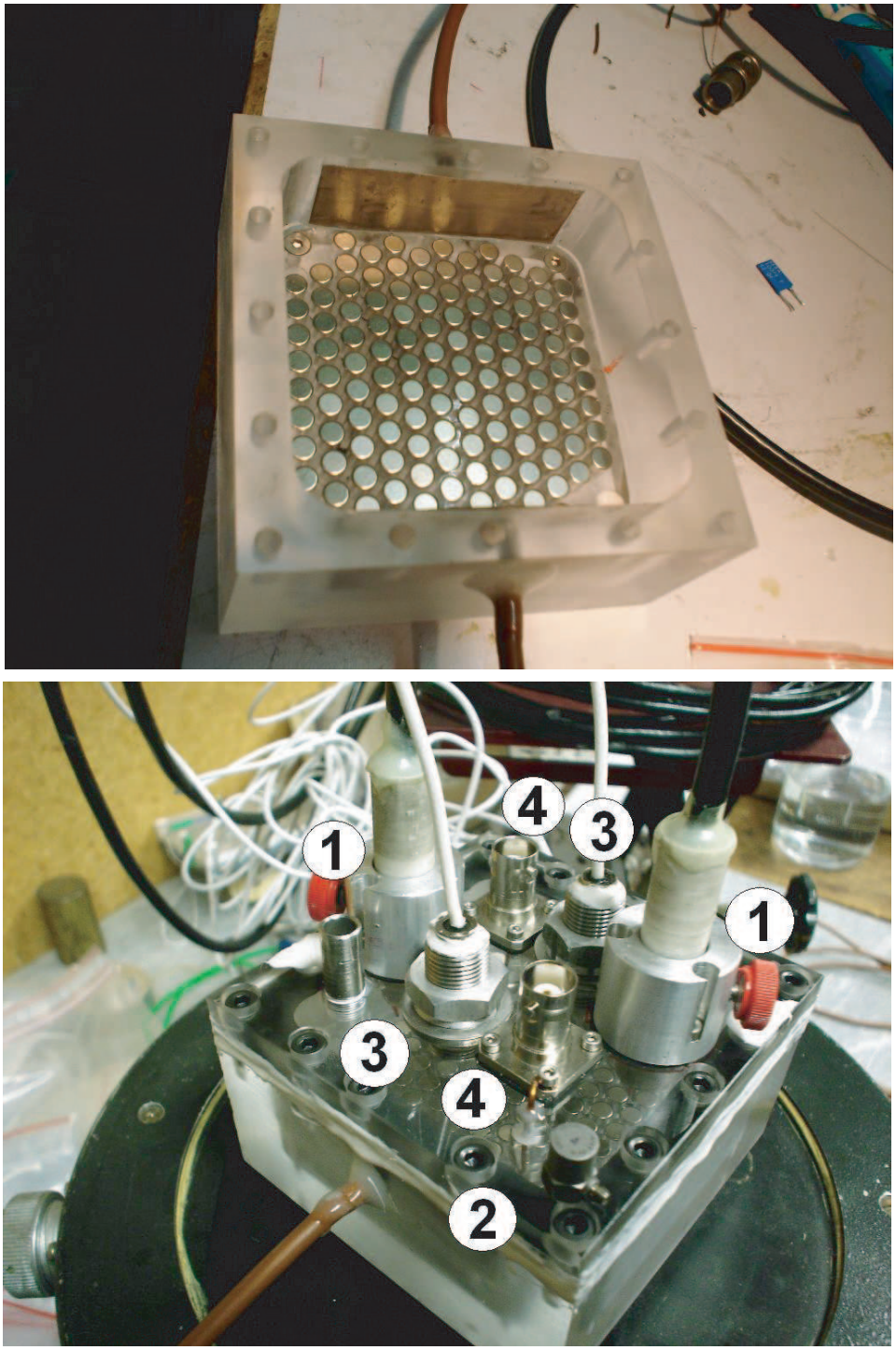

Figure 5.8: Second experimental set-up. **Up:** Bottom of the container, where an array of periodically alternating polarity magnets are positioned in an hexagonal array. On opposite sides of the cell two copper electrodes are used to drive a DC current in the mercury layer. **Bottom:** Mounted container on the electromagnetic shaker, showing the sensors (1) Vivès probes, (2) piezoelectric accelerometer, (3) inductive sensors and (4) capacitive wire gauges.

5.3.1 Experimental set-up and measuring techniques

We describe the second experimental set-up in this section. A schematical picture of the experimenal set-up is displayed in Fig. (5.7). A Plexiglass container of 70 x 70 mm^2 is filled with mercury (density ρ = 13.6 x 10^4 kg/m^3, kinematic viscosity ν= 1.2 x 10^{-7} m^2/s and surface tension σ= 0.4 N/m) up to a height of 5 mm. At the bottom of the cell, alternating vertical polarity magnets (5 mm in diameter) were placed with a 1 mm gap between them on an hexagonal array (6 mm in wavelength), as depicted in Fig. (5.8). The magnetic field strength at the surface of the fluid on top of a magnet is 500 G. Two nickel-barnished copper electrodes were glued at opposite sides of the cell, to be in contact with the mercury layer. A fine layer of nickel was deposited over them to ensure no chemical reaction between mercury and copper. The surface stayed clean of impurities (amalgams of Ni and Hg) for as long as two months. To avoid oxide formation, the surface is kept clean by maintaining the fluid in a nitrogen-filled atmosphere. Through the copper electrodes, a DC current I generated by a power-supply (Agilent E3336A 20 V - 7 A), is applied to the conducting fluid. This gives rise to current density $\mathbf{j}$, and therefore a Lorentz force $\mathbf{F}_L = \mathbf{j} \times \mathbf{B}$. The container is temperature-regulated by circulating water 20.0 $\pm$ 0.1°C by means of a thermal bath (Lauda RC6 Chiller). As in the previous experimental device, an electromagnetic vibration exciter (B & K 4809) driven by a frequency syntheziser (HP 8904 A), provides a clean vertical sinusoidal acceleration (horizontal acceleration less than 1 % of the vertical one). The effective gravity in the reference frame of the container is then $g+acos(2\pi ft)$, where g is the acceleration of gravity, a is proportional to the applied tension V and f is the excitation frequency. The vertical modulation of the acceleration is measured by a piezoelectric accelerometer (B & K 4803) fixed to the vibrating container and a charge amplifier (B & K 2635).

The surface wave amplitude is measured by two inductive sensors (eddy-current linear displacement gauge, Electro 4953 sensors with EMD1053 DC power supply). Both sensors, 3 mm in diameter, are screwed in the Plexiglas plate perpendicularly to the fluid surface at rest. They are put 0.7 mm above the surface. The sensors are located on one of the diagonals of the container, 30 mm away from each other about the center. The measuring mechanism of the eddy (circular)-current linear displacement gauge used to measure the position or displacement of a conducting metal at a distance x relies on electromagnetic induction [24]. Two coils, called primary (or reference) coil and secondary (or sensing) coil, are positioned one over the other without touching. An alternating tension is imposed over the primary at high frequency (the operating range is in between 50 kHz up to 10 MHz). The eddy or circular currents induced in the conducting material produce a magnetic field which opposes the one on the sensing coil. This effect is larger the closer the conducting material is to the sensing coil, due to the fact that the change in the magnetic impedance is larger. Although generally the relationship between the coil impedance and the distance x to the conducting material is nonlinear, for the sensors used in this experiment, the sensing range is linear in very small range of x. The type of inductive sensors used in this experiment is of the shielded type, allowing it to be embedded in a metal socket, as shown in Figs. (5.8) and (5.9). The linear response of these inductive sensors in the case of a wavy liquid metal surface has been checked in a previous study [25]. The linear sensing range of the sensors allows distance measurements from the sensor head to the fluid surface up to 1.27 mm with a 7.9 V/mm sensitivity. A capacitive measurement can be also made, but the sensitiviy of the capacitive wire gauge is orders of magnitudes smaller than the one of the inductive sensors. The greatest advantage of inductive sensors is that they are not perturbative as the capacitive wire gauges. In contrast, the main disadvantage is that inductive sensors average the local fluctuations over 3 mm, which means that fluctuations with length scales that are smaller than 3 mm cannot be resolved. This is the reason why we have chosen the wavelengths in the experimental

set-up larger than 3 mm.

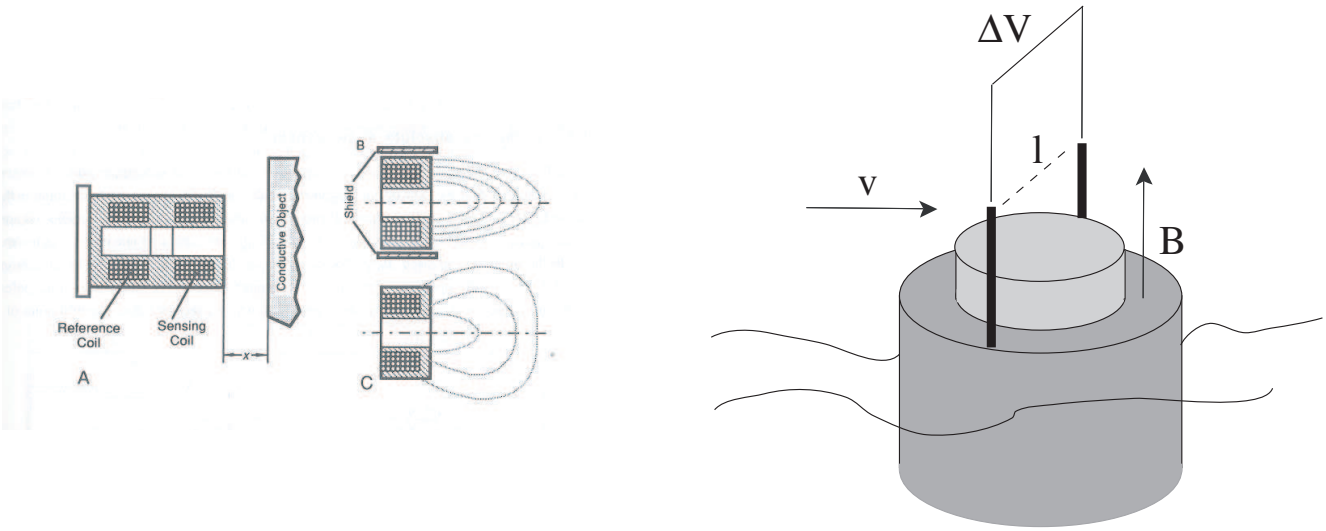

Figure 5.9: **Left:** Schematic view of an inductive sensor. **A** Electromagnetic proximity sensor. **B** Shielded and **C** Unshielded sensor. Figure taken from Fraden[24], p.279. **Right:** Schematic view of a Vivès probe, where the potential difference ΔV averaged over the distance l is proportional to the averaged electric field $\int_l \mathbf{v} \times \mathbf{B} \cdot \mathbf{dl}$.

In addition, the local velocity fluctuations of the flow can also be studied in this experimental configuration. They are measured in two points 20 mm from the closest wall, 35 mm the farthest one and 50 mm away from each other by means of Vivès probes [26]. As shown in Fig. (5.9), these probes are made by two electrodes made of copper and separated by a distance l=3 mm, that plunge 2 mm into the fluid and are isolated completely from the liquid metal, except at the end, where the electrical contact is made. A small cylindrical magnet (5 mm in diameter) is placed 5 mm above the electrodes, generating a magnetic field strength of 500 G at the electrical contact point. The whole system is integrated into a cylindrical rod that is screwed to the Plexiglass plate. The measuring principle relies on Faraday's law of induction. When an element of conducting fluid in presence of a magnetic field **B** passes with velocity **v** in between the wire electrodes, an electric field **e** is generated following

$$\int_l \mathbf{e} \cdot \mathbf{dl} = \int_l \mathbf{v} \times \mathbf{B} \cdot \mathbf{dl},$$

which in turn creates a small tension difference at the end of the wire electrodes. The magnetic field of the magnet in the Viveès probe does not affect the qualitative behavior of the velocity fluctuations of the flow. In this approximation we have not taken into account neither the constant nor the induced currents in the conducting fluid, which can generate also an electric field. The explanation is as follows: the DC component is eliminated by high-pass filtering the potential difference and the induced currents are negligible given the low speed of the vortex flow (low magnetic Reynolds number R_m). For velocity fluctuations of length scales larger than l, the voltage difference measured between the electrodes is proportional to the velocity fluctuations v_1 which are orthogonal to the vertical magnetic field B_0 [27]. A small tension proportional to $v_1 B_0 l$ of the order of a few microvolts is amplified by a factor 10^5 and acquired with the amplitude fluctuations and the acceleration signals. The DC component of the signals are filtered out in the acquisition. This filtering eliminates the problem of constant eddy currents in the inductive sensors and the large DC component in the Vivès probes. To resolve statistically the temporal fluctuations of the measured quantities, the sampling

frequency is fixed at 500 Hz and the acquisition time is set 800 s, much larger than the typical time scales of the acquired signals.

5.3.2 Experimental results

We present in the following section the experimental results of the effect of the spatio-temporal fluctuations due to the underlying vortex flow on the standing surface waves. To do so, we start by describing both cellular flows separately. We start by describing the properties of the local wave amplitude and velocity profile of the parametrically amplified surface waves.

Parametrically amplified surface waves

Subjecting the container to a periodical modulation of gravity, surface waves can be amplified parametrically. These parametric waves respond subharmonically to the modulation. In this experimental configuration the modulation frequency f is fixed and the modulation amplitude a is changed. At a given threshold amplitude a_c, the flat surface becomes unstable to small perturbations and stationary surface waves appear. We observe a square pattern of standing waves without defects.

The choice of the excitation frequency f =23.8 Hz is two-fold: to have no time-dependent amplitude (an eigenmode of the container) and a comparable wavelength to the one of the magnetic field $\mathbf{B}$ ($\lambda = 6$ mm), larger than the diameter of the inductive sensor, which is 3 mm. We have explored a frequency range ($20 < f < 30$ Hz) in which the wavelength of the pattern and the one of the periodic Lorentz force are similar. The wavelength of the parametrically amplified waves is roughly 8 to 10 times smaller that the size of the container. The frequency difference between two successive resonance tongues is about 1 Hz. By tuning the excitation frequency within a 1 Hz interval, it is easy to work in the vicinity of the minimum of a resonance tongue, without detunning between the excitation frequency and the natural oscillation frequency of the surface waves. We show in Fig. (5.10) the bifurcation diagram of the wave amplitude $\langle h_1 \rangle$ of the parametrically amplified surface waves. Its dependence on the reduced control parameter $\epsilon = (a - a_c)/a_c$ is

$$\langle h_1 \rangle \sim \epsilon^{1/4},$$

as reported elsewhere [15].

Given the fact that the surface deformations are generated by the cellular flow in the bulk of the fluid, the velocity field also saturates nonlinearly and can be used to study the threshold of the parametrically amplified waves. To our knowledge, this is the first measurement of the local velocity field in parametrically excited surface waves. The bifurcation diagram of this signal is shown in Fig.(5.11). The nonlinearly saturated velocity field grows as

$$\langle v_1 \rangle \sim \epsilon^{1/2},$$

in contrast to the local amplitude dependence.

Both the local wave amplitude and velocity field present the same threshold value for a_c, showing the growth of one single mode over the container and no distinguishable hysteresis loop is found in the bifurcation diagrams for h_1 and v_1. Increasing ϵ further, more modes are excited. For large ϵ, $\epsilon > 0.5$, the unstable mode is no longer stationary and low-frequency (large-scale) modulations of both fields appear due to secondary instabilites as explained in the previous section.This complex regime was not studied here. To compute the bifurcation diagram of each variable $X(t)$ we have used

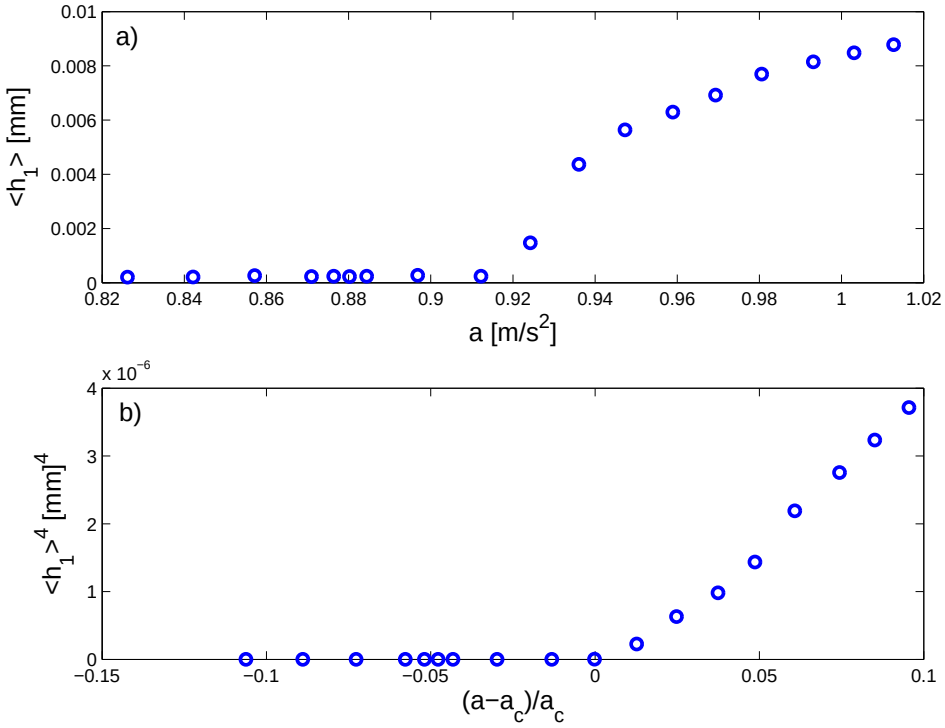

Figure 5.10: (a) Bifurcation diagram for the wave amplitude $\langle h_1 \rangle$ as a function of a. (b) Bifurcation diagram for $\langle h_1 \rangle^4$ as a function of $\epsilon = (a - a_c)/a_c$.

the Fourier coefficients at $f/2$ of the signals, by taking

$$\widehat{X}(\omega = \pi f) = \lim_{T \to \infty} \left| \frac{1}{2} \int_{-T}^{T} X(t) e^{\pi i f t} dt \right|,$$

where T is the acquisition time, much larger than the oscillation period π/f ($Tf \sim 10^4$). This proccedure is simply a phase-sensitive detection of the Fourier component at the oscillation frequency $f/2$.

This weakly nonlinear regime, with a stationary nonlinearly saturated standing wave, will be studied when fluctuations in space and time are added to the wave system, through an underlying vortex flow.

Vortex flow

We investigate now the effect of the periodic Lorentz force $\mathbf{F}_L$ on the surface and in-bulk fields. The mechanism of the formation of the flow is the following: when a constant current I is applied through the liquid metal in the presence of a periodic magnetic field $\mathbf{B}$, a periodic Lorentz force $\mathbf{F}_L = \mathbf{j} \times \mathbf{B}$ sets the fluid in motion. In this experimental setup up, given the fact that the waves at the interface have very small amplitude with respect to the depth of the mercury layer, the density current $\mathbf{j}$ can be estimated as $\mathbf{j} = (I/S)\mathbf{e}$, where S=3.5 cm^2 is the surface crossed by the current and $\mathbf{e}$ is a unitary vector pointing normally from one electrode (the cathode) to the other one (the anode).

The velocity field $\mathbf{v}$ of the flow can be estimated balancing the Lorentz force $\mathbf{F}_L$ that works as the motor of the motion of the fluid and the convective acceleration $\rho(\mathbf{v} \cdot \bigtriangledown)\mathbf{v}$ in the Navier-Stokes

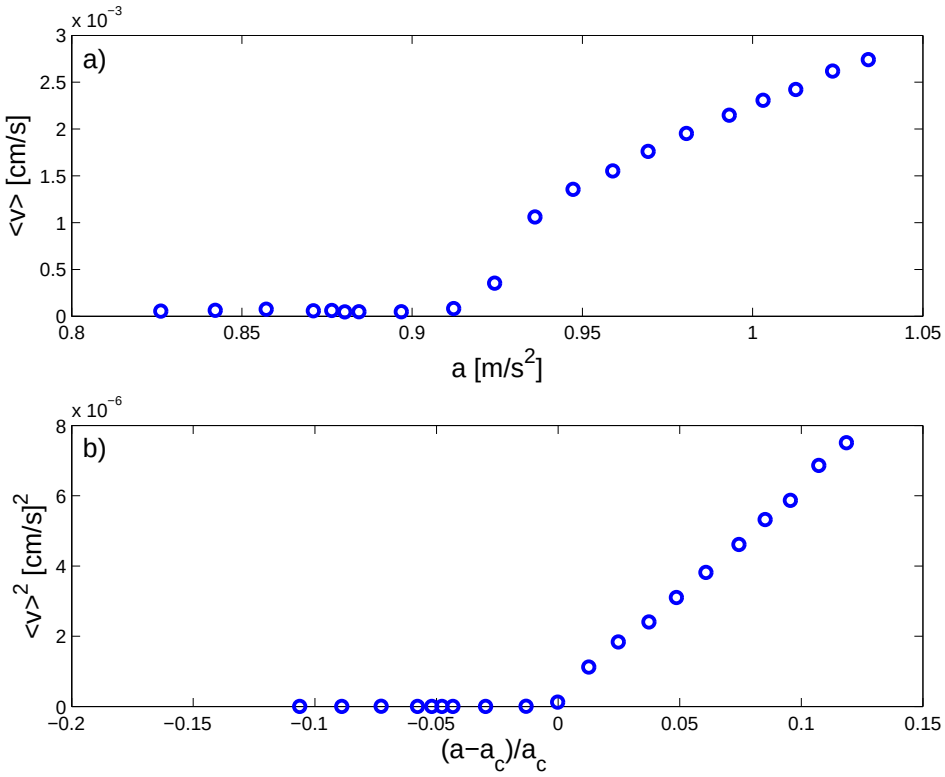

Figure 5.11: (a) Bifurcation diagram for the velocity field $\langle v_1 \rangle$ as a function of a. (b) Bifurcation diagram for $\langle v_1 \rangle^2$ as a function of $\epsilon = (a - a_c)/a_c$.

equation

$$\rho \left(\frac{\partial \mathbf{v}}{\partial t} + (\mathbf{v} \cdot \bigtriangledown)\mathbf{v} \right) = - \bigtriangledown p + \rho \nu \bigtriangleup \mathbf{v} + \mathbf{F_L},$$

where ρ is the fluid density and ν its kinematic viscosity. The order of magnitude for such velocity fluctuations at the forcing scale (the magnetic field wavelength λ) for a typical DC current $I \sim 1$ A is 5 cm/s and the Reynolds Number Re is of the order of 100. Even at low Re, the velocity field creates deformations on the free surface. Both surface and in-bulk fluctuations present large amplitude events and low-frequency fluctuations, as it is shown in Fig. (5.12). We study in the next paragraphs their statistical properties.

Probability density functions : To study the statistical properties of the local response of the fluid to the periodic Lorentz force, we compute the probability density function (PDF) of both the local surface amplitude given by one of the inductive sensors h_1 and the velocity field fluctuations given by one of the Vivès probes v_1. The other two sensors display similar behaviors. For the acquired signals, at a given value of the DC current I, we show their computed PDFs in Figs. (5.13) and (5.14). Increasing the value of I, larger and larger events in local height and velocity occur. The standard deviation or *rms* value of local surface fluctuations $\sigma(h_1)$ increases with increasing current, as do the *rms* of the velocity fluctuations $\sigma(v_1)$. The growth rate is linear in I for the latter and a small departure from linearity is measured in the former (left inset in Figs. (5.13) and (5.14)).

When plotted in the rescaled variables $h_1/\sigma(h_1)$ and $v_1/\sigma(v_1)$, all the PDFs collapse on one curve (see right inset in Figs. (5.13) and (5.14)). No clear asymmetry is found in the normalized PDFs of both variables. A slight departure from the statistics of a normal variable was observed in both

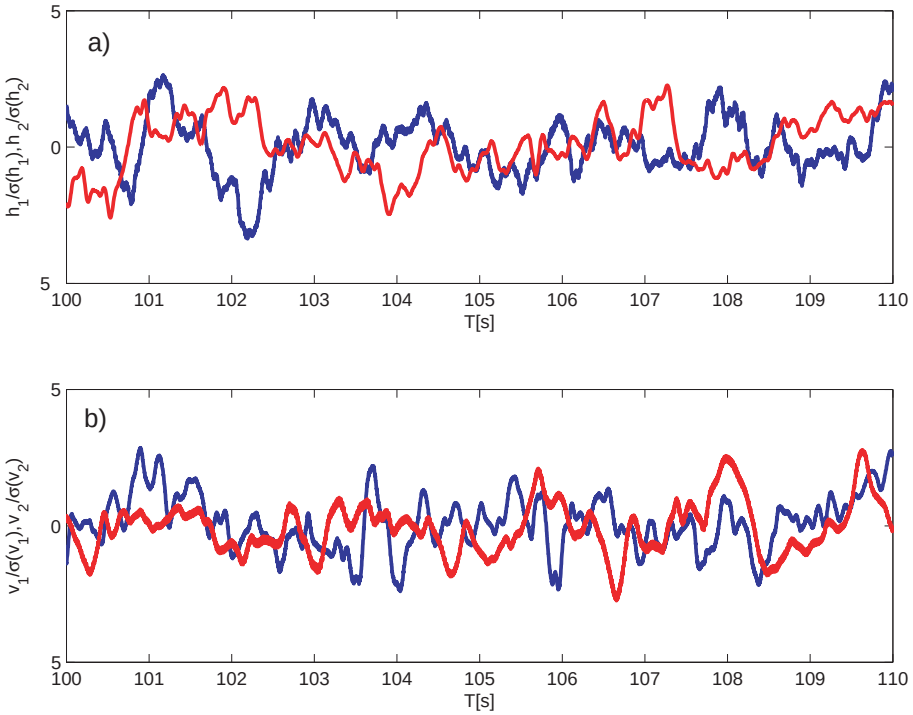

Figure 5.12: Typical traces of the the normalized local amplitude ($h_1/\sigma(h_1)$ and $h_2\sigma(h_2)$) and velocity ($v_1\sigma(v_1)$ and $v_2/\sigma(v_2)$) for I=5 A. Here $\sigma(h_1)$ =0.04 mm and $\sigma(v_1)$ =8 cm/s

signals (the computed kurtosis is 3.2), but not large enough to discard gaussianity.

Contrary to the case of a nonlinearly saturated amplitude, these fluctuations are statistically independent. We can corroborate this fact by measuring their normalized covariance

$$\rho_{h_1 v_1} = \langle h_1 v_1 \rangle / \sqrt{\langle h_1^2 \rangle \langle v_1^2 \rangle},$$

where $\langle\rangle$ stands for time average. This coefficient relates the degree of statistical independence of one variable to the other. We show in Fig. (5.15) the evolution of this statistical indicator as a function of I for different pairs of observables. Increasing I, increases the normalized covariance of the local wave amplitude measured at two different points (h_1 and h_2) from 0.1 at 1 A till 0.25 at 8 A. In contrast, the normalized covariance for v_1 and v_2 fluctuates slighlty arround 0.1 for any value of I, as it is also observed for the pair v_1 and h_1. In that sense, the vortex flow creates locally independent surface and in-bulk fluctuations over the container.

Power spectral densities : As I is increased, low-frequency fluctuations dominate the response of the fluid motion due to the Lorentz force. This can be seen in the power spectral densities (PSD) of both the local amplitude h_1 and velocity field v_1, as shown in Fig. 5.16. For the amplitude fluctuations, the spectra display an exponential behavior and no power-laws for the PSD are found, even for large values of I. In the case of the velocity field, the spectra are not exponential and it follows a power-law close to -5/3. This corroborates the fact that even at the low Re values achieved in this experimental set-up, the flow remains highly fluctuating and chaotic.

When I is less than 1 A, there are clear peaks related to the lower normal modes of the container, acting as cavity modes for the excited surface waves generated by large amplitude fluctuations. At

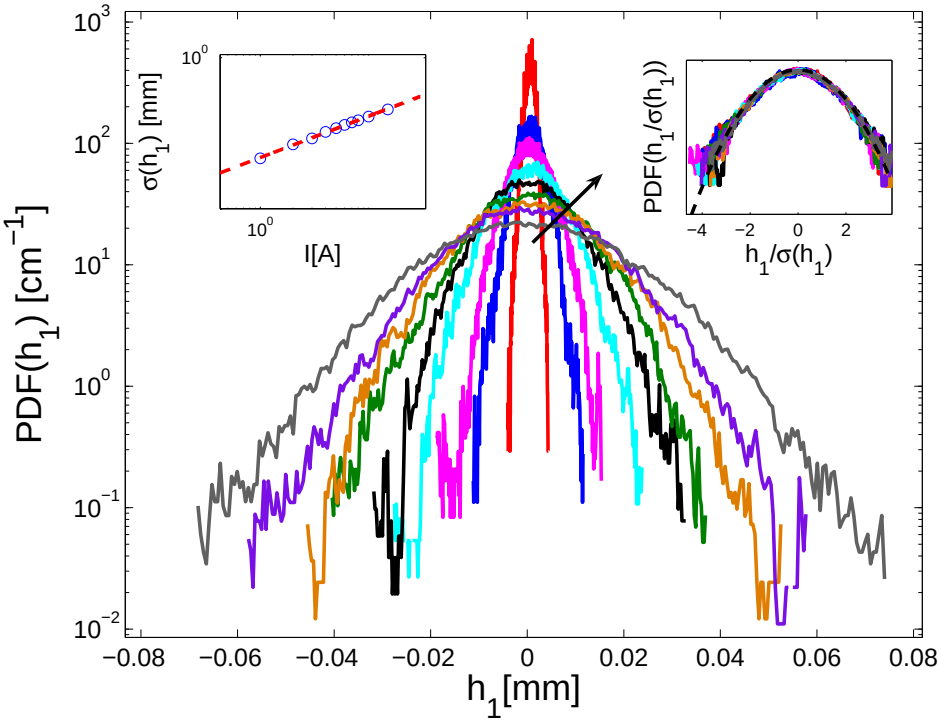

Figure 5.13: Probability density functions of the local amplitude fluctuations h_1 for different values of the current intensity I between 1 and 10 A. The arrow shows the sense of increasing current. Left Inset: Loglog plot $\sigma(h_1)$ as a function of the current intensity I. Best fit slope is 1.2. Right Inset: Probability density functions of the rescaled local amplitude fluctuations $h_1/\sigma(h_1)$ for different values of the current intensity I between 1 and 10 A. In dashed, Gaussian fit.

higher values of I, this coherent response is lost. Rescaling the frequency by the typical turn-over time of the vortex $\lambda/\sigma(v_1) \sim 0.1$ s and the PSDs of the normalized variables $h_1/\sigma(h_1)$ and $v_1/\sigma(v_1)$ by its inverse frequency, we can try to collapse all data on one single curve, as shown in Fig.(5.17). For the local wave amplitude fluctuations, in the explored current range (1 A $< I <$ 10 A), there is a large dispersion for small values of I, due to the strong persistance of the cavity modes. As stated above, this coherent response is lost once the forcing is large enough ($I \sim$ 5A). On the other hand, all data for the velocity spectra can be collapsed on one single curve.

Parametric surface waves in the presence of spatio-temporal noise: vortex flow effect

Let us now study the effect of the periodic Lorentz force $\mathbf{F}_L$ on the growth, saturation and statistics of parametrically forced surface waves. The wavelength of the standing wave pattern is chosen to be of the same order of magnitude as the one of periodic vortex flow, forced at wavelength λ =6 mm. This is done to maximize the effect of the vortex flow fluctuations over the global stationary mode. Therefore, for moderate values of I, the electromagnetically forced vortex flow can be seen as a source of spatio-temporal noise on the standing surface waves. In presence of the vortex flow, the local wave amplitude and velocity field of the surface waves fluctuate strongly as shown in Fig. (5.18). The subharmonic response of both fields decreases as I is increased, till it is lost completely, as we will show below.

The low-frequency and large amplitude fluctuations related to the vortex flow described above persist when the modulation of the gravity is switched on and interact with the small scale cellular

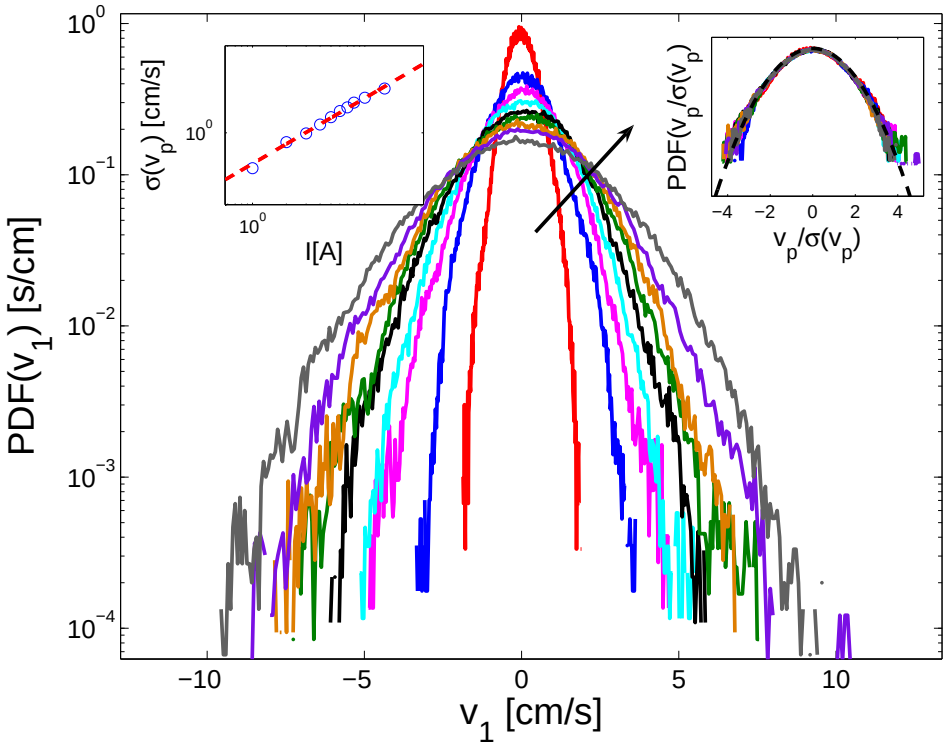

Figure 5.14: Probability density functions of the local velocity fluctuations v_p for different values of the current intensity I between 1 and 10 A. The arrow shows the sense of increasing current. Left Inset: Loglog$\sigma(v_1)$ as a function of the current intensity I. Best fit slope is 1.0. Right Inset: Probability density functions of the rescaled local velocity fluctuations $v_1/\sigma(v_1)$ for different values of the current intensity I between 1 and 10 A. In dashed, Gaussian fit.

flow of the Faraday waves, as we can see from the PSDs of the variables h_1 and v_1 shown in Figs.(5.19) and (5.20), respectively. As the forcing increases, the low frecuencies of the spectra dominate and the subharmonic response decreases. This interaction between the parametrically excited waves and the vortex flow also modulates the amplitude of the subharmonic response, increasing the growth of the bandwidth around $f/2$, as shown in the insets of Figs.(5.19) and (5.20), till the subharmonic response dissapears under the noise level of the fluctutations generated by the Lorentz force.

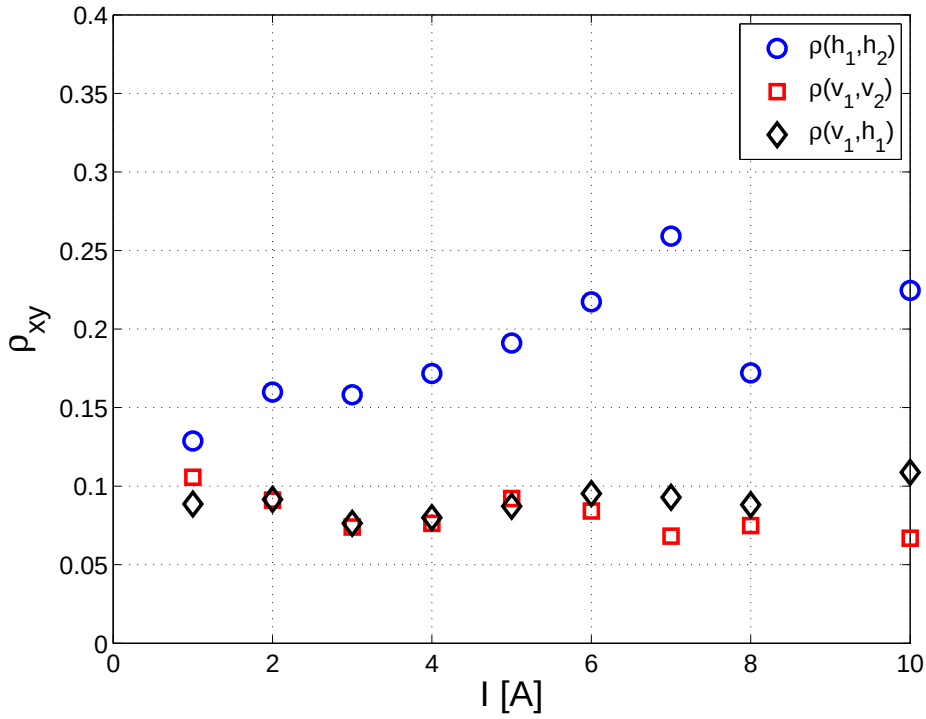

Figure 5.15: Normalized covariance ρ_{xy} as a function of I for h_1, h_2 ($\circ$), v_1, v_2 ($\square$) and h_1, v_1 ($\diamond$).

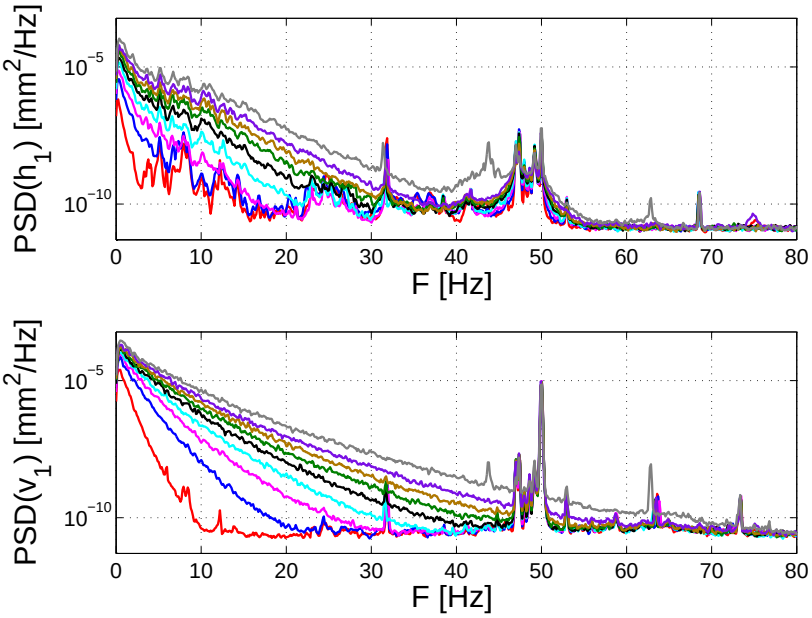

Figure 5.16: (a) Power spectral density (PSD) of the local wave amplitude fluctuations h_1 for different values of the current intensity I between 1 and 10 A as a function of the frequency F. (b) Power spectral density the local velocity field fluctuations v_1 for different values of the current intensity I between 1 and 10 A as a function of the frequency F.

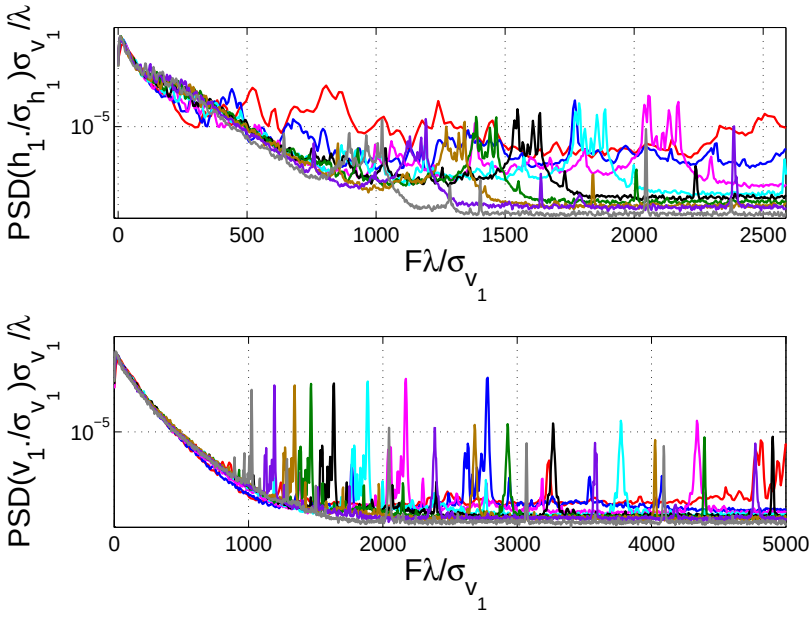

Figure 5.17: (a) Power spectral density (PSD) rescaled by a time constant $\sigma(v_1)/\lambda$ of the normalized local wave amplitude fluctuations $h_1/\sigma(h_1)$ for different values of the current intensity I between 1 and 10 A as a function of the normalized frequency $F\lambda/\sigma(v_1)$. (b) Power spectral density rescaled by a time constant $\sigma(v_1)/\lambda$ of the normalized local velocity field fluctuations $v_1/\sigma(v_1)$ for different values of the current intensity I between 1 and 10 A as a function of the normalized frequency $F\lambda/\sigma(v_1)$.

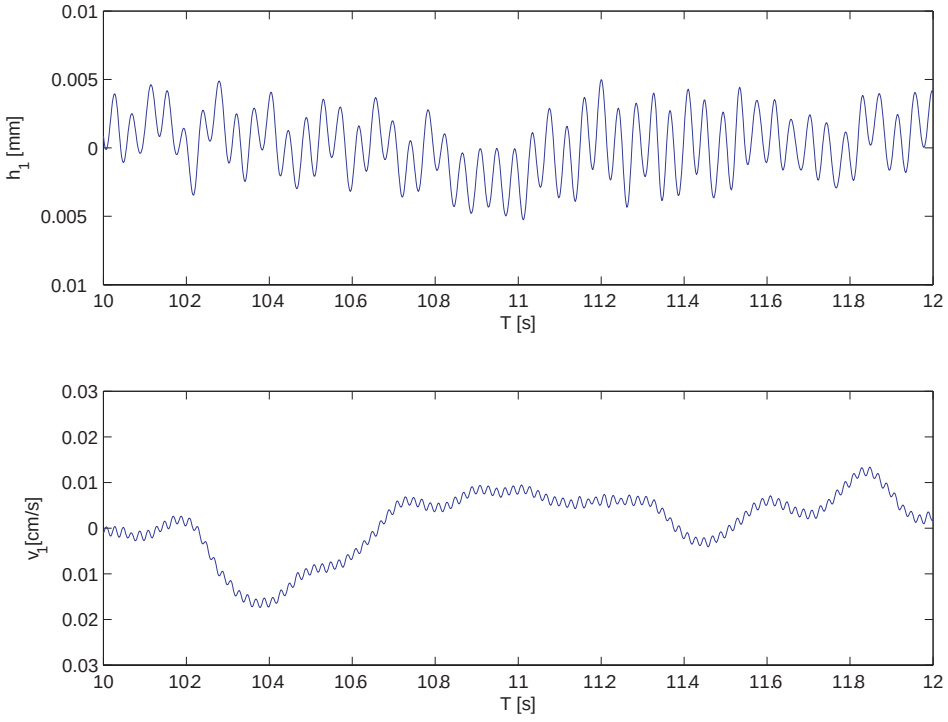

Figure 5.18: Typical traces of the the local amplitude h_1 and velocity v_1 when the subharmonic response is set to I=1 A. We observe the subharmonic oscillation and a superimposed large low-frequency fluctuation in both fields. The excitation frequency is 23.8 Hz.

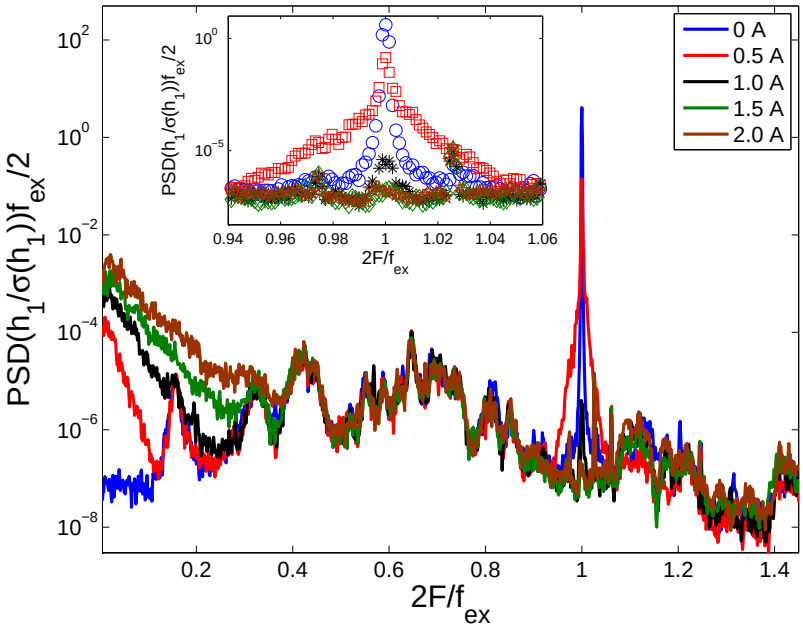

Figure 5.19: Power spectral density (PSD) of the normalized local wave amplitude fluctuations $h_1/\sigma(h_1)$ for different values of the current intensity $I = 0$ to 2 A as a function of the normalized frequency $2F/f$ for a given value of $a > a_c$. Inset: Frequency window focused on the resonance peak of the parametrically excited response for $I = 0.0$ ($\circ$), 0.5 ($\square$), 1.0 ($*$), 1.5 ($\diamond$) and 2.0 ($\star$) A. The excitation frequency is 23.8 Hz.

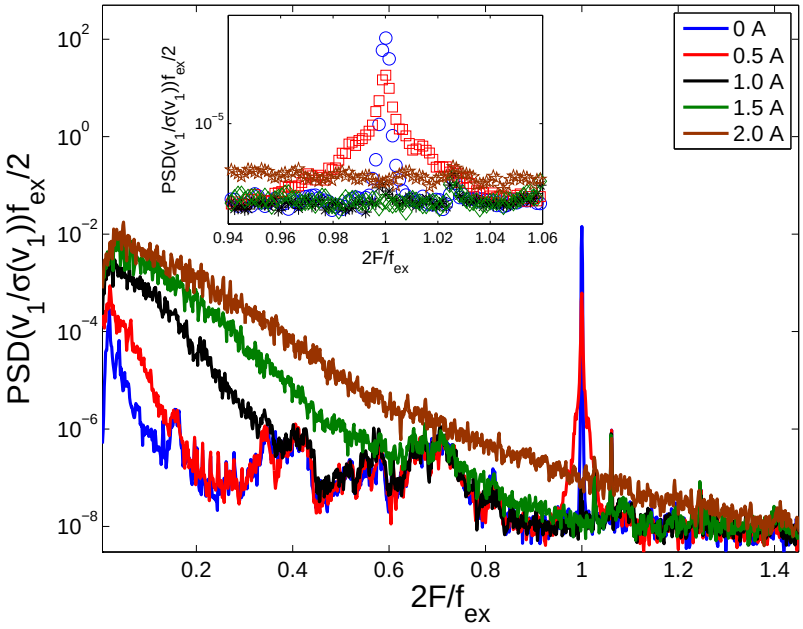

Figure 5.20: Power spectral density PSD the normalized local velocity field fluctuations $v_1/\sigma(v_1)$ for different values of the current intensity $I = 0$ to 2 A as a function of the normalized frequency $2F/f$ for a given value of $a > a_c$. Inset: Frequency window focused on the resonance peak of the parametrically excited response for $I = 0.0$ ($\circ$), 0.5 ($\square$), 1.0 ($*$), 1.5 ($\diamond$) and 2.0 ($\star$) A. The excitation frequency is 23.8 Hz.

When the current I is increased, the critical acceleration threshold $a_c(I)$ of the subharmonic response, shifts to higher values as shown in the bifurcation diagram of local wave amplitude (Fig. (5.21)) and velocity (Fig.(5.22)) fluctuations. As done before, we use the Fourier coefficients at $f/2$ to compute the bifurcation diagrams. No distinguishable hysteresis loop is found in the bifurcation diagrams for both fields. The corresponding critical value of $a_c(I)$ is the same for both the subharmonic local wave amplitude and velocity responses, showing that the parametrically amplified waves develope over the whole container. At a given value of $\epsilon(I) = (a - a_c(I))/a_c(I)$, the local wave amplitude increases with the current. This is due to the large values of $a_c(I)/a_c(0)$. Locally, fluctuations of the vortex flow can be small enough to let the surface waves explore large amplitude events. This is not the case of the local velocity fluctuations, where the nonlinealy saturated velocity field remains of the same order as before. The dependence on the dimensionless parameter $\epsilon(I)$ for the nonlinearly saturated fields continues to hold on average: $(\epsilon(I)^{1/4}$ for the local wave amplitude and $\epsilon(I)^{1/2}$ for the velocity field), although there is a large dispersion on the rescaled bifurcation diagram.

Now, we describe from these measurements the effect of the underlying vortex flow on the growth of the parametrically amplified surface waves. One clear effect is that the local pattern losses its coherence when we increase the flow intensity. We show in Fig. (5.23)a the normalized covariance for the subharmonic response of the wave amplitude and velocity fields. Increasing I for a given value of $a > a_c(0)$, (the parametric waves are indeed present) decreases the normalized covariance of the subharmonic response, decorrelating the fields at different places in the container. This effect is stronger between the local amplitude and the velocity fields. In that sense, the vortex flow breaks locally the pattern structure.

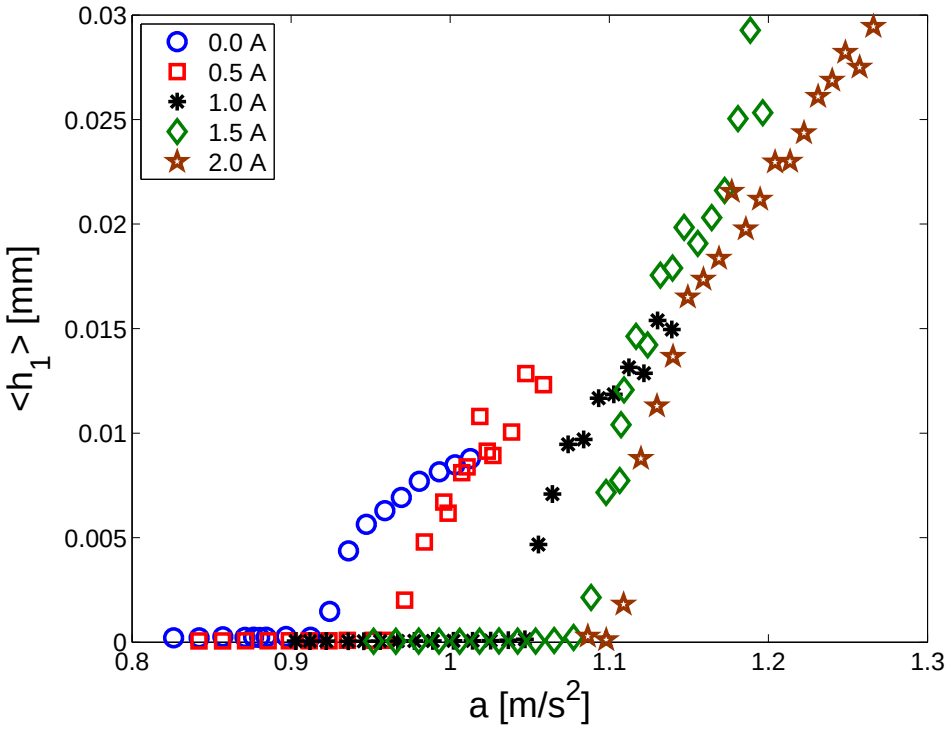

Figure 5.21: Bifurcation diagram of the local wave amplitude of the subharmonic response for $I =$ 0.0 ($\circ$), 0.5 ($\square$), 1.0 ($*$), 1.5 ($\diamond$) and 2.0 ($\star$) A. the excitation frequency 23.8 Hz.

To further prove this point, we calculate the spectral coherence magnitude

$$C_{\widehat{x}\widehat{y}}(f) = |\langle \widehat{x}(f)\widehat{y}(f)\rangle| / \sqrt{|\widehat{x}(f)|^2 |\widehat{y}(f)|^2},$$

where $\widehat{x}(f)$ and $\widehat{y}(f)$ stand for the Fourier transforms of x and y at frequency f. This coefficient relates the possibility of two waves to produce interference between them at a given frequency. In this case we choose that frequency to be the one of the subharmonic response. We show its dependence on I in Fig. 5.23b. As in the case of the normalized covariance, increasing I for a given value of $a > a_c(0)$ decreases the spectral coherence of the subharmonic response till it reaches zero. In that sense, the vortex flow prevents the wave to maintain its structure over the whole container.

These two indicators relate the degree of statistical dependence of two fluctuating quantities (in this case local amplitude and velocity fluctuations). Taking into account the previous measurements and the fact that both the normalized covariance and spectral coherence magnitude are decreased when the vortex flow intensity is increased, we can think of this type of forcing as a spatio-temporal noise on the set of parametrically excited surface waves.

The last part of this experimental study is devoted to the effect of these spatio-temporal fluctuations on the instability threshold value. From the bifurcation diagrams of the local wave amplitude and velocity field, we compute the threshold value $a_c(I)$ as a function of I in the range [0,2] A, as shown in Fig. (5.24). The variable $(a_c(I) - a_c(0))/a_c(0)$ increases roughly linearly with I. From this curve we can see that the threshold value of the subharmonic waves can be shifted by 20 % for I =2 A, with a rather small value of the vortex flow intensity ($\sigma(v_1) \sim 5$ cm/s). This large change in the instability onset means that we cannot see the change of the threshold value just as a renormalization of the eigenfrequency of the waves due to noise effects solely, but also as the appearence of an effective viscosity that grows with I as the underlying flow increases. We do not attempt to

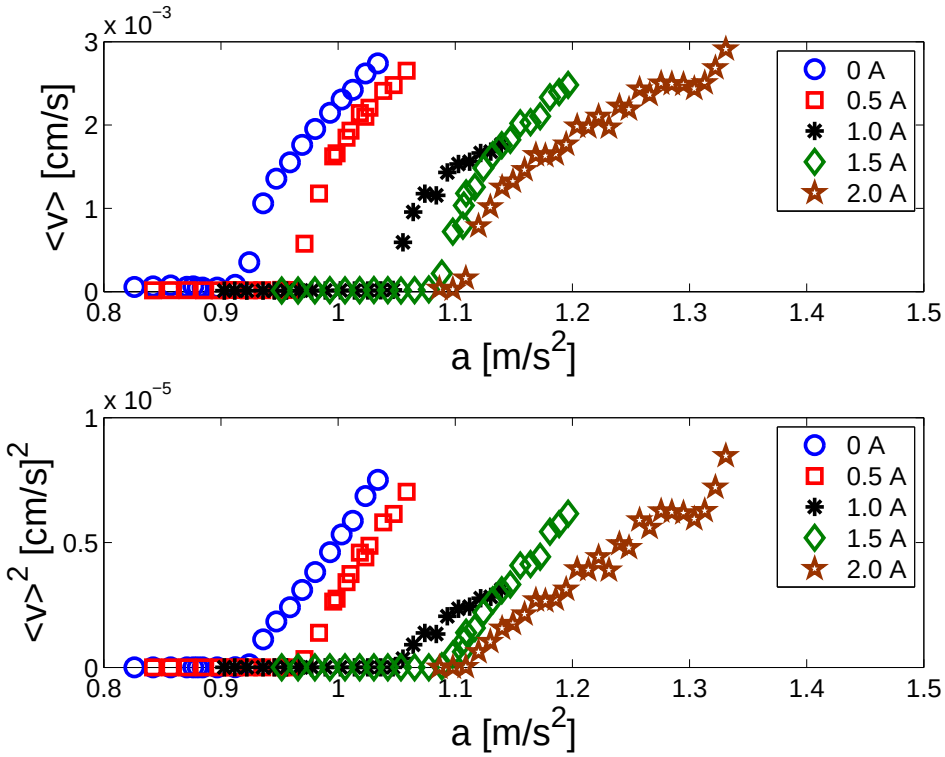

Figure 5.22: (a) Bifurcation diagram of the local velocity field of the subharmonic response for $I =$ 0.0 ($\circ$), 0.5 ($\square$), 1.0 ($*$), 1.5 ($\diamond$) and 2.0 ($\star$) A. (b) (a) Bifurcation diagram of the square of the local velocity field of the subharmonic response for $I = 0.0$ ($\circ$), 0.5 ($\square$), 1.0 ($*$), 1.5 ($\diamond$) and 2.0 ($\star$) A. The excitation frequency is 23.8 Hz.

increase farther the value of I. This will make the vortex flow fluctuations comparable to the largest peak value of the Fourier amplitude of the subharmonic response, i.e., it cannot be viewed as noisy spatio-temporal fluctuation of the cellular flow, as we can see from the insets of Figs. (5.19) and (5.20). This restriction avoids the exploration of larger values of I.

5.4 Conclusions

In this chapter we have presented two separate experimental studies of out-of-equilibrium states where stationary surface waves non-linearly interact among themselves or with a vortex flow. In the first experiment, a defect-mediated turbulent regime has been studied. The statistical properties of the local amplitude of the stationary parametric waves through their PDF and PSD have been studied. The probability density function of the local wave amplitude reveals no long-tailed distribution for large fluctuations. It decreases strongly to zero for $|A| > 2\langle|A|\rangle$, showing the finite character of the amplitude fluctuations. The power spectral density of these fluctuations displays a power-law with an exponent close to -5 for frequencies in between δf (the secondary oscillatory instability frequency) and $f/2$ (the basic pattern oscillation frequency) over one decade. This scale-invariant behavior is interpreted as the signature of defect-mediated turbulence in the wave system when these singularities start to dominate the amplitude dynamics. Although corroboration of this fact was made by mere optical observation with a stroboscopic light driven at $f/2$, spatial Fourier analysis should be performed in order to study experimentally the long-range interaction of defects in this

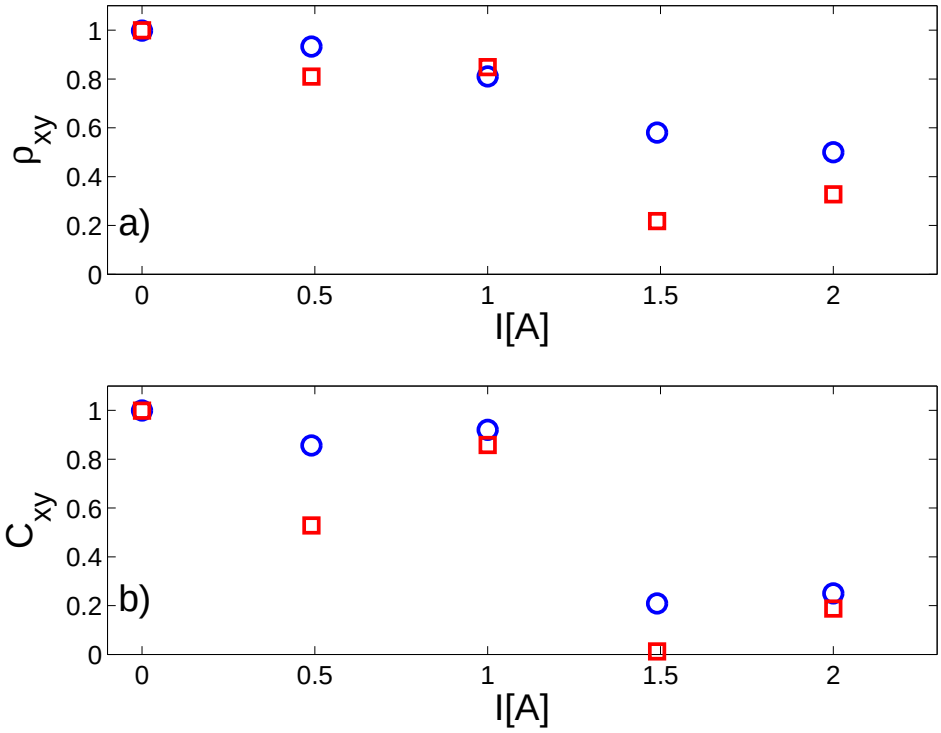

Figure 5.23: (a) Normalized covariance ρ_{xy} as a function of I for h_1, h_2 ($\circ$) and h_1, v_1 ($\square$). (b) Spectral coherence magnitude C_{xy} as a function of I for h_1, h_2 ($\circ$) and h_1, v_1 ($\square$).

type of systems.

In the second experiment, we have studied the effect of a vortex flow on the fluctuations of the local wave amplitude and velocity field of a set of parametrically excited surface waves at a fluid surface. The vortex flow is generated by a periodic Lorentz force $\mathbf{F}_L = \mathbf{j} \times \mathbf{B}$ in the bulk of a liquid metal (mercury). When the sole excitation is the parametric pumping, the standing wave pattern developes and stationary surface waves appear over the fluid surface. When the sole excitation of the fluid motion is the vortex flow, the statistical properties of the surface waves were studied separatetly. The PDFs of local wave amplitude h_1 and velocity field v_1 are roughly normal with their standard deviations growing linearly with the strength of the flow. The PSDs of the temporal fluctuations of the wave amplitude are found to be exponential and the PSD of the velocity fluctuations display a power-law. Also, the normalized covariance between the acquired signals was computed as a function of I, staying always below 0.2. This means that the correlation length of the forcing (vortex flow) is much smaller than the size of the container (which is comparable to the correlation length of the pattern structure). As a remark, these measurements indicate that this type of forcing cannot generate coherent waves and therefore phenomena such as propagation of wave trains or wave turbulence may not be displayed in the presence of an underlying flow.

Later, we have shown experimentally that the vortex flow can act as a source of spatio-temporal noise on a parametrically excited set of waves at a fluid surface. Its presence decorrelates the surface waves over the container. Indeed, the normalized covariance ρ_{xy} and spectral coherence magnitude C_{xy} at the subhamonic frequency $f/2$ decrease strongly in presence of the underlying flow as I is increased. The main effect of the vortex-wave interaction is the growth of the threshold of the parametric instability. The large growth of parametric instability onset cannot be accounted solely by the nonlinear change in the eigenfrequency of the standing pattern due to the nonlinear coupling

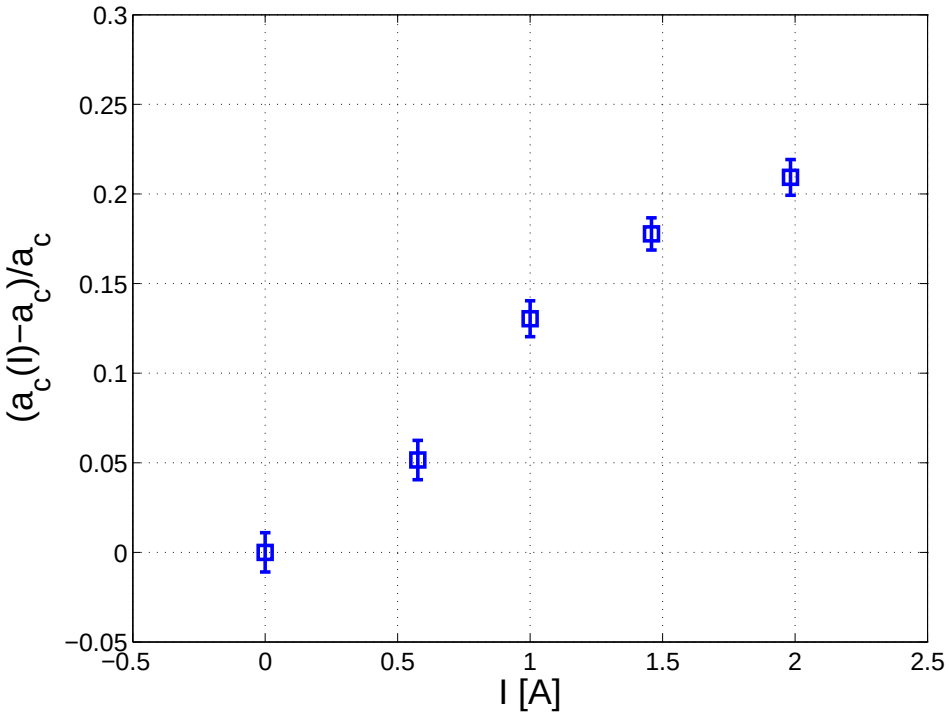

Figure 5.24: Normalized threshold growth $(a_c(I) - a_c)/a_c$ as a function of I ($\square$).

with the flow. Therefore, to increase the threshold, the vortex flow mean effect is to increase the effective viscosity the surface waves perceive. It also modulates the amplitude of the subharmonic response, making h_1 and v_1 fluctuating quantities.

Bibliography

[1] M. Faraday, Phlios. Trans. R. Soc. London **121**, 319 (1831). See also A. Kudrolli, M.C. Abraham and J.P Gollub, Phys. Rev. E **63**, 026208 (2001), S. Douady, J. Fluid Mec. **221**, pp.383-409 (1990)

[2] Mathieu, E., *Journal des Mathématiques Pures et Appliquées*, pp. 137203 (1868)

[3] See for instance S. Fauve, *Dynamics of Nonlinear and Disordered Systems* edited by G. Martiniez-meckler and T. H. Seligman, World Scientific Seres on Nonlinear Science Vol. B6 (World Scientific, Singapore, 1995), pp. 67-115

[4] T. B. Benjamin and F. Ursell, Proc. R. Soc. London A **225**, 505 (1954)

[5] S. Douady, *Instabilité paramétrique d'ondes de surface*, Thèse, ENS Lyon (1989) (unpublished)

[6] I. Aronson, L. Kramer, Rev. Mod. Phys. **74**, 99 - 143 (2002)

[7] S. Douady, S. Fauve and O. Thual, J. Phys. II **1**, p.311-322 (1991)

[8] S. Douady, S. Fauve and O. Thual, Europhys. Lett. **10**, pp. 309-315 (1989)

[9] M.C. Cross and P.C. Hohenberg, Rev. Mod. Phys **65**, 851 (1993)

[10] P. Manneville, *Instabilités, Chaos et Turbulence*, Les Editions de lEcole Polytechnique (2004)

[11] B. Shraiman, Phys. Rev. Lett. **57**, 325 (1986); M. Bertram and A. S. Mikhailov, Phys. Rev. E **67**, 036207 (2003); J. T. Medeiros and A. S. Simões, Phys. Rev. E **64**, 057301 (2001); M/I/ Rabinovich, V.P. Reutov, A.V. Rogalski, Phys. Lett. A **144**, pp. 259-264 (1990)

[12] P. Coullet and E. Elphick, Phys. Lett. A **121** 233 (1987); P. Coullet and J. Lega, Europhys. Lett. **7**, 511 (1988); H. Chaté and B. Nicolaencko, *New Trends in Nonlinear Dynamics and Pattern Forming Phenomena* (Ed. P. Coullet and P. Huerre) Plenum, New York (1990); P. Coullet, L. Gil, and J. lega, Phys. Rev. Lett. **62** 1619 (1998)

[13] E. Falcon, S. Fauve, and C. Laroche, Phys. Rev. Lett. **98**, 154501 (2007)

[14] E. Falcon, C. Laroche, and S. Fauve, Phys. Rev. Lett. **89**, 204501 (2002); Phys. Rev. Lett. **91**, 064502 (2003)

[15] F. Petrélis, S. Aumaître and S. Fauve, Phys. Rev. Lett. **94**, 070603 (2005)

[16] Y. Kuramoto, Prog. Theo. Phys. Suppl. **71**, 1182 (1978); G.I. Sivashinsky, Acta Astronautica **4**, 1177 (1977)

[17] B.W. Zeff, B. Kleber, J. Fineberg, D.P.Lathrop, Nature, 403 (6768):401-4 (2000)

[18] A. Papoulis, *Probability, Random Variables, and Stochastic Processes* (2nd ed. New York, McGraw-Hill), pp. 104,148, (1984)

[19] E. A. Kuznetsov, JETP **80**, 83-89 (2004)

[20] S. Residori, R. Berthet, B. Roman and S. Fauve, Phys. Rev. Lett.**88**, 024502 (2001); R. Berthet, A. Petrossian, S. Residori, B. Roman and S. Fauve, Physica D **174**, pp. 84-99 (2003)

[21] S. Kabashima, S. Kogure, T. Kawakubo, and T. Okada, J. Appl. Phys. **50**, 6296 (1979); T. Kawakubo, A. Yanagita, and S. Kabashima, J. Phys. Soc. Jpn. **50**, 1451 (1981)

[22] V.V. Zautkin, B. I. Orel, and V. B. Cherepanov, Sov. Phys. JETP **58**, 414 (1983)

[23] J. Sommeria, J. Fluid Mech. **170** 139-168 (1986)

[24] J. Fraden, *AIP Handbook of Modern Sensors:Physics, Designs, and Applications* (Springer, New York, 3rd edition (2003))

[25] E. Falcon, C. Laroche, and S. Fauve, Phys. Rev. Lett. **89**, 204501 (2002)

[26] R. Ricou and C. Vivès, Int. J. Heat Mass Transfer **25**, 1579 (1982); A. Cramer, K. Varshney, T. Gundrum, and G. Gerbeth, Flow Meas. Instr. **17**, 1 (2006)

[27] M. Berhanu, B. Gallet, N. Mordant, and S. Fauve, Phys. Rev. E **78**, 015302 (2008)

Chapter 6

Fluctuations in Capillary Wave Turbulence

This last chapter is devoted to *wave turbulence*. In this state, a set or weakly nonlinear surface waves interact randomly between themselves, developing a stationary state where fluctuations in wave amplitude occur that cannot be described by equilibrium distributions. We will focus mainly on experimental studies on wave turbulence at air-fluid (or fluid-fluid) interface when the effect of surface tension is important.

In the first section, we give a short overview of the theoretical background of wave turbulence and the handful of experimental studies made so far on the subject, particularly on a set of studies of gravito-capillary wave turbulence performed in laboratory experiments. Later, we describe our experimental devices used to study capillary wave turbulence. Then, we present the experimental results.

6.1 Wave Turbulence

It was established 40 years ago that a set of weakly coupled dispersive waves can develope an out-of-equilibrium steady state called wave turbulence[1]. In this state, the wave amplitude $A_k(t)$ of the mode with wave number k, fluctuates due to the weakly nonlinear interactions with other waves and a statistical description of the wave system properties (such as the fluctuations of energy, momentum and other conserved quantities for the wave system) must be used. The equations of motion are typically of the form

$$\frac{dA^s_{\mathbf{k}}}{dt} + is\omega_{\mathbf{k}}A^s_{\mathbf{k}} = \sum_{s_i}\int L^{ss_1s_2s_3...s_N}_{\mathbf{k}\mathbf{k}_1\mathbf{k}_2\mathbf{k}_3...\mathbf{k}_N}A^{s_1}_{\mathbf{k}_1}A^{s_2}_{\mathbf{k}_2}A^{s_3}_{\mathbf{k}_3}...A^{s_N}_{\mathbf{k}_N}\delta(\mathbf{k}_1+\mathbf{k}_2+\mathbf{k}_3+...-\mathbf{k})d\mathbf{k}_{123...N} \qquad (6.1)$$

where the s_i are equal to $\pm$ in such a way that $A^+_{\mathbf{k}} = A_{\mathbf{k}}$ and $A^-_{\mathbf{k}} = A^*_{\mathbf{k}}$. This equation has two main contributions to the evolution of $A_{\mathbf{k}}$: the oscillation related to the typical pulsation frequency of the waves ($is\omega_{\mathbf{k}}A^s_{\mathbf{k}}$) and the nonlinear interaction term, which relates the local interaction of a number N of waves with wave number $\mathbf{k}_i$ and amplitudes $A^{s_i}_{\mathbf{k}_i}$ through a scattering matrix $L^{ss_1s_2s_3...s_N}_{\mathbf{k}\mathbf{k}_1\mathbf{k}_2\mathbf{k}_3...\mathbf{k}_N}$ which only takes into account the wave vectors which satisfy the resonance $\mathbf{k}_1+\mathbf{k}_2+\mathbf{k}_3+...+\mathbf{k}_N=\mathbf{k}$. Theoretically, the equations of evolution of the amplitudes $A_{\mathbf{k}}$ come from a Hamiltonian, which is nonlinear in $A_{\mathbf{k}}$. There is no dissipation taken into account in the theory, at least in a transparency window in between the injection scale (usually set at $\mathbf{k}$ =0 or at the scale of the system) and the dissipation scale. In wave turbulence theory, the dissipation scale is usually set at $\mathbf{k}\to\infty$. In the deduction of this type of equations, certain hypothesis have been used, namely the homogeneity and isotropy of space, locality of the interactions (which means that the wave vectors that can interact to

contribute to the evolution of $A_{\mathbf{k}}$ are the ones that satisfy the resonance condition described above in the so called *resonant manifold*) and a certain degree of ergodicity in order to take averages in space and relate them to the temporal averages.

The strength of the theory comes from the possibility of describing the evolution of the wave amplitude in terms of the density distribution of wave numbers $n_{\mathbf{k}}$, which is related directly to the second moment $\langle A_{\mathbf{k}} A^*_{\mathbf{k}'} \rangle = n_{\mathbf{k}} \delta(\mathbf{k} - \mathbf{k}')$ of the fluctuating wave amplitude $A_{\mathbf{k}}$. It is important to notice that higher moments of the wave amplitude $\langle A^{s_1}_{\mathbf{k}_1} A^{s_2}_{\mathbf{k}_2} A^{s_3}_{\mathbf{k}_3} ... \rangle$ can be written as a function of $n_{\mathbf{k}}$ only, because there exist an asymptotic closure for the problem [3].

The distribution $n_{\mathbf{k}}$ displays a slow dynamical evolution (the pulsation frequency is eliminated from the effective dynamics and enters as a condition of resonance of the wave set), given by the small nonlinear interaction between waves of different wave numbers, at slow time scales with respect to the fast dynamics of the dispersive wave system. The separation between the fast (linear) and slow (nonlinear) time scales makes possible to describe the evolution of the wave system to an out-of-equilibrium state by a means of a kinetic equation for $n_{\mathbf{k}}$. The kinetic equation has the form

$$\begin{aligned} \partial_t n_{\mathbf{k}} &= \pi \sum_{\mathbf{k}_i} \int (|L^{ss_1s_2}_{\mathbf{k}\mathbf{k}_1\mathbf{k}_2}|^2 \delta(\mathbf{k} - \mathbf{k}_1 - \mathbf{k}_2)(n_{\mathbf{k}_1} n_{\mathbf{k}_2} - n_{\mathbf{k}}(n_{\mathbf{k}_1} + n_{\mathbf{k}_2})) \\ &- 2|L^{s_1ss_2}_{\mathbf{k}_1\mathbf{k}\mathbf{k}_2}|^2 \delta(\mathbf{k} - \mathbf{k}_1 - \mathbf{k}_2)(n_{\mathbf{k}} n_{\mathbf{k}_1} - n_{\mathbf{k}_1}(n_{\mathbf{k}} + n_{\mathbf{k}_2})))\delta(\omega_{\mathbf{k}} - \omega_{\mathbf{k}_1} - \omega_{\mathbf{k}_2}) d\mathbf{k}_{12}, \end{aligned} \tag{6.2}$$

for 3 interacting waves, for instance [1]. It takes into account only the second moment of the wave amplitude. The higher moments of the amplitude are computed as a function of $n_{\mathbf{k}}$, and that is used to compute the kinetic equation.

The density distribution evolves by a resonance processes between waves to a stationary state. The number of interacting waves depends on both the dispersion relation $\omega_{\mathbf{k}} = \omega(\mathbf{k}) = \omega(k)$ and the order of nonlinearity of the expansion of the interaction terms between waves. The kinetic equation in wave turbulence posseses, very much like the Boltzmann equation for a diluted gas, an $\mathcal{H}$ theorem that drives the system in an irreversible way to the thermodynamic equilibrium (characterized by the Rayleigh-Jeans distribution). An important point of this theoretical developement is the fact that the kinetic equation can support non trivial solutions, different from those of thermodynamics equilibrium. Zakharov [2] proved that there are out-of-equilibrium solutions that describe the transport of conserved quantities like energy from the large scale of the injection of energy to the small scale, where energy is dissipated. Within this inertial bandwidth of wave numbers a power-law density distribution is a solution: $n_k \sim k^{-\alpha}$, with $\alpha > 0$ the Kolmogorov-Zakharov exponent which depends on the type of dispersion relation and the number of nonlinear interactions. By analogy with the energy cascade in fully developed hydrodynamic turbulence [4] these solutions are named Kolmogorov-Zakharov's spectra (KZ). KZ spectra have been theoretically predicted for gravity and capillary surface waves [5, 6], Alfvèn waves in astrophysical plasmas [7], ion waves in plasmas [8], nonlinear optics [9], bending waves in thin elastic sheets [10] and so forth. Moreover, numerical simulations show the realisation of wave turbulence regimes with KZ power-law spectra in gravity [11] and capillary [12] wave turbulence.

Even though wave turbulence has been theoretically and numerically studied in several physical systems, experimental evidences of the appearence of this out-of-equilibrium state are scarce. KZ spectra have been observed in atmospheric science [13], surface capillary waves [14, 15, 16], internal waves in the ocean [17] and spin waves in solids [18]. In all these experimental studies, there was no control of the injection mechanism nor on its effect on the nonlinear interactions between waves.

Recently, a new set of experimental studies have been conducted on the subject of gravito-capillary wave turbulence in laboratory [19, 20]. In these experiences, a capacitive wire gauge recorded the

local wave amplitude fluctuations $\eta(t)$ of random waves forced at the surface of a fluid. To record the local wave amplitude, we will use the same principle of capacitive measurement of [19, 20] in our experimental study.

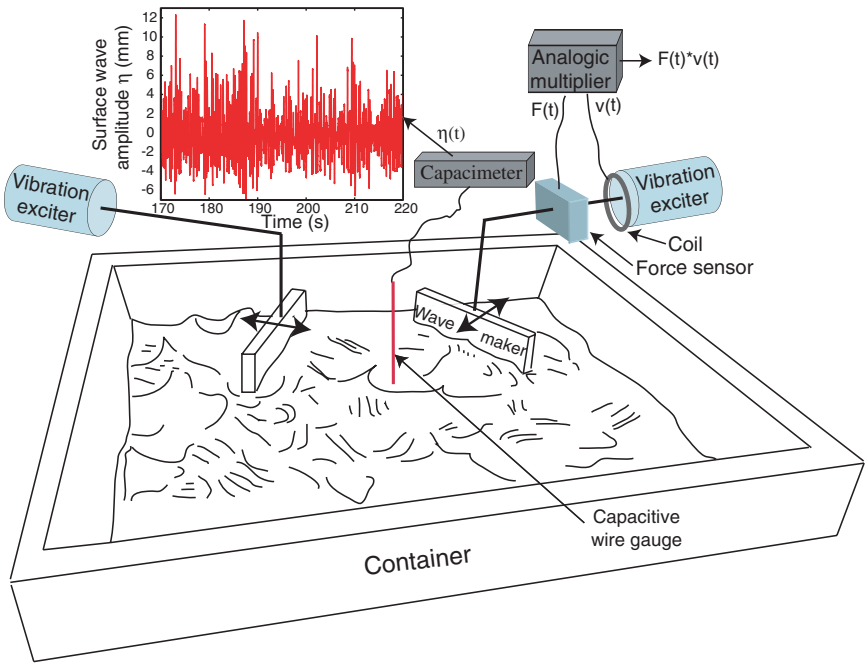

Figure 6.1: Laboratory gravito-capillary wave turbulence experimental set-up and a typical time recording of the surface wave height, $\eta(t)$ at a given location during 50 s. (Taken from [19]).

6.2 Gravito-capillary wave turbulence in laboratory experiments

To introduce the subject, we describe the experiment used in [19, 20] to study gravito-capillary wave turbulence, as it is schematically shown in Fig.(6.1). Contrary to the case of parametric excitation described in Chapter 5, surface waves are generated here by the horizontal motion of two rectangular (10 x 3.5 cm^2) plunging Plexiglas wave makers driven by two electromagnetic vibration exciters (B & K 4809) via a power supply (Kepco Bop50-4A). The wave makers are driven with random noise excitation, supplied by a function generator (SR-DS345), and selected in a frequency range 0-f_{driv} with f_{driv} in the range 4 to 6 Hz by a low-pass filter (SR 640). This corresponds to wavelengths of surface waves larger than 4 cm. This is in contrast with most previous experiments on capillary wave turbulence driven by a monochromatical excitation frequency (mainly parametric amplification [14, 15, 16]). Surface waves are generated 2.2 cm inward from two adjacent vessel walls and the local displacement of the fluid in response to these excitations is measured 7 cm away from the wave makers. The size of the container is 200 x 200 mm^2 filled with fluid up to 20 mm.

From the acquired local wave amplitude fluctuations of η the probability density function (PDF) and power spectral density (PSD) were computed, as shown in Fig.(6.2). For large forcing amplitudes, when gravito-capillary turbulence is developed over the surface, the PDF of η is asymmetric. The

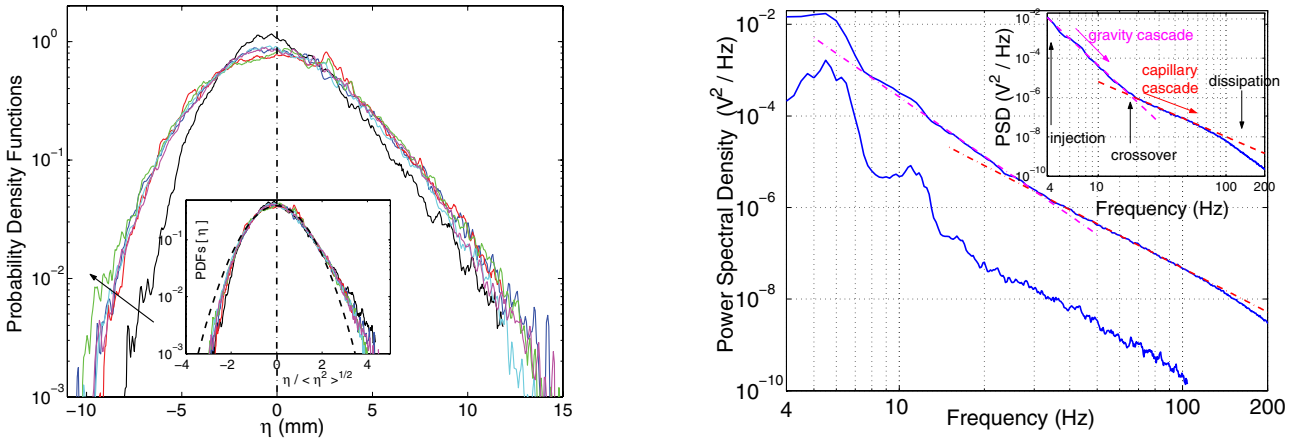

Figure 6.2: **Left:** Probability density function of the local wave amplitude η for 6 different values of the fluid depth, from $h = 18$, 35, 55, 80, 110, to 140 mm (see the arrow). The frequency band is $0 \leq f \leq 6$ Hz. Inset: Same PDFs displayed using the reduced variable $\eta/\sqrt{\langle \eta^2 \rangle}$. Gaussian fit with zero mean and unit standard deviation (dashed line). **Right:** Power spectra of the local wave amplitude η for two different driving amplitudes. The frequency band is $0 \leq f \leq 6$ Hz. Dashed lines have slopes -4.3 and -3.2. Inset: The frequency band is $0 \leq f \leq 4$ Hz. Dashed lines had slopes of -6.1 and -2.8. (Both figures are taken from [19]).

high crests (positive events) are more probable than the deep troughs (negative events). The mean level of local wave amplitudes $\langle \eta \rangle \simeq 0$. In the rescaled variable $\eta/\sqrt{\langle \eta^2 \rangle}$, all the PDFs collapse on the same curve. This behavior does not change when the fluid depth is increased.

The power spectrum of the surface wave amplitude is recorded from 4 Hz up to 200 Hz during a time period ($\sim$ 2000 s), large with respect to the smallest resolved frequency, in this case, 4 Hz. When the forcing is small, peaks related to the forcing and its harmonics are visible in the low frequency part of the spectrum, as it is displayed in Fig.(6.2) (left, lower curve). When the forcing is increased, the peaks related to the forcing and its harmonics are smeared out. A power law type of spectrum developes in a small band of frequencies. At higher frequencies, larger than 30 Hz, another power law can be fitted with a different slope. This frequency f_c corresponds to the transition from gravity-driven waves to capillarity-driven waves and is related directly to the capillary length l_c. At this length both restitution forces have the comparable effect in the dispersion relation

$$\omega(k)^2 = gk + \frac{\sigma}{\rho}k^3,$$

for a deep layer of fluid of density ρ and surface tension σ (see Chapter 4). From this relation, the capillarity length is computed as $l_c = \sqrt{\sigma/g\rho}$, giving a cross-over frequency $f_c = \sqrt{g/2\pi^2 l_c}$. For the working fluid, mercury, $l_c \sim 1.74$ mm and $f_c \sim 17$ Hz. These parameters keep the same order of magnitude when the fluid is changed for water. The capillary length cannot be significantly changed using other interfaces between simple liquids and air. It is at an intermediate scale between the size of the experiment and the dissipative length. The theoretical value f_c is in good agreement with the experiment (see inset in Fig. (6.2)) for a low-frequency broad band forcing. At higher forcing, there is a shift (see main Fig.(6.2)) which can be due to nonlinear interactions between gravity and capillary waves, but that deserves to be experimentally and theoretically studied. At even larger frequencies, larger than 100 Hz, the dissipation of surface waves takes place at the capacitive wire meniscus.

The experimental spectrum density was compared to the theoretically predicted KZ power spectral density $S_\eta(f)$ which follows a power law depending on the resitution force acting on the wave system. For surface wave turbulence, the predicted spectra [1] are

$$\begin{aligned} S_\eta(f) &\sim \epsilon^{1/3} g f^{-4} \quad \text{for gravity waves,} \\ S_\eta(f) &\sim \epsilon^{1/2} \left(\frac{\sigma}{\rho}\right)^{1/6} f^{-17/6} \quad \text{for capillary waves,} \end{aligned} \tag{6.3}$$

where ϵ is the mean injected energy flux per unit of mass into the system. The exponent in the spectra is related directly to the number of waves which take part in the scattering matrix L and the dispersion relationship. For gravity waves, 4 waves interact in the resonant process, and for capillary wave turbulence, 3 waves interact (unless certain symmetries are impossed to the system).

These spectra can be also found by dimensional analysis [21]. To do so, one can use

$$\int_{-\infty}^{\infty} S_\eta(f) df = \langle \eta^2 \rangle,$$

which has units of (distance)^2, that we will write as L^2. As df has units of inverse of time T^{-1}, $S_\eta(f) \sim L^2 T^1$. The other parameters of the system have the following units $g \sim LT^{-2}$, $(\sigma/\rho) \sim L^3 T^{-2}$, $f \sim T^{-1}$ and $\epsilon \sim L^3 T^{-3}$. Using dimensional analysis, we assume that we can write the power spectrum density as a polynomial function Ψ of the adimensional parameters of the problem called Π_i. The number of independent Π_i is given by the number of dimensional quantities of the problem (in this case 5) minus their dimensional units (in this case distance L and time T, i.e. 2)) [22]. Then Ψ can be written as

$$\Pi_1 \equiv \frac{S_\eta(f)}{\epsilon^{2/3} f^{-3}} = \Psi(\Pi_2 \equiv \frac{\sigma f}{\epsilon \rho}, \Pi_3 \equiv \frac{g^3 f^{-3}}{\epsilon}). \tag{6.4}$$

In the wave turbulence regime, where the forcing applied at large scale is discarded ($f/f_c \ll 1$), the surface wave turbulence spectrum of local wave amplitude $S_\eta(f)$ can be either driven by gravity

$$\lim_{\Pi_2 \to 0} \Psi(\Pi_2, \Pi_3) \to \Psi_{grav}(\frac{g^3 f^{-3}}{\epsilon}),$$

or surface tension

$$\lim_{\Pi_3 \to 0} \Psi(\Pi_2, \Pi_3) \to \Psi_{cap}(\frac{\sigma f}{\epsilon \rho}).$$

At this point, we cannot conclude on the behavior of the function Ψ, and certain assumptions have to be made. We mainly assume that the the number of interacting waves will fix the power-law behavior of Ψ though the energy flux ϵ: for N resonant wave process, the spectrum $S_\eta(f)$ dependence on the energy flux goes as $\epsilon^{\frac{1}{N-1}}$. For gravity waves, the number of waves interacting in the gravity regime is 4 [21], the exponent of the mean injected power must be 1/3. Therefore $\Psi_{grav}(x) \sim x^{1/3}$ and we get $S_\eta(f) \sim \epsilon^{1/3} g f^{-4}$. For capillary wave turbulence, the number of interacting waves is 3 [21], therefore $\Psi_{cap}(x) \sim x^{1/6}$ and we get $S_\eta(f) \sim \epsilon^{1/2} (\frac{\sigma}{\rho})^{1/6} f^{-17/6}$.

An important result of the experimental study is the strong dependence of gravity wave turbulence on the forcing amplitude: the smaller the amplitude of the forcing, the steeper the slope of the computed power-law spectrum. The experimental value varies from -4 for large forcing amplitude and small driving frequency band (f_{driv}=4 Hz) to almost -7 for small forcing amplitude and large driving frequency (f_{driv}=6 Hz). When the forcing is not strong enough, harmonics of the forcing still

appear over the experimental spectrum [19]. The transition from the forcing peak resonance to the developed gravity wave turbulent state deserves further study.

For capillary wave turbulence, the situation is different. The experimental slope of capillary spectra are close to the theoretically predicted one $S_\eta(f) \sim f^{-17/6}$. It is found to be independent of the forcing [19]. We will further study this regime in this Chapter.

Comment on the relation between frequency (local) and wave number (spatial) measurements: The experimental power spectrum density discussed in the previous section is deduced from the recorded wave amplitude fluctuations of a local measurement. This spectrum, when wave turbulence is developed in the surface wave system, displays two distinct frequency windows where a power-law type of spectrum developes: at low frequency (in between f_{driv} and f_c) a gravity wave regime, and at high frequency (in between f_c and f_{dis}), a capillary one. For each regime, a comparison between experiment and theory was made [19]. The point we would like to discuss briefly here is the fact that the theoretical calculations of the power spectrum density are made on wave number space [1] and not in frequency domain. As we are considering a statistically homogenous system in space, it is natural to compute the moments and statistical properties of the wave fluctuations by taking space averages. Nevertheless, from the experimental point of view, taking space averages is quite a difficult task. On the contrary, time averages of local wave amplitudes are much accessible. It is possible to relate both for stationary solutions in the linear regime as follows:

$$n_T(\omega) \propto k^{d-1} \frac{dk}{d\omega} n(k)$$

where $n_T(\omega)$ is the time averaged density distribution, now written in frequency domain, and d is the dimension of the space where waves propagate (in this case $d = 2$). This is done by assuming the validity of the linear dispersion relation $\omega_k = \omega(k)$, where $\frac{d\omega(k)}{dk}$ is well defined. The fulfillment of the dispersion relation in the weakly nonlinear regime is taken as a fact for the comparison between theoretically and experimentally computed power spectrum densities. In what rests, we will assume that the dispersion relation is valid.

6.3 Capillary wave turbulence

Capillary waves are ubiquitous in nature. They appear whenever the interface between two fluids is perturbed. In the presence of another restitution force that can sustain surface waves (such as gravity or a magnetic field), a competition between both will occur, generating naturally a crossover length (in the case of gravito-capillary waves, it is the capillary length l_c). When forced out-of-equilibrium, their nonlinear interaction can produce a turbulent-like regime termed capillary wave turbulence. Capillary wave turbulence is the assymptotic regime where dispersive capillary waves at the interface between two fluids interact randomly through weak nonlinearities. This interaction generates an out-of-equilibrium stationary state where the density distribution n_k displays a power-law behavior as a function of the wave-number k. In this subject, theoretical, numerical and experimental studies agree in showing the appearance of a scale-invariant KZ spetrum. Even so, there are several aspects of capillary wave turbulence that have not been properly addressed or compared between theory, experiments and numerical simulations, for instance, the non-gaussianity of the wave amplitudes [23], the nature and existence of intermitency in a wave system [20, 24] or the role of symmetries and dissipation in the wave interactions [25, 26]. From the experimental point of view, gravity waves have always been present in the former experiments [14, 15, 16], and their nonlinear interactions with capillary waves has not been taken into account theoretically nor experimentally.

To adress these points, pure capillary wave turbulence must be studied. The main issue in ground experiments in surface wave turbulence is the interaction between diferent types of waves acting in the same system, such as the case of gravito-capillary wave turbulence. Through the characteristic scales of each cascade, energy and other conserved quantities must be transported. This is done through different processes, envolving different mechanisms. Therefore, to properly study pure capillary wave turbulence, surface gravity waves must be either negligible or eliminated. In the following section, we present two experimental configurations where this can be achieved.

6.3.1 Experimental set-up and measuring techniques

We present now the experimental devices used to study the statistical properties of the local wave amplitude fluctuations in pure capillary wave turbulence at the interface between two fluids. To be able to neglect gravity effects as spureous contamination of the capillary regime we designed two different set-ups. The first experiment, realized in a low-gravity environment, allowed us to probe the local wave amplitude fluctuations in a capillary wave turbulence regime and also parametrically amplified surface waves in a spherical container. It is the first experimental report on low frequency (large scale) capillary wave turbulence. The second laboratory experiment was performed using a gravity-matching technique, where two inmiscible fluids of similar densities where superposed, eliminating the acceleration of gravity from the surface wave dynamics. In this configuration, capillary waves in deep fluids display a symmetric distribution of amplitudes with respect to the equilibrium level, in contrast to the gravito-capillary wave turbulence distribution of wave amplitudes.

Microgravity experiment

Before describing the experimental set-up, we first explain the procedure and the necessary considerations to perform an experimental study in a low-gravity enviroment. Low-gravity enviroment is achieved by flying with the specially modified Airbus A300 Zero-G aircraft (operated by Novespace for the Centre National d'Etudes Spatiales [27] at Bordeaux, Merignac), through a series of parabolic trajectories (~ 90) which result in low-gravity periods, each one of 20 ± 2 s. Two campaigns where performed, separated by 6 months. In the first (last) second of the parabolic flight, the acceleration of gravity decreases (increases) and transient effects can polute the experimental measurements. Due to this fact they are not taken into account in the acquisition of data, and only 18 s are acquired. The effective gravity g_{eff} in a typical trajectory is low with respect to the acceleration of gravity g on ground $g_{eff}/g \sim 5$ x 10^{-2}. Although small, fluctuations in g_{eff} occur, called g-jitters.

Experimental device: The dynamical part of the experimental set-up is depicted schematically in Fig. (6.3). An inner container is partially filled with a fluid. The container geometry is either spherical (15 cm in diameter) or cylindrical (15 cm in diameter, 18 cm in length). Each container is made of a wetting material (Plexiglas cylinder or glass sphere) to avoid that the fluid loses contact with the internal wall of the container during the microgravity phases. According to its geometry, the container is filled with 20 or 30 cl of fluid. This corresponds to an uniform fluid layer of roughly 5 mm depth covering all the internal surface of the container during the microgravity phases. The inner container is fixed inside an outer container which is made of polycarbonate (Lexan) and is air-tight to avoid fluid leaks. Security standards have to be respected in order to performed experiments in low gravity. As it is shown in Figs. (6.3) and (6.4), the whole system is put down on a rail and is submitted to vibrations by means of an electromagnetic exciter (BK 4809) via a power supplied (BK

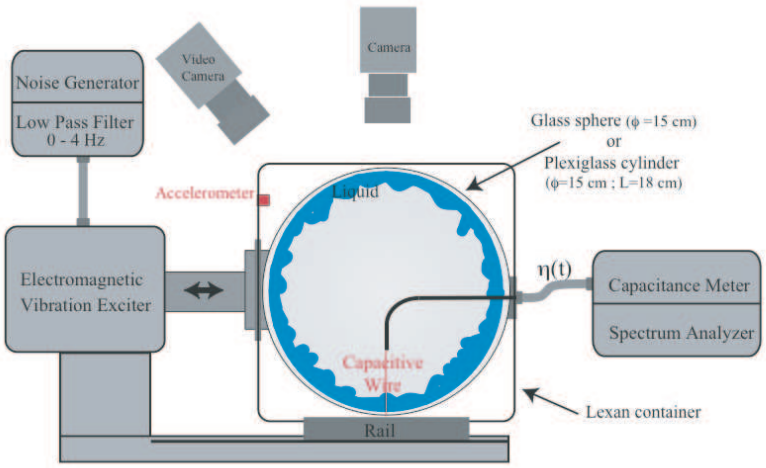

Figure 6.3: First Experimental set-up: Microgravity experiment. A spherical or cylindrical cell is filled with a fluid. The waves at the surface of the fluid are excited by a low-frequency (large scale) forcing performed by an electromagnetic shaker. Local wave amplitude fluctuations are measured by means of a capacitive wire gauge. Acceleration measurements were done by means of a piezoelectric accelerometer and a charge amplifier. The fluid motion and local wave patterns are also recorded by means of a camera and a videocamera.

2706). We have used two type of forcings: sinusoidal to study parametric instabilities and random to study wave turbulence.

- In the wave turbulence case, the container is driven with random noise, supplied by the source of a dynamical analyzer (Agilent 35 670A), and low-pass filtered in the frequency range 0 - 6 Hz by a low pass filter (SR 650). This corresponds to wavelengths of surface waves larger than 1 cm in zero gravity.

- In the case of wave patterns, the container is driven with a sinusoidal forcing at frequency f_0 in the range $10 \leq f_0 \leq 70$ Hz, forcing amplitude d_0 of few mm corresponding to a container acceleration $0.1\ g \leq a_0 \leq 30\ g$.

In this chapter, we will focus mainly on random forcing. Further investigations of the dynamical properties of parametrically excited surface waves are presented in the publication on the subject in the Appendix. The local acceleration of the container is measured with a piezoelectric accelerometer (B & K 4803), which is screwed on the container, and a charge amplifier (B & K 2635). The fluid used is either ethanol or water. The local displacement of the fluid is measured with two capacitive wire gauges, plunging perpendicularly to the working fluid in two different places. At the beginning of each recording, great care was taken to have one wire gauge always plunging into the fluid in order to avoid voltage jumps if the water dewets locally the wire. The sensor working mechanism, linear dynamical range and response time were described in the previous chapter. In the first campain, a dynamical signal analyzer (Agilent 35670A) is used to record the power spectrum of the surface wave amplitude and the acceleration of the container during each microgravity phase. In the second campaign, both type of signals are low-pass filtered with an electronic filter (SR650) at 4 kHz to avoid aliasing and recorded simultaneously at 10 kHz using an acquisition card (National Instruments PCI 6052E) inserted into a PC. The fluid surface is visualized with a Nikon camera and recorded with

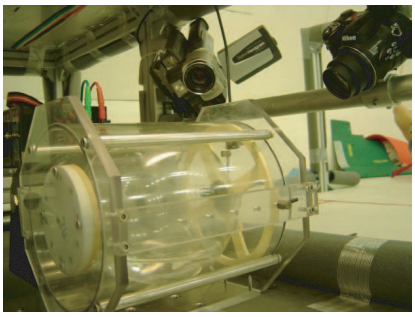


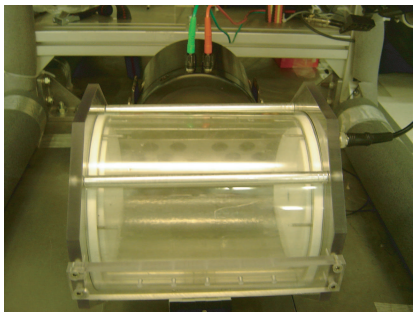

Figure 6.4: **Left:** Outer container in the low-gravity set-up with inner spherical container.**Center:** Experimental set-up mounted on aluminium rack on Airbus A300 Zero-G. **Right:** Outer container in the low-gravity set-up with inner cylindrical container. (Photos taken with gravity (fluid is at the bottom of the container).

a Sony video camera. The whole acquisition system and dynamical set-up is screwed into a rack (136 cm x 76 cm x 143 cm) which is in turn screwed tight to the plane (see Fig. (6.4)). During microgravity experiments and when no vibration is applied, we observe that the fluid crawls up the sides of the container. The fluid then covers all the internal surface of the inner container due to the capillary forces. Contrary to the common sense, no formation of a single sphere of fluid is observed in the middle of the tank, due to these capillary effects and the relative small amount of fluid. A roughly homogeneous fluid layer is then formed on the internal surface of the container, confining air in its center. Over the homogeneous layer, capillary waves form and fluctuations occur.

Gravity-matching experiment

The second way to elimate gravity waves is to design a set-up where two superposed fluids with the same (or almost the same) density ρ. In this configuration, complete (or almost complete) buoyancy is achieved and the effective gravity of the system becomes negligible. In this configuration, the surface waves have no prefered orientation with respect to the vertical and pure capillary waves dominate. The effective gravity can be controled by means of the density difference related to the Atwood number $A = (\rho_1 - \rho_2)/(\rho_1 + \rho_2)$ which acs in the dispersion relation of the surface waves in deep fluid layers as

$$\omega^2(k) = \frac{\rho_1 - \rho_2}{\rho_1 + \rho_2} gk + \frac{\sigma}{\rho_1 + \rho_2} k^3, \tag{6.5}$$

where ρ_1 is the density of the upper fluid, ρ_2 is the density of the lower fluid and σ is the surface tension. For A=0, the only restitution force is surface tension and capillary wave turbulence can develope on the interface. In the case of equal depth of the superimposed fluids, the number of interacting waves in the scattering matrix increases and therefore the theoretically predicted capillary wave turbulence spectrum shifts its slope (as it can be seen in the publications in the Appendix). This can be understood by symmetry arguments: the interaction term has to take into account the

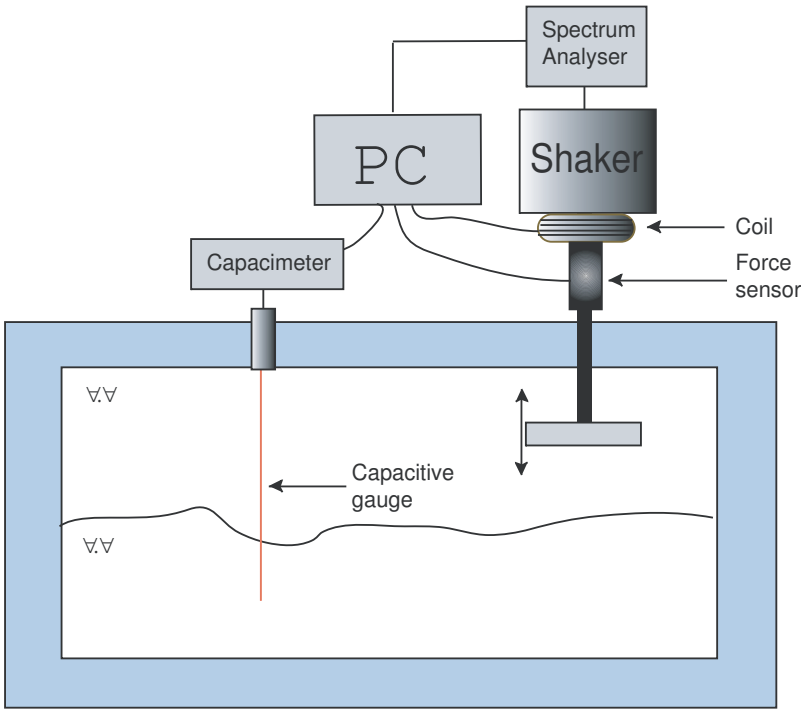

Figure 6.5: Second Experimental set-up: Gravity-matching experiment: A closed container is filled with an oil/water mixture. The waves at the interface are excited by a low-frequency random forcing performed by a plunging wavemaker driven by an electromagnetic shaker. Local wave amplitude fluctuations are measured by means of a capacitive wire gauge.

$z \rightarrow -z$ invariance, and no odd-terms can appear, changing the order of the nonlinearity of the interaction term. This imposed symmetry may as well change the PDF of the local wave amplitude, because no difference can appear between crests and troughs. The slope and skewness changes can be checked experimentally. We present in the following section the experimental device we have developed for this matter.

Experimental device: The experimental device used to study capillary wave turbulence is shown in Fig. (6.5). A Plexiglass container (height h=60 mm, length l=100 mm, depth d=80 mm) is half filled with distilled water (density ρ_1 =1.00 g/cm^3, kinematic viscosity ν_1 =0.01 cm^2/s) and half filled with silicon oil (PDMS from ABCR GmbH & Co., density ρ_2 =0.96 g/cm^3, kinematic viscosity ν_2 =0.07 cm^2/s). The surface tension coefficient for the fluids interface is $\sigma \sim 30$ mN/m. This value depends on the chemical origins of the PDMS, but it cannot be lower than 10 mN/m [28]. The equilibrium interface position is measured at 35 $\pm$ 2 mm. The capillary surface waves are excited in first place by a rotating Plexiglass wavemaker whose blade is plunging in between both fluids. The wave blade oscillated between to angles and its motion is controlled by a SSD motor from Parvex driven by a random gaussian noise coming from one of the outputs of a HP 8904A frequency generator with cut-off frequency $f_{driv} = 3$ Hz. At very low forcing amplitude, the motion of the wave blade creates large bubbles. This is due to the wetting properties of the silicon oil on the wave blade. Any small motion, produces bubbles of water in oil that are advected by the flow generated by the wavemaker oscillation. We thus discarded this method. The method that we used afterwards is also based on a wave-maker that plunged into the upper fluid, oscillating vertically without approaching the lower fluid. The wave-maker is driven by an electromagnetic vibration

exciter (B & K 4809) via a power amplifier. The random forcing, supplied by the source output of a dynamical spectrum analyzer (HP 8904 A), is low-pass filtered to a range between 0-3 Hz. We control the forcing amplitude such that no bubble is present in the cell. The excited surface wave amplitude η is locally measured 4 cm away from the container walls by means of a capacitive gauge, 0.1 mm in diameter. The measured capacitive fluctuations are proportional to the local wave amplitude ones. They are sampled at 500 Hz during 300 s. The calibration and linear response of this type of measurement is described elsewhere [19]. We checked the constant frequency response of the wire probe for the water-oil boundary in a frequency band between 1 to 100 Hz by means of an accelerometer solidary to the probe and a charge amplifier. The only noteworthy differences are that in this case both the dielectrics are liquids of similar densities and similar viscosities. We used the fact that the linear response of this type of measurement depends on the dielectric ratio of the fluids, in this case $\varepsilon_{water}/\varepsilon_{oil} \sim 40$, giving good signal to noise ratio for this oil-water mixture.

6.3.2 Experimental results

We present now the experimental results on capillary wave turbulence in the two configurations described above.

Microgravity experiment

In the low gravity phase, when the container (either the cylindrical or the spherical one) is excited by a low-frequency random forcing, surface wave fluctuations appear over the fluid layer. Even in some cases these fluctuations are excited solely by the g-jitters. In this experimental configuration, large events occur where the amplitude η fluctuates strongly. From the acquired signal $\eta(t)$, we compute the power spectral density of η, as shown in Fig.(6.6). One single power-law spectrum is observed on two decades in frequency. Whatever the geometry of the tank (sphere or cylinder) and the large scale forcing (random or sinusoidal), the exponent is found to be close to -3. This spectrum does not depend on the large-scale forcing parameter. Wave turbulence theory predicts a $f^{-17/6}$ scaling of the surface height spectrum for pure capillary regime. This expected exponent is close to the value -3 reported here. Kolmogorov-like spectrum of capillary wave turbulence is thus observed in Fig. (6.6) over two decades in frequency. To our knowledge, this large range of frequencies has never been reached with ground experiments for such large scales. The power spectrum in the presence of gravity is shown for comparison in the inset of Fig. (6.6). It displays two power laws: f^{-5} and f^{-3} corresponding respectively to gravity and capillary wave turbulence regimes. The capillary range is limited at low frequencies $f \leq f_c = \sqrt{\rho g/2\pi^2 l_c} \sim 20$ Hz. The capillary length l_c being of order of a few mm for usual fluids, the critical frequency f_c is in rough agreement with the one observed in the inset of Fig. (6.6). Such a critical frequency corresponds to a wavelength of the order of 1 cm. When $g \rightarrow 0$, the cross-over frequency between both regimes is then predicted to be pushed away to very low frequency. For our microgravity precision, ± 0.05 g, the capillary length then is expected to be close to cm, and the cross-over frequency of the order of 1 Hz, corresponding to wavelength of the order of 10 cm. Thus, in microgravity, for our frequency range (4 Hz up to 400 Hz), the power spectrum of surface wave amplitude is not polluted by gravity waves. At high frequency, the power spectrum in the capillary range in microgravity (Fig. (6.6)) is limited at frequency about 400 Hz due to the low signal-to-noise ratio. Note that the high frequency limitation is lower in the presence of gravity ($\geq$ 100 Hz) as it is shown in the inset of Fig. (6.6). This cut-off frequency is related to the meniscus diameter on the capacitive wire gauge that prevents the detection of waves with a smaller wavelength. In microgravity, this latter effect vanishes since the meniscus diameter becomes

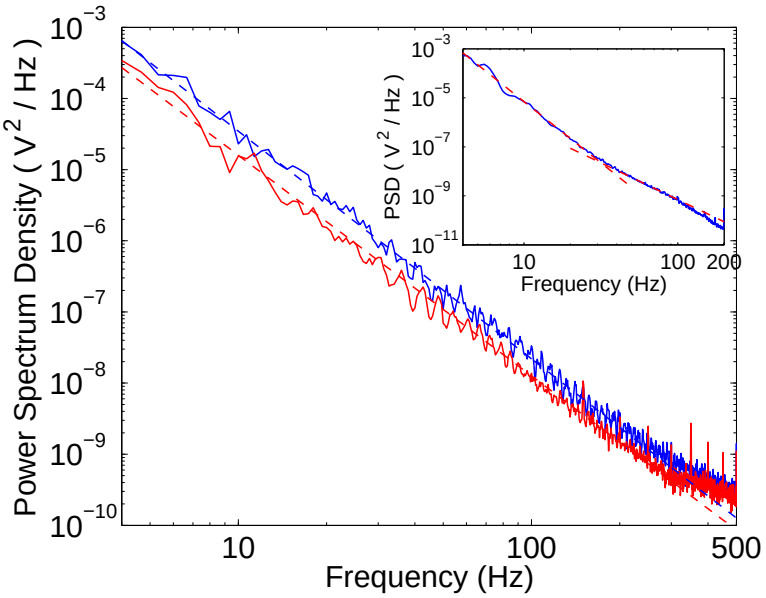

Figure 6.6: Power spectrum density of the local wave amplitude in capillary wave turbulence in microgravity. Lower curve: Random forcing 0 - 6 Hz. Upper curve: Sinusoidal forcing at 3 Hz. Dashed lines with slopes of -3.1(lower) and -3.2 (upper). Cylindrical container filled with 30 cl of ethanol. Inset: Power spectrum density of the local wave amplitude in gravito-capillary wave turbulence. Slopes of dashed lines are -5 (upper) and -3 (lower) corresponding respectively to gravity and capillary wave turbulence regimes. Rectangular container filled with a 20 mm ethanol depth.

of the order of the size of the container. When the container is submitted to random forcing, we observe an invariant-scale power spectrum of wave amplitude on two decades in frequency in roughly good agreement with wave turbulence theory. An inconvenient of the low-gravity measurements is the small acquisition time of the random wave amplitude fluctuations: in an average parabolic flight, we have only ∼20 seconds of dynamical fluctuations associated with capillary wave turbulence. Statistical resolution is not sufficient to resolve correctly the probability density function of the local wave amplitude when large events are present. To bypass this problem, we have performed another set of experiments on ground using gravity-matching fluids.

Comment on parametrically excited waves and wave turbulence: When the container is submitted to periodic excitation, two-dimensional subharmonic patterns with a given symmetry (stripes or hexagons) develope on a spherical or cylindrical fluid surface for forcing strong enough to parametrically excite the surface waves. In this periodic geometry, there are no boundary effects of the waves with the container. We have noticed that their dynamical description cannot be simply subscribed to parametric surface waves. A much more complex picture appears: the wave motion results from the interaction between two instabilities (sloshing motion related to the global motion of the fluid layer and parametric amplification). Note that the slope of the continuous part of the spectrum is steeper in the presence of parametric wave patterns than for wave turbulence ($S_\eta(f) \sim f^{-4}$ in Fig. (6.7) instead of f^{-3} in Fig. (6.6)). This can be related to cusps of the spatial patterns sweeping the sensor, due to the fact that the power spectrum density of a continous signal with derivative discontinuities displays a f^{-4} power-law.

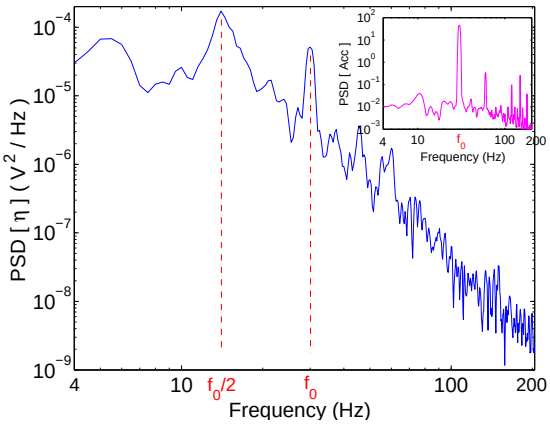

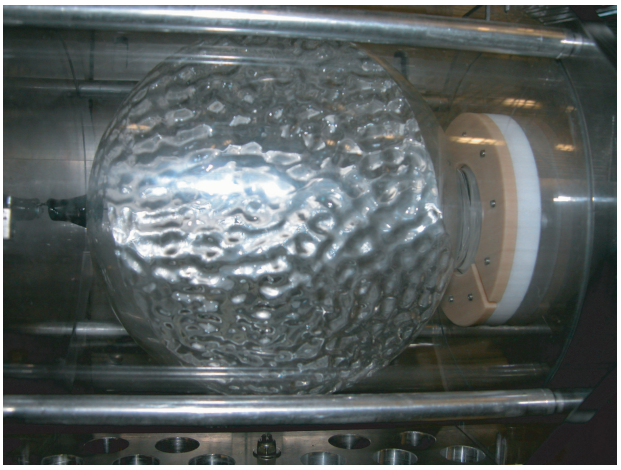

Figure 6.7: **Left:** Typical PSD of local wave amplitude fluctuations when sinusoidal forcing of frequency f_0 =30 Hz is acting on the container, at acceleration value a_0=1.16 g. **Right:** Subharmonic patterns on the spherical surface of a fluid in microgravity.

Gravity-matching experiment

With the data acquired by the capacitive gauge, we calculate the probability distribution function (PDF) of the local wave amplitude η, as shown in Fig. (6.8) (main). We notice that $\langle\eta\rangle \sim 0$ and that its fluctuations are close to being symmetric with respect to $\eta = 0$. No exponential tails are found. The kurtosis of the PDF is slightly larger than 3, but not large enough to exclude gaussianity. For comparison, when replacing the upper fluid with air, we show in Fig. (6.8) (inset), the PDF for the local wave amplitude when gravito-capillary wave turbulence developes. We see the asymmetric tails (positive skweness) as it has been mentioned above. This contrast is a clear indication of the symmetry imposed in the system: there is no external field (such as gravity) that breaks the $z \to -z$ parity thus the surface perturbations are symmetric with respect to $\eta = 0$. It is unclear if the fluctuations are indeed gaussian, but resolution of large events could not be made in the present experimental set-up. As discussed above, the wave system has a very low Atwood number $A = (\rho_1 - \rho_2)/(\rho_1 + \rho_2)$. For the nominal densities of both fluids A=0.02, reducing the effective gravity drastically. The dispersion relation for waves at the interface is, in the case of the deep water limit, written in Eq. (6.5). One finds that in this system the capillary length $l_c = 2\pi\sqrt{A\sigma/g(\rho_1 + \rho_2)}$ where the crossover from gravity to capillary regime takes place is an order of magnitude larger than for liquid-air interface. This means that the frequency crossover between gravity and capillary regimes $f_c = \pi\sqrt{(\rho_1 - \rho_2)g/2(\rho_1 + \rho_2)l_c}$ is obtained at a frequency close to 3-4 Hz for our working fluids. Therefore, when the frequency cut-off of the forcing is larger than f_c, the only KZ-type spectrum we can observe is the capillary one. In Fig. (6.9) we show both the pure capillary (main figure) and the gravito-capillary (inset) spectra. In the capillary-driven transparency window we can see only one scale-invariant spectrum (for frequencies larger than the characteristic frequencies of the broad-band forcing). The slope of the spectrum is roughly $\sim f^{-2.75}$.

The experimental value of the slope is a point worth explaining. We can calculate theoretically the slope of the spectrum in this configuration, as it is shown in the publication in the Appendix. Another way to calculate the spectrum slope is to assume that the number of wave interactions changes from 3 (as the case of the usual capillary wave turbulence) to 4, due to the imposed $z \to -z$ invariance. Using dimensional analysis, we can write the power spectrum density $S_\eta(f)$ as a function of the parameters of the system σ, ρ_1, ρ_2, the average energy flux per unit of mass ϵ and the frequency

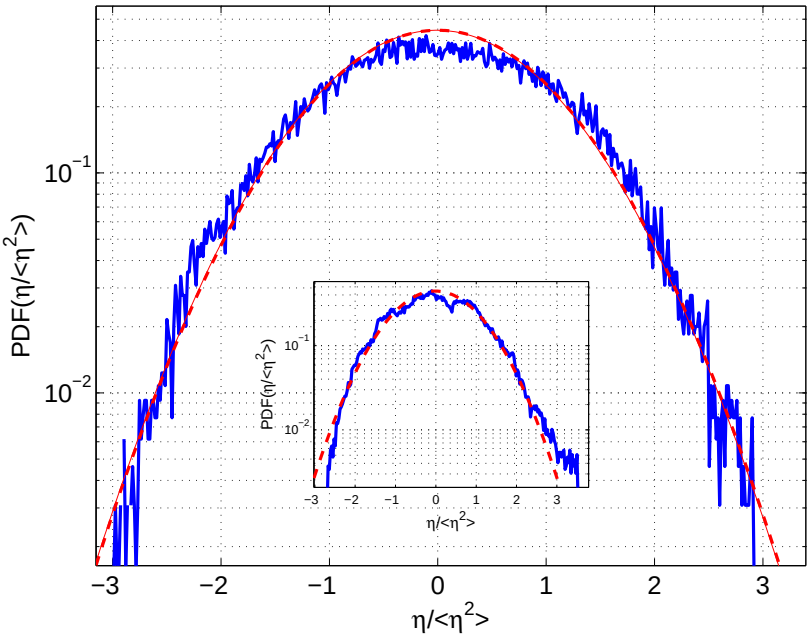

Figure 6.8: Probability density function (PDF) of the local wave amplitude η at the interface of two inmiscible fluids with A=0.02 (in blue) and a parabolic fit (in red). Inset: Probability density function (PDF) of the local wave amplitude η at the interface of a water-air interface with A=1 (in blue) and a parabolic fit (in red).

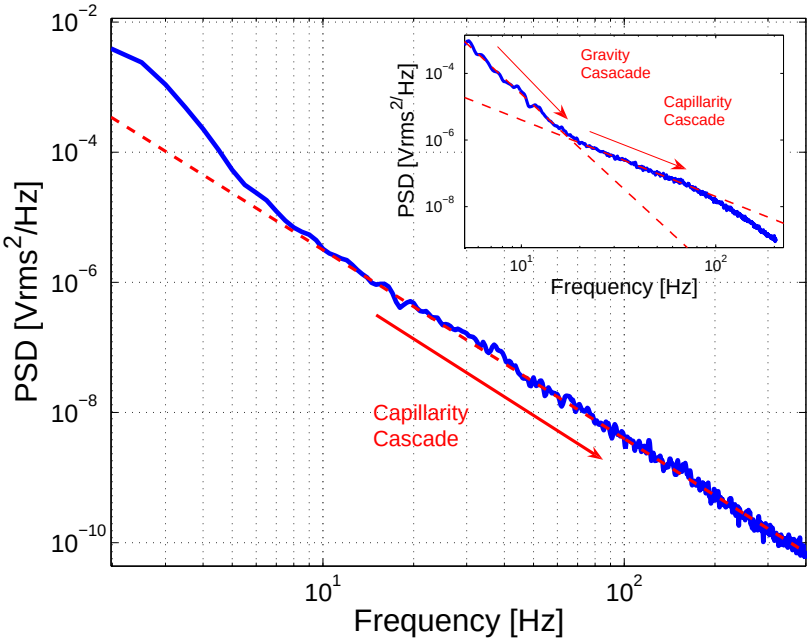

Figure 6.9: Power spectral density (PSD) for the local wave amplitude η at the interface of two inmiscible fluids with A=0.02 (in continuous blue line). Best fit slope $S_\eta(f) \sim f^{-2.75}$ (in dashed red line). Inset: Power spectral density for the local wave amplitude η at a water-air interface with A=1 (in blue) and the best-fit KZ spectra (in red) for gravity and capillary waves, as shown above.

f. As before, $S_\eta(f)$ has units of L^2T and ϵ has units of L^3T^{-3}. We can write $S_\eta(f)$ as a function of the adimensional numbers of the problem. To wit, the power spectrum density of capillary waves in this configuration reads

$$S_\eta(f) = \left(\frac{\sigma}{\rho}\right)^{2/3} f^{-7/3} \times \Phi(A = \frac{\rho_1 - \rho_2}{\rho_1 + \rho_2}, \frac{\rho\epsilon}{\sigma f}) \tag{6.6}$$

where $\Phi(x, y)$ is a polynomial function of two variables and we have used the definition of the Atwood number A. We discard a dependence of Ψ in A and we asume that when $A \to 0$, $\Phi \to \Phi_0$ constant [22]. As it was explained in the beginning of the chapter, for 4-wave interactions, $S_\eta(f)$ depends on the average energy flux per unit of density ϵ (related directly to the mean injected power furnished by the wavemaker) as $\epsilon^{1/3}$. Therefore

$$S_\eta(f) \sim \left(\frac{\sigma}{\rho}\right)^{2/3} f^{-7/3} \times \left(\frac{\rho\epsilon}{\sigma f}\right)^{1/3} \sim \left(\frac{\epsilon\sigma}{\rho}\right)^{1/3} f^{-8/3}.$$

This result is close to the numerically computed PSD $S_\eta(f) \sim f^{-2.75}$, where the error is, in the worst case, 6%.

This slope, as in the previous experiments, is forcing independent. For the small forcing used in this experimental set-up, no cusps over the wave crests were observed, which eliminates the possibility of singularities polluting the spectral content of the signal. This stresses the fact that capillary wave turbulence is a robust phenomenon.

Comment on the cut-off frequency of capacitive measurements : All through this Chapter local capacitive measurements were performed in order to extract the local amplitude fluctuations of the wavy fluid level in two experimental devices where gravity could be removed, or at least neglected, from the surface wave evolution. These fluctuations present a power law spectrum with a given slope over a certain frequency band, which is compared with the one obtained in ground experiments in presence of gravity. The cut-off frequency of both computed spectra are different. For gravitocapillary measurements, the frequency cut-off is close to 150-200 Hz, where a dissipation slope, steeper than the capillary slope develops. This viscous dissipation takes place for small waves that arrived at the meniscus of the fluid at the wire probe. The typical lengths asociated to the cut-off frequency is at least a factor 5, calculated from the dispersion relation of capillary waves for water. In absence of gravity, the capillary frequency f_c goes to zero as $g^{3/4}$ and as the effective gravity of the system goes to zero, close the capacitive wire the small amplitude waves are less atenuated. As the meniscus gets larger and larger, the small amplitude waves are less damped as they approach the wire, making the cut-off frequency larger and larger. In microgravity and gravity matching experiments, the frequency cut-off was of the order of 400-500 Hz.

6.4 Conclusions

We have presented results about pure capillary wave turbulence regime in two different experimental set-ups, where the effect of gravity can be neglected. The main feature of both experiments is the power-law spectrum of the capillary waves, that display a slope independent of the forcing. The experimental PSD of the local amplitude fluctuations shows a power-law behavior ($S_\eta(f) \sim f^{-3.0}$ for the microgravity experiment and $S_\eta(f) \sim f^{-2.75}$ for the gravity matching experiments) which are in farly good agreement with the theoretical predictions. In the microgravity experiment, parametric

surface waves were also studied, although their behavior is not discussed here. In the gravity matching experiment, the PDF of the local wave amplitudes is a gaussian, and no exponential tails where found, which can be seen as a signature of the effect of the symmetry imposed on the system.

Bibliography

[1] V. E. Zakharov, V. S. L'vov, and G. Falkovich, *Kolmogorov Spectra of Turbulence I* (Springer, Berlin, 1992).

[2] V.E. Zakharov, Zh. Eksper. Teoret. Fiz. **51**, 686 (1966)

[3] A.C. Newell, Rev. Geophys. **6** (1968) 131

[4] A.N. Kolmogorov, Dokl. Akad. Nauk SSSR **30**, 299303 (1941)

[5] K. Hasselmann, J. Fluid Mech. **12** 481500 (1962); J. Fluid Mech. **15** 273281 (1963)

[6] V.E. Zakharov, N.N. Filonenko, Dokl. Akad. Nauk SSSR **170** (6) (1966) 12921295

[7] V.E. Zakharov, N.N. Filonenko, Zh. Prikl. Mekh. I Tekn. Fiz. **5** (1967) 6267

[8] E. Kuznetsov, A.C. Newell, and V. E. Zakharov, Phys. Rev. Lett. **67**, 3243 (1991).

[9] S. Dyachenko, A. C. Newell, A. Pushkarev and V. E. Zakharov, Physica D **57**, 96 (1992)

[10] G. Düring, C. Josserand and S. Rica, Phys. Rev. Lett. **97**, 025503 (2006)

[11] A. N. Pushkarev and V. E. Zakharov, Phys. Rev. Lett. **76**, 3320 (1996).

[12] A. I. Dyachenko, A. O. Korotkevich, and V. E. Zakharov, JETP Lett. **77**, 477 (2003); A. I. Dyachenko, A. O. Korotkevich, and V. E. Zakharov, JETP Lett. **77**, 546 (2003). A. I. Dyachenko, A. O. Korotkevich and V. E. Zakharov, Phys. Rev. Lett. **92**, 134501(2004)

[13] P. A. Hwang, D. W. Wang, E. J. Walsh, W. B. Krabill, R. N. Swift, Journal of Physical Oceanography **30**, 27532767 (2000)

[14] W. Wright, R. Budakian, and S. Putterman, Phys. Rev. Lett **76**, 4528 (1996)

[15] E. Henry, P. Alstrom and M. T. Levinsen, Europhys. Lett., **52** (1), pp. 2732

[16] M. Yu. Brazhnikov, G.V. Kolmakov, A. A. Levchenko, and L. P. Mezhov-Deglin, JETP Lett. **74**, 583 (2001); M. Yu. Brazhnikov, G.V. Kolmakov, and A. A. Levchenko, Sov. Phys. JETP **95**, 447 (2002); M. Yu. Brazhnikov, G. V. Kolmakov, A. A. Levchenko and L. P. Mezhov-Deglin, Europhys. Lett., **58** (4), pp. 510516 (2002).

[17] Yuri V. L'vov, Kurt L. Polzin, and Esteban G. Tabak, Phys. Rev. Lett. **92**, 128501 (2004)

[18] V. L'vov, *Wave Turbulence Under Parametric Excitation* (Springer-Verlag, Berlin, 1994)

[19] E. Falcon, C. Laroche and S. Fauve, Phys. Rev. Lett. **98**, 094503 (2007)

[20] E. Falcon, S. Fauve and C. Laroche, Phys. Rev. Lett. **98**, 154501 (2007)

[21] C. Connaughton, S. Nazarenko and A. C. Newell, Physica D **184**, 86 (2003)

[22] G. I. Barenblatt, *Scaling, Self-similarity, and Intermediate Asymptotics: Dimensional Analysis and Intermediate Asymptotics*, (Cambridge University Press, Cambridge (1996))

[23] Y. Choi, Y. V. L'vov, S. Nazarenko, Physica D **201**, 121 (2005)

[24] A. Newell, S. Nazarrenko and L. Biven, Physica D (Amsterdam), **152-153**, 520 (2001)

[25] I.V. Ryzhenkova and G.E. Falkovich, JETP **71**, 1085 (1990)

[26] G.V. Kolmakov, JETP **83**, 58 (2006)

[27] HTTP://WWW.CNES.FR/

[28] A-M. Cazabat, private communication.

Part IV

Conclusions and perspectives

Conclusions and perspectives

Conclusion

In this thesis, several studies have been conducted on the statistical properties of observables in dissipative systems forced in statistically out-of-equilibrium states. In these states, observables whether local (such as the local wave amplitude in a steady turbulent-like regime) or global (such as the injected power necessary to maintain a system in a steady out-of-equilibrium state), display large fluctuations. These fluctuations are, in some cases much larger than their average and their distribution often cannot be described by the usual tools of equilibrium statistical mechanics where minimization principles can be used to construct equilibrium distributions. It is this lack of general rule to approach out-of-equilibrium distributions and properties of observables that motivated this work, where simple systems are used to probe and understand the statistics of out-of-equilibrium in order to apply these results to more complex and nontrivial systems.

The first part of this thesis is devoted to the experimental and theoretical study of the fluctuations of the injected power I necessary to sustain a statistically stationary state in dissipative out-of-equilibrium systems. We have recalled in first place the main energy balance equation relating the injected and dissipated power and given simple examples where the dissipated power P_{diss} can be modelized to find relationships between internal energy fluctuations σ_E and injected power fluctuations σ_I (Chapter 1). We have focused specifically in the case where the forcing driving the system out-of-equilibrium is a random gaussian noise. We have shown that the shape of the PDF of the injected power fluctuations displays exponential asymmetric tails and a cusp close to zero, its most probable value. The PDF shape can be computed from a simple theoretical model which uses the fact that both the large scale forcing f and the response of the system v are gaussian and correlated, with $\langle fv \rangle \equiv \langle I \rangle > 0$. The asymmetry of the injected power statistics is solely controled by the mean injected power $\langle I \rangle$, and therefore by the mean dissipated power $\langle P_{diss} \rangle$ (Chapter 2). We have experimentally studied one of the simplest out-of-equilibrium system, an electronic RC circuit forced by a random gaussian noise which displays such a distribution. Several other dissipative systems in stationary states display such statistics of the injected power, even when a larger amount of degrees of freedom are involved in the definition of injected power. Finally, we have experimentally tested the Fluctuation Theorem (FT) in the simple electronic RC circuit (Chapter 3). The FT relates the fluctuations of the injected power fluctuations I_τ averaged over a time lag τ (much larger than the correlation time τ_c) with the internal energy fluctuations. We have found out that in this simple dissipative system the FT holds for small values of $I_\tau / \langle I \rangle$, but later it breaks down for values of $I_\tau / \langle I \rangle$ larger than 1. Also we have tested experimentally the FT in a wave turbulence experience, where a wavemaker excites the surface waves. By measuring both the force applied by the wavemaker on the fluid and the velocity of the wavemaker, the injected power was computed. These simple systems display large fluctuations of the global observable $\epsilon = I_\tau / \langle I \rangle$ larger than 1 for $\tau/\tau_c \sim 20$, making them excellent candidates to study the fullfillment of the FT. We have found out that the FT does

not hold in both cases.

The second part of this thesis is devoted to the experimental study of fluctuations in wave systems. Here, we have studied the local wave amplitude fluctuations at the surface of a fluid. This set of waves are excited by means of parametric amplification (sinusoidal vertical vibration of the container) or large scale forcing (low-frequency vibration of wavemakers plunging into the fluid or low-frequency vibration of the whole container). We present the main results in both cases:

- In the case of the parametric amplification of surface waves, the system developes a stationary cellular pattern at the fluid surface. The cellular pattern oscillates at half the frequency of the forcing f_{ex}. Its geometry, for all working fluids (water or mercury) is squared and appears over the whole surface of the fluid. This mode can present complex dynamical behavior when the surface waves are nonlinearly coupled with another dynamical variable, such as a large-scale flow or a turbulent-like flow. We have focused experimentaly on two situations. In the first case, when the parametric amplification is much larger than the threshold value of the control parameter, defects appear on the pattern (Chapter 5). We have measured the local wave amplitude by means of a capacitive gauge. These defects are lines connecting two sides of the container. The local value of the wave amplitude vanishes on a defect. We have studied their local dynamics and shown that they appear after secondary bifurcations of the cellular pattern. In the turbulent-like state called *defect-mediated turbulence* they change qualitively the internal dynamics of the wave system. This effect can be seen in the PDF of the local wave amplitude, which displays an exponential tail and non-gaussian statistics and also in the PSD of the local wave amplitude, where a power-law spectrum $\sim f^{-5}$ appears as an indicator of the genration of defects over the wave pattern. In the second case an underlying vortex flow is superimposed on the parametrically amplified surface waves (Chapter 5). The vortex flow is generated by a periodic Lorentz force $\mathbf{F}_{L]}$ which acts on the conducting fluid (mercury). We have measured both the local wave amplitude by means of inductive sensors and also the local velocity field by means of Vivès probes. The underlying vortex flow can be viewed as a source of spatio-temporal noise. We have shown that these spatio-temporal fluctuations have two main effects on the parametric surface waves: they locally break the global structure of the cellular pattern and it increases the threshold value of the control parameter for parametric generation of waves.

- In the case of large scale forcing, the nonlinearly interacting waves develope a statistically steady state known as wave turbulence. We have conducted experimental studies on these out-of-equilibrium states, where the local wave amplitude is measured. We have focused on the case where the restitution force of the surface waves is solely capillarity and shown that capillary wave turbulence is a robust phenomenon. In two independent experimental devices where gravity can be neglected, (either in a microgravity environment where the effective gravity is negligible or in a gravity-matching experiment performed with two superposed inmiscible fluids of equal densities where gravity in the wave system is also negligible) a scale invariant PSD of the local wave amplitude over two decades appears, with slope close to -3, as theoretically predicted.

We must stress that the main results of this thesis are robust although the simplicity of the experimental devices used to study dissipative systems. The main idea is to expand these results to more complex systems such as fully developed turbulence, MHD systems or granular materials, where not many experimental studies have been conducted to gain insight on the statistical properties of observables (wheter global or local) in out-of-equilibrium states.

Perspectives and open questions

Fluctuations of observables in dissipative systems sustaining out-of-equilibrium steady states are far from being understood in the same way as fluctuations at thermodynamic equilibrium. There are no generic tools to study such a complex problem, such as the ones of statistical mechanics can provide for equilibrium, and thus in several situations *ad-hoc* approaches have to be used for each specific class of systems. In this work we have experimentally studied the injected power fluctuations in a class of dissipative systems where the forcing f can be modelised by a random gaussian noise of zero mean following the dynamics of an Orstein-Ulhembeck process. This is an importante simplification: no large fluctuations of f nor more complex temporal behavior are taken into account in this approach. Even more, the relation between f and the response v of the system to the driving is linear and no higher derivatives nor (temporal) memory effects where used to describe the dynamics of v. A more detailed study on the effect of these changes on the shape of the PDF of the injected power I, such as nonlinear corrections on the damping rate or memory effects, should give insight on the role of large fluctuations in the out-of-equilibrium properties of internal degrees of freedom, such as the case of intermittency in fully developed turbulence.

Regarding waves at the surface of a fluid displaying out-of-equlibrium steady states, we have studied in several experimental devices their local amplitude dynamics and the effect of fluctuations, whether external (by means of a superimposed underlying flow as a source of spatio-temporal noise) or internal (by nonlinear interaction between excited modes at different characteristic scales) on their statistics. Although interesting results have been found in parametrically amplified waves and in capillary wave turbulence, they all concern local measurements (of wave amplitude or velocity field). The relationship between one-point temporal measurements and spatially resolved measurements rely on certain hypothesis such as the Taylor hypothesis in fully developed turbulence or, in wave systems, the existence of a dispersion relation. Their validity needs to be tested in the nonlinear regime, even the case where the slope of the surface waves is comparable to the wavenumber, and spatio-temporally resolved measurements should be made to fully test wave turbulence theory and the effect of small-scale fluctuations on parametrically excited waves. Furthermore, the dissipative scale in surface waves should be studied, in order to understand their dissipation mechanism in the case of a continuum of excited modes (as in wave turbulence) or a discrete set (as in parametrically excited waves).

Appendix A

Thermalization of the Langevin equation

We recall in this Appendix the equilibrium thermalization process of a brownian particule, described by a Langevin equation using the Fluctuation-Dissipation theorem and we show how the simple dissipative system used in Chapter 2 and 3 does not satisfy the Fluctuation-Dissipation theorem when is forced out of equilibrium by a random gaussian noise with a non-vanishing correlation time.

A.1 Fluctuation-Dissipation theorem and thermalization

It is important to stress that the simple system governed by the Eqs. (2.1) and (2.2)

$$\begin{aligned} \frac{dv(t)}{dt} &= -\gamma v(t) + f(t), \\ \frac{df(t)}{dt} &= -\lambda f(t) + \zeta(t), \end{aligned} \tag{A.1}$$

used in Chapter 2 and 3, where the forcing $f(t)$ is a colored noise, is *strongly* forced out-of-equilibrium. In this configuration, no thermalisation can occur, which means that the we cannot relate directly the fluctuations of the forcing $f(t)$ with the dissipation γ through the equilibrium temperature T. To prove this point, we will use the Fluctuation-Dissipation theorem.

The Fluctuation-Dissipation theorem can be understood as follows: given a system in equilibrium with a thermal bath at a temperature T, the statistical distribution functions are given by the Boltzmann weights $\sim \exp[E/k_BT]$, with E the energy of the system and k_B=1.38 $\times 10^{-23}$ kg m^2 s^{-2} K^{-1} the Boltzmann constant. We apply an external force $F(t)$ which starts to act on the system at an instant $t = 0$. The response of the system to this forcing will be a fluctuating quantity. The variation of the conjugated thermodynamical variable of F (called X[1]) will change the internal energy to $E + X(t)F(t)$. In the case where the forcing acting on the system is "small" enough, we will assume that the response of the system is proportional to the forcing. In the frame of this linear response theory[2], we can write

$$\langle X(t)\rangle_F = \langle X(0)\rangle_0 + \int_0^t \chi(t-t')F(t')dt',$$

where $\langle X(t)\rangle_F$ and $\langle X(t)\rangle_0$ represent the perturbed and unperturbed averaged variables, and $\chi(t-t')$ the linear response function of the system under study. It is important to notice that we have assume

[1]Examples of thermodynamical conjugated pairs are for instance pressure and volume, entropy and temperature, strain and stress, voltage and impedance, and mobility and diffusivity.

[2]See the first references in Chapter 3 for linear response theory

the causality of the system ($\chi(t) = 0$ for $t < 0$) which is set in a stationary regime so that in the unperturbed configuration $\langle X(t)\rangle_0 = \langle X(0)\rangle_0$. In this framework, we can relate the fluctuations of the observable X in equilibrium, given by its autocorrelation function $C_{XX}(\tau) = \langle X(t+\tau)X(t)\rangle_0$, with the linear response function $\chi(t)$ of a system at equilibrium with a thermal bath at temperature T.

To do so in a simple way, we suppose that $F(t) = F_0$ for $t > 0$. Assuming that the distribution function of the energy of the system is given by the Boltzmann weights, we develope them as $\exp[E'/BT] \simeq \exp[E/BT](1 + F_0 X(t))$. Then we compute the perturbed average $\langle X(t)\rangle_F$ as

$$\langle X(t)\rangle_F = \langle X(0)\rangle_0 + \frac{F_0}{k_B T} C_{XX}(t).$$

The Fluctuation-Dissipation theorem therefore states that

$$C_{XX}(t) = k_B T \int_0^t \chi(t - t')dt',$$

or in frequency domain ω

$$S_X(\omega) = 4\frac{k_B T}{\omega} Im(|\widehat{\chi}(\omega)|).$$

In the Langevin equation (as it is written in Eq.(2.2)), $\zeta(t)$ is a gaussian white noise with no correlation time and the Fluctuation Dissipation theorem holds with $S_f(\omega) = 4k_B T/\lambda(\lambda^2 + \omega^2) = 4\frac{k_B T}{\omega} Im(|\widehat{\chi}(\omega))$, with $\chi(t) = \exp[-\lambda t]$ and $D = \gamma k_B T$. From Eq.(2.2) we can see that the forcing term $f(t)$ used in Eq.(2.1) has a typical correlation time scale of order λ^{-1} such that the frictional term should involve a certain memory effects and be written instead of γv as $\int_0^t (D/k_B T) e^{\lambda(t-t')} v(t')dt'$, in order to describe a thermal bath with a finite correlation time.

Appendix B

Calculation of the PDF of the injected power from the Fokker-Planck equation

We present here the calculation of the probability density function of the injected power I for the simple systems governed by Eqs.(2.1) and (2.2).

B.1 Fokker-Planck equation

In this complement we will discuss the calculation of the stationary probability density function of the system described in Eqs. (2.1) and (2.2). Taking the derivative of Eq.(2.1) and using Eq.(2.2), we can write the evolution of $v(t)$ as

$$\ddot{v}(t) + (\lambda + \gamma)\dot{v}(t) + \gamma\lambda v(t) = \zeta(t),$$

$\zeta(t)$ being a white noise with zero mean and singular auto-correlation function $\langle \zeta(t)\zeta(t')\rangle = D\delta(t-t')$. This is the equation for the position $x(t)$of a damped particle of unit mass and damping coefficient $\lambda + \gamma$ in a quadratic potential of stiffness $\lambda\gamma$, although in this case there are no oscillations due to the fact that the eigenvalues of the equation are $\{-\lambda, -\gamma\}$. Following [6], the evolution equation for the joint conditonal probability distribution function $\mathcal{P}(v, f, t)$ of both variables is called the Fokker-Planck (or the forward Kolmogorov) equation and reads

$$\partial_t \mathcal{P}(v, f, t) = -\partial_v \left[(f - \gamma v)\mathcal{P}(v, f, t)\right] + \lambda\partial_f \left[f\mathcal{P}(v, f, t)\right] + \frac{\Delta}{2}\partial_{ff}\mathcal{P}(v, f, t).$$

In the stationary limit, no temporal dependence on time appears and the solution to the stationary Fokker-Planck solution with a gaussian initial condition is the so-called bivariate gaussian PDF. To calculate this joint PDF a simple calculus can be done by noting that if $\zeta(t)$ is gaussian and the equations are linear, then $\mathcal{P}(v, f)$ must remain gaussian. We supose that, in the stationary limit,

$$\mathcal{P}(v, f) \sim \exp[-\frac{1}{2}(av^2 + 2bvf + cf^2)].$$

We have also used the fact that the mean values of both variables are zero, which results directly from $\langle\zeta\rangle \equiv 0$. In the stationary limit the condition $\partial_t\mathcal{P} = 0$ means that the coefficients have to obey

the relationships

$$\begin{aligned}\langle v^2\rangle &= \frac{1}{a} \equiv \sigma_v^2,\\ \langle f^2\rangle &= \frac{1}{c} \equiv \sigma_f^2,\\ \langle vf\rangle &= \frac{1}{b} \equiv r\sigma_v\sigma_f,\end{aligned} \tag{B.1}$$

where we have defined the correlation coefficient $r = \langle vf\rangle/\sigma_v\sigma_f$. Calculating these coefficients from Eqs.(2.1) and (2.2) is straightforward. We can write stationary solutions of both equations as

$$v(t) = \int_0^t f(t')e^{-\gamma(t-t')}dt', \tag{B.2}$$

$$f(t) = \int_0^t \zeta(t')e^{-\lambda(t-t')}dt' \tag{B.3}$$

where we can compute that $\langle f^2\rangle = D/2\lambda$, $\langle v^2\rangle = D/2\lambda\gamma(\lambda+\gamma)$ and $\langle vf\rangle = D/2\lambda(\gamma+\lambda)$. With these constants, the normalized probability density function is the bivariate gaussian PDF

$$\mathcal{P}(v,f) = \frac{1}{2\pi\sigma_v.\sigma_f(1-r^2)^{1/2}}\exp\left[-\frac{1}{2(1-r^2)}\left(v^2/\sigma_v^2 - 2rvf/(\sigma_v\sigma_f) + f^2/\sigma_f^2\right)\right].$$

B.2 Calculation of the probability density function of I=fv

From the solution of the Fokker-Planck equation, $\mathcal{P}(v,f)$, we compute the PDF of $I = fv$. We begin by normalising the variables $v' = v/\sigma_v$ and $f' = f/\sigma_f$ in order to simply the calculations. Then, we change variables from the pair $\{f', v'\}$ to $\{I = fv, u = v'\}$. The probability density function $\mathcal{P}(I,u)$ must then satisfy

$$\mathcal{P}(v'(I,u), f'(I,u))\left|\frac{\partial(v'(I,u), f'(I,u))}{\partial(I,u)}\right| = \mathcal{P}(I,u),$$

where

$$\left|\frac{\partial(v'(I,u), f'(I,u))}{\partial(I,u)}\right| = \frac{1}{\sqrt{|I|}}$$

is the determinant of the jacobian of the transformation, therefore the joint PDF of $\{f', v'\}$ is

$$\mathcal{P}(I,u) = \frac{1}{2\pi(1-r^2)^{1/2}\sqrt{|I|}}\exp\left[-\frac{1}{2(1-r^2)}\left(u^2 - 2rI + u^2/I^2\right)\right],$$

with $r = \langle I\rangle$. From this starting point, we integrate on u to get the probability density function of I, as

$$P(I) = \frac{\exp\left[rI/\left(1-r^2\right)\right]}{2\pi(1-r^2)^{1/2}\sqrt{|I|}}\int_{-\infty}^{\infty}\exp\left[-\frac{1}{2(1-r^2)}\left(v^2 + v^2/I^2\right)\right]dI.$$

The integral can be aproximated using the steepest descent method[1] for functions of the form $\exp[-f(u)]$, where $f(u)$ has a global unique minimum at u_0 in the interval of integration. The function can be expanded as a Taylor series around u_0

$$f(u) = f(u_0) + f'(u_0)(u-u_0) + f''(u_0)\frac{(u-u_0)^2}{2} + O((u-u_0)^3),$$

where $f'(u_0)$ stands for the derivative of f with respect to u, evaluated at u_0.

Due to the fact that u_0 is a global minimum, we can aproximate the integral

$$\int_{-\infty}^{\infty} \exp[f(u)]du \sim \exp[f(u_0)] \int_{-\infty}^{\infty} \exp[\frac{f''(u_0)}{2}(u-u_0)^2]du \equiv \sqrt{\frac{2\pi}{f''(u_0)}}\exp[f(u_0)].$$

We have just used that the former integral can be aproximated by a gaussian function that decreases fast such that only the the values of u close to u_0 are important in the integration.

We apply the former method the function $f(u) = (u^2 + I^2/u^2)/2(1-r^2)$, which has a global minimum at $u_0 = \sqrt{|I|}$ with concavity $f''(u_0) = 4/(1-r^2)$. The probability density function of I can be aproximated by

$$P(I) = C\exp[rI/\sqrt{1-r^2}] \times \exp[|I|/(1-r^2)]/\sqrt{|I|},$$

with C a normalisation constant. This exponential behavior can be sorted out of the exact expression of $P(I)$, that comes from the integral representation of the modified Bessel function of the second kind of order zero $K_0(x)$ as[2]

$$\int_{-\infty}^{\infty} \exp[(y^2 + x^2/y^2))]dy = \frac{1}{2\pi}K_0(|x|).$$

Using the PDF of I we can calculate all the moments of I, $\langle I\rangle^n$ as,

$$\langle I\rangle^n = \int_{-\infty}^{\infty} I^n P(I)dI,$$

which will depend only on the normalized mean injected power $r = \langle v'f'\rangle$.

[1] See, for instance, *Mathematical Methods for Physicists*, George B. Arfken and Hans J. Weber, Academic Press, New York (2000)

[2] See, for instance, from B. Sorin, P. Thionet, *Revue de statistique apliquée*, **16**, N°4 (1968), pp.65-72)

Appendix C

Copie of articles

C.1 "Fluctuations of Energy Flux in Wave Turbulence", *published in Physical Review Letters,* **100**, *064503 (2008)*

Abstract: We report that the power driving gravity and capillary wave turbulence in a statistically stationary regime displays fluctuations much stronger than its mean value. We show that its probability density function (PDF) has a most probable value close to zero and involves two asymmetric roughly exponential tails. We understand the qualitative features of the PDF using a simple Langevin-type model.

C.2 "PDF of the power injected by a random forcing into dissipative systems", *submitted to The European Journal of Physicas B (2008)*

Abstract: The fluctations of the injected power necessary to drive a dissipative system into a nonequilibrium steady state, is studied. Here we develope the ideas evocated in a previous letter. First, we show that very different physical systems driven by a random forcing present identical features for the fluctuations of their injected power. Other related quantities like the heat flux in turbulent convection exhibit the same type of fluctuations. In all the cases considered, the Probability Density Functions (PDF) of the injected power, I, have a characterisic cusp at $I = 0$ and asymmetrical exponential tails. In the second part we will detail the derivation of an exact analytical formula of the PDF of these fluctuations in the simplest case of this class of dissipative brownian motion: we compute first the joint PDF of velocity and applied force for the brownian motion of a particles sustained by an Ornstein–Uhlenbeck (O–U) type of noise and then we deduce the PDF of their product. The agrements and discrepancies of these PDF with the ones obtained in other dissipative systems are discussed. Further extensions of these works, espacially for energy flux in turbulent flows will be discussed to conclude.

C.3 "Fluctuations of energy flux in a simple dissipative out-of-equilibrium system", *submitted to Physical Review E (2008).*

Abstract: We report the statistical properties of the fluctuations of the energy flux in an electronic

RC circuit driven with a stochastic voltage. The fluctuations of the power injected in the circuit are measured as a function of the damping rate and the forcing parameters. We show that its distribution exibits a cusp close to zero and two asymmetric exponential tails, the asymmetry being driven by the mean dissipation. This simple experiment allows to capture the qualitative features of the energy flux distribution observed in more complex dissipative systems. We also show that the large fluctuations of injected power averaged on a time lag do not verify the Fluctuation Theorem even for long averaging time. This is in contrast with the findings of previous experiments due to their small range of explored fluctuation amplitude. The injected power of an ensemble of N circuits is also studied to mimic systems with large number of particles either correlated or not, such as in a dilute granular gas.

C.4 "Local Dynamics of Defects in Parametrically Excited Waves", *submitted to International Journal of Bifurcation and Chaos (2008).*

Abstract: We present an experimental study on the local dynamics of parametrically excited waves at an air-water interface when defects are present in the wave pattern. The probability density function (PDF) of the local wave amplitude displays an exponential part for values close to the average amplitude and decreases sharply to zero for large amplitudes. The power spectral density (PSD) of the local amplitude fluctuations shows a power-law behavior over one decade which we relate to a regime of defect-mediated turbulence.

C.5 "Faraday Waves in the Presence of Spatio-Temporal Noise", *to be submitted to Physical Review E (2008).*

Abstract: We report an experimental study on the nonlinear interaction between a spatially periodic vortex flow and the celular flow that generates parametrically excited surface waves in a liquid metal. The vortex flow acts as a source of spatio-temporal noise for the wave system. The subharmonic response of the local wave amplitude and velocity field is diminished as the vortex flow intensity increases, as it is shown in their power spectral densities, probability density functions, correlation measurements and spectral coherence. In addition, the instability threshold of the subharmonic waves is increased, showing the effect of an effective viscosity.

C.6 "Capillary wave turbulence on a spherical fluid surface in zero gravity", *submitted to Physical Review Letters (2007).*

Abstract: We report the observation of capillary wave turbulence on the surface of a fluid layer in low gravity environment. In such conditions, the fluid covers all the internal surface of the spherical container which is submitted to random forcing. The surface wave amplitude displays power-law spectrum over two decades in frequency. This spectrum is found in roughly good agreement with the wave turbulence theory. Such a large band observation has never been reached during ground experiments due to the presence of gravity waves. When the forcing is periodic, two-dimensional

spherical patterns are observed on the fluid surface such as subharmonic stripes or hexagons with wavelength satisfying the capillary wave dispersion relation.

C.7 "Symmetry Induced 4-Wave Capillary Wave Turbulence", *submitted to Physical Review Letters (2008).*

Abstract: We report theoretical and experimental results on 4-wave capillary wave turbulence. A system consisting of two inmiscible and incompressible fluids of the same density can be written in a Hamiltonian way for the conjugated pair (η, Ψ). When given the symmetry $z \rightarrow -z$, the set of weakly non-linear interacting waves display a Kolmogorov-Zakharov (KZ) spectrum $n_k \sim k^{-4}$ in wave vector space. The wave system was studied experimentally with two inmiscible fluids of almost equal densities (water and silicon oil) where the capillary surface waves are excited by a low frequency random forcing. The power spectral density (PSD) and probability density function (PDF) of the local wave amplitude are studied. Both theoretical and experimental results are in fairly good agreement with each other.